LBL-32310
UC-802

Lawrence Berkeley Laboratory

UNIVERSITY OF CALIFORNIA

EARTH SCIENCES DIVISION

Geologic Characterization of Fractures as an Aid to Hydrologic Modeling of the SCV Block at the Stripa Mine

S.J. Martel

April 1992

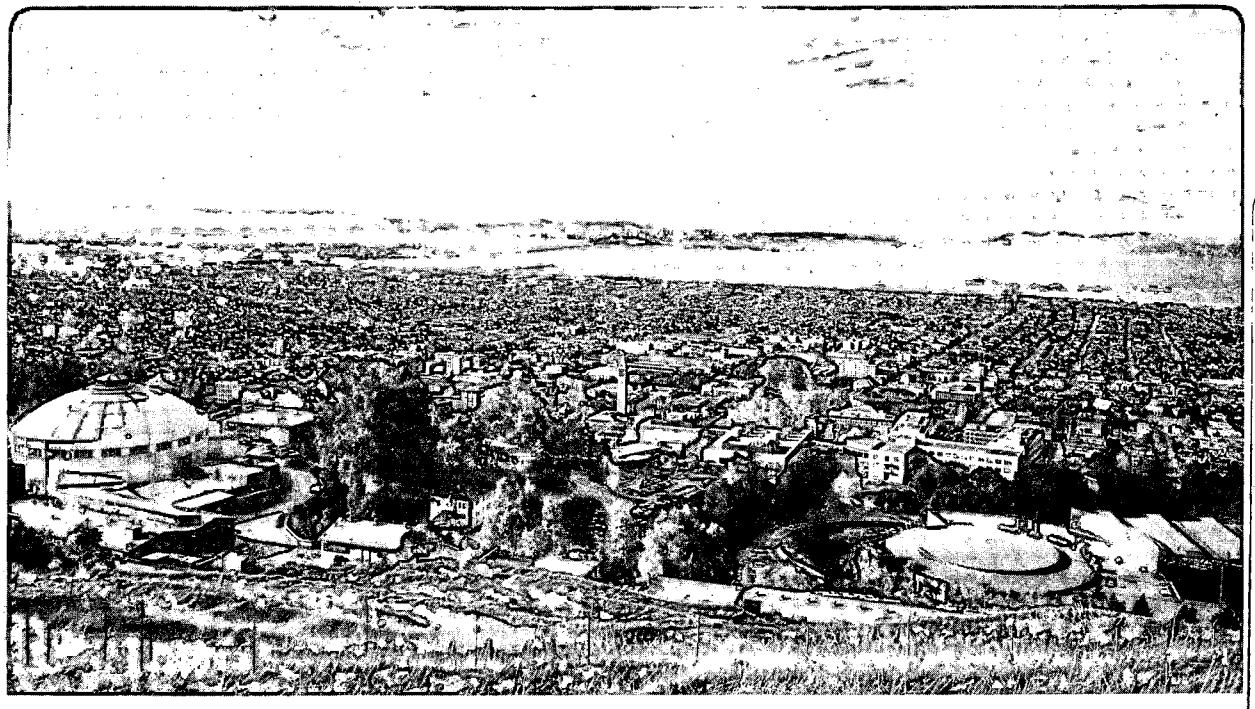

| LOAN COPY |
|Circulates |
|for 4 weeks| Bldg. 50 Library.
LBL-32310
Copy 2

Prepared for the U.S. Department of Energy under Contract Number DE-AC03-76SF00098

DISCLAIMER

This document was prepared as an account of work sponsored by the United States Government. Neither the United States Government nor any agency thereof, nor The Regents of the University of California, nor any of their employees, makes any warranty, express or implied, or assumes any legal liability or responsibility for the accuracy, completeness, or usefulness of any information, apparatus, product, or process disclosed, or represents that its use would not infringe privately owned rights. Reference herein to any specific commercial product, process, or service by its trade name, trademark, manufacturer, or otherwise, does not necessarily constitute or imply its endorsement, recommendation, or favoring by the United States Government or any agency thereof, or The Regents of the University of California. The views and opinions of authors expressed herein do not necessarily state or reflect those of the United States Government or any agency thereof or The Regents of the University of California and shall not be used for advertising or product endorsement purposes.

This report has been reproduced directly
from the best available copy.

Available to DOE and DOE Contractors
from the Office of Scientific and Technical Information
P.O. Box 62, Oak Ridge, TN 37831
Prices available from (615) 576-8401, FTS 626-8401

Available to the public from the
National Technical Information Service
U.S. Department of Commerce
5285 Port Royal Road, Springfield, VA 22161

Lawrence Berkeley Laboratory is an equal opportunity employer.

DISCLAIMER

This document was prepared as an account of work sponsored by the United States Government. While this document is believed to contain correct information, neither the United States Government nor any agency thereof, nor the Regents of the University of California, nor any of their employees, makes any warranty, express or implied, or assumes any legal responsibility for the accuracy, completeness, or usefulness of any information, apparatus, product, or process disclosed, or represents that its use would not infringe privately owned rights. Reference herein to any specific commercial product, process, or service by its trade name, trademark, manufacturer, or otherwise, does not necessarily constitute or imply its endorsement, recommendation, or favoring by the United States Government or any agency thereof, or the Regents of the University of California. The views and opinions of authors expressed herein do not necessarily state or reflect those of the United States Government or any agency thereof or the Regents of the University of California.

LBL-32310

GEOLOGIC CHARACTERIZATION OF FRACTURES AS AN AID TO HYDROLOGIC MODELING OF THE SCV BLOCK AT THE STRIPA MINE

by

Stephen J. Martel
Lawrence Berkeley Laboratory
Earth Sciences Division
One Cyclotron Road
Berkeley, CA 94720

April 1992

This work was supported by the Director, Office of Civilian Radioactive Waste Management, Office of External Relations, under U.S. Department of Energy Contract No. DE-AC03-76SF00098.

Table of Contents

1 SUMMARY 1

2 INTRODUCTION 4

3 THE STRIPA MINE AND THE SCV SITE 5

4 REVIEW OF THE GEOLOGY AT STRIPA 8

4.1 Summary of Local Geologic History 8

4.1.1 Svecokarelian crystalline basement rocks 8

4.1.2 Post-Svecokarelian tectonic history 8

4.1.3 Neotectonics, seismicity, and post-glacial rebound 17

4.1.4 Conclusions regarding post-Svecokarelian fracturing 17

4.2 The Stripa Granite 17

4.3 Previous Mapping of Fracture Systems at the Stripa Mine 18

4.4 Fracture Fillings 19

4.5 Conclusions Based on Previous Work on Fractures at Stripa 19

5 CONCEPTUAL MODEL OF FRACTURE ZONES AT STRIPA 22

6 OBSERVATIONS AND INTERPRETATIONS OF FRACTURE ZONES EXPOSED IN DRIFTS 30

6.1 Zone H 30

6.1.1 360 Level 31

6.1.2 310 Level 34

6.1.3 410 Level 37

6.1.4 Validation Access Drift 40

6.1.5 Conclusions Regarding Zone H 40

6.2 Zone M 40

6.3 Zone K 41

6.4 Evidence for Multiple Generations of Fractures 41

6.5 Porosity due to Alteration of the Granite 43

6.6 Comparison with scanline information 43

6.7 Comparison of geophysical model with drift-wall observations 44

7 BOREHOLE FRACTURE ORIENTATION DATA 45

7.1 Introduction to Borehole Bias 45

7.2 Interpretation and Discussion of SCV Borehole Data in Light of Borehole Bias 48

8 THE MODERN STRESS STATE 57

9 POSSIBLE DRIFT EXCAVATION EFFECTS 58

10 CONCLUSIONS 64

11 ACKNOWLEDGMENTS 67

12 REFERENCES 68

APPENDIX 1

Coordinates of SCV Block Corners (From Olsson et al., 1989) 73

APPENDIX 2.1

Information on SCV Boreholes W1, W2, N2, N3, N4 74

APPENDIX 2.2

Information on SCV Boreholes C1, C2, C3, C4, C5 75

APPENDIX 2.3

Information on SCV Boreholes D1, D2, D3, D4, D5, D6 76

APPENDIX 2.4

Calculated Fracture Zone/Borehole Intersection Depths 77

APPENDIX 3

Equations for Calculating the Redistribution of Stress 78

APPENDIX 4

Equations for Calculating the Effective Hydraulic Conductivity for Radial Flow into a Cylindrical Excavation 81

List of Figures

Figure 3.1. Map showing the location of the Stripa mine. 6

Figure 3.2. Map showing the location of drifts and boreholes near the SCV block at the Stripa mine. Boreholes and drifts are projected orthogonally onto a horizontal plane. Angles denote overall inclination of the boreholes and are rounded off to the nearest degree. Borehole C3 is not shown 7

Figure 4.1. Generalized geologic map of southern and central Sweden showing dolerite intrusions a) older than 1150 Ma and b) younger than 1150 Ma (modified from Patchett, 1978). The Protogine zone (PZ) lies along the boundary between rock assemblages labeled Sveconorwegian and Svecofenninan (Svecokarelian). The lake southeast of Lake Vänern is Lake Vättern. 9

Figure 4.2. Geologic map of the Lindesberg SV quadrangle (from Olkiewicz *et al.*, 1979). 10

Figure 4.3. a) Rock block map of the Bergslagen district and surrounding environs (from Tirén and Beckenholm, 1990, p. 198). Lines denote geomorphic lineaments. 12

Figure 4.4. Lineament map of a 400 km^2 area centered about the Stripa mine (from Black *et al.*, 1990, p. 197). Lakes are shown in grey. This figure was prepared using a computer-assisted terrain analysis with the direction of synthetic "illumination" being from the northwest. This "illumination" direction would preferentially emphasize northeast-trending features. 13

Figure 4.5. Lineament map of a 48 km^2 area about the Stripa mine (from Carlsten, 1985, p. 34). 14

Figure 4.6. Generalized fracture trace map of the 335-level showing the ventilation drift and branching drifts. The northeastern branch drift is the computer room. The southeastern branch drift is the full-scale drift. The southwestern branch drift is the Luleå drift. The northwestern branch drift is the time-scaled drift. From Olkiewicz *et al.*, 1979. 20

Figure 4.7. Detailed fracture trace map of the north end of the ventilation drift. From Olkiewicz *et al.*, 1979. 21

Figure 5.1. Maps showing traces of the major inferred SCV fracture zones at the 310 level. 23

Figure 5.2. Maps showing traces of the major inferred SCV fracture zones at the 360 level. 23

Figure 5.3. Maps showing traces of the major inferred SCV fracture zones at the 410 level. 24

Figure 5.4. Comparison of SCV borehole core characteristics against the locations where SCV fracture zones project into the boreholes. The column labeled D is a composite from all the D holes 25

Figure 6.1. Map showing traces of major fractures within zone H at exposures at the 360 level. Faults are labeled drift by drift, with increasing numbers from left to right. The scale is given by the 50 m grid. The swath of red granite is stippled. 32

Figure 6.2. Diagram showing splay cracks along a) an isolated fault, and b) a fault zone that is bounded on both sides by faults (heavy lines). The fault zone here strikes north, dips steeply to the east, and has slipped in a right-lateral, normal oblique fashion. In map view, the traces of the splay cracks (light lines) trend ENE. In cross section view, the traces of the splay cracks are vertical. 33

Figure 6.3. Map showing traces of the major fractures of zone H at the 310 level. The scale is given by the mine coordinate grid lines. The traces of zones H and Hb as defined in Table 5.1 are shown for the 310 level. Numbers by fractures give fracture dips. 37

Figure 6.4. Map showing traces of the major fractures in the vicinity of zone H at the 410 level and in the validation access drift. The traces of zones H and Hb as defined in Table 5.1 are shown for the 410 level. Numbers by fractures give fracture dips. 38

Figure 6.5. Controlled sketch showing the trace of the normal fault on the south wall of the 410A drift. View is along fault strike 39

Figure 6.6. Map showing traces of fractures identified in the walls (side panels) and ceiling (central panels) of the 3-D migration drift (360-level) and the projected intersection of zone K with the drift. Mine north is to the top of the page (modified from Abelin and Birgersson, 1987). 42

Figure 6.7. Location of scanlines at the Stripa mine. From Gale *et al.* (1990). 44

Figure 7.1. Relative probability of a borehole intersecting a fracture. For fractures of set A, $\theta = 60°$, and the relative probability of intersecting a fracture is 0.5. For fractures of set B, $\theta = 90°$, and the relative probability of intersecting a fracture is 1.0. Over a given distance along the borehole, twice as many fractures of set B are intersected as from set A 46

Figure 7.2. Equal area lower hemisphere plots of synthetic distributions of 500 fracture poles from a) a uniform distribution sampled at random and b) a distribution prepared from combinations of fracture strikes and fracture dips selected at random. Note the concentration of poles to subhorizontal fractures in b. 47

Figure 7.3. Comparison of synthetic distributions of 500 fracture poles selected from a uniform fracture distribution sampled along boreholes of four orientations. Plots are equal area lower hemisphere projections. Borehole orientations are marked by large dots. Note the clustering of fracture poles about the borehole orientations. a) Vertical borehole. b) Borehole trends west and is horizontal. c) Borehole trends southwest and plunges 45°. d) Borehole trends east and plunges 60° 49

Figure 7.4. Comparison of recorded (left) and synthetic (right) fracture orientation distributions for boreholes a) W1 and b) W2. Orientations of boreholes are marked by large dots. Data points touching the borehole orientation dots have been removed for the sake of clarity. 50

Figure 7.5. Comparison of recorded (left) and synthetic (right) fracture orientation distributions for boreholes a) N2, b) N3, and c) N4. Orientations of boreholes are marked by large dots. Data points touching the borehole orientation dots have been removed for the sake of clarity. 51

Figure 7.6. Comparison of recorded (left) and synthetic (right) fracture orientation distributions for boreholes a) C1, b) C2, and c) C3. Orientations of boreholes are marked by large dots. Data points touching the borehole orientation dots have been removed for the sake of clarity. 52

Figure 7.6. (continued). Comparison of recorded (left) and synthetic (right) fracture orientation distributions for boreholes d) C4 and e) C5. Orientations of boreholes are marked by large dots. Data points touching the borehole orientation dots have been removed for the sake of clarity. 53

Figure 7.7. Comparison of recorded (left) and synthetic (right) fracture orientation distributions for boreholes a) D1, b) D2, and c) D3. Orientations of boreholes are marked by large dots. Data points touching the borehole orientation dots have been removed for the sake of clarity. 54

Figure 7.7. (continued). Comparison of recorded (left) and synthetic (right) fracture orientation distributions for boreholes d) D4, e) D5, and f) D6. Orientations of boreholes are marked by large dots. Data points touching the borehole orientation dots have been removed for the sake of clarity. 55

Figure 9.1. Orientation of far-field principal stresses, the Validation drift and the cylindrical coordinate system about the drift. 59

Figure 9.2. Stress changes near a drift plotted as a function of normalized distance from the drift center. a) Stress changes at the drift wall. b) stress changes at the drift floor and roof. 60

Figure 9.3. a) Hoop stress ($\sigma_{\theta\theta}$) above drift axis. b) Normalized fracture hydraulic conductivities predicted for a vertical, drift-parallel fracture at the roof of the Validation drift. 63

List of Tables

Table 5.1. Orientation and position of SCV fracture zones (from Black *et al.*, 1990).....26

Table 5.2. Calculated depths of intersection of SCV fracture zones with SCV boreholes.....27

Table 5.3. Recorded depths of intersection of SCV fracture zones with SCV boreholes (from Black *et al.*, 1990). No intersections are recorded for borehole C4. 27

Table 5.4. Characteristics of SCV borehole cores as determined by inspection by the author. Intervals of pronounced fracturing (F), red color (R), or pitting (P) are noted. Regular and bold fonts mark observations from photographs and cores, respectively. In general, drilling-induced fractures are not distinguished here.....28

Table 6.1. Coordinates of central points zone H exposures (as defined by red granite) at 310, 360 and 410 levels.....30

Table 6.2. Evidence for faulting at 360 level based on offset markers. 34

Table 6.3. Evidence for faulting at 360 level based on splay cracks.....35

Table 6.4. Evidence for faulting at 360 level based on slickenlines. For oblique slipsenses, N=normal, R=reverse, RL=right-lateral and LL=left-lateral.....36

Table 8.1. "Virgin" stress state for the SCV block 57

Table 9.1. Predicted post-drift stresses and stress changes along the Validation drift at Stripa (MPa). Positive values are compressive.....61

1 SUMMARY

A series of hydrologic tests have been conducted at the Stripa research mine in Sweden to develop hydrologic characterization techniques for rock masses in which fractures form the primary flow paths. The structural studies reported here were conducted to aid in the hydrologic examination of a cubic block of granite with dimensions of 150 m on a side. This block (the SCV block) is located between the 310- and 460-m depth levels at the Stripa mine. This report describes and interprets the fracture system geology at Stripa as revealed in drift exposures, checks the interpretive model against borehole records and discusses the hydrologic implications of the model, and examines the likely effects of stress redistribution around a drift (the Validation drift) on inflow to the drift along a prominent fracture zone.

The locations and extents of several fracture zones in the SCV block have been inferred from geophysical imaging, hydrologic tests, and borehole data. The principal zones are termed A, B, H, Hb, I, M and K. Zones A and B dip at 45°±3° to the SE. Zones H, Hb, and I dip to the east at 76°, 60° and 63°, respectively. Zone K dips 65° to the NE, and zone M dips 87° to the NE. Zone H (together with Hb) is the most prominently expressed zone and may coincide with a structure several kilometers long identified through a regional aeromagnetic survey. Zones H and Hb have a projected intersection near the 400 m depth level at the SCV block.

Only zone H was identified in accessible portions of the mine tunnels in or near the SCV block. The other zones do not intersect the drifts near the block, because of either their orientation or their limited extent. Based on the drift exposures, zone H could not be distinguished from zone Hb, hence they are referred to jointly as zone H here. The plane that passes through the center of zone H exposures at the 310-, 360- and 410-m depth levels in the mine strikes N-S and dips ~64° to the east. This orientation for zone H has an uncertainty of several degrees in strike and dip and can not be distinguished from the orientations of zones H and Hb given in the preceding paragraph.

Zone H exposures are characterized by a red granite that contrasts sharply with the grey granite typical of the mine. The thickness of the red granite across zone H appears to vary from ~5 m to ~40 m. The color of zone H is its most distinguishing feature; its edges are not sharply defined based on either the intensity or orientation of its fractures. The thickness of zone H exposures increases preceding from the 410 level up to the 310 level; this is consistent with the separate orientations of zones H and Hb listed above.

Sealed fractures of numerous orientations occur at zone H exposures. Most individual fractures are difficult to trace more than a few meters. However, the longest fractures in zone H exposures typically strike to the north and dip steeply to the east, subparallel to the zone as a whole. Many of these long fractures are faults. At the 360 level, the longest fractures west of the zone generally strike NNW and east of the zone they generally strike NNE.

The steeply-dipping faults with a northerly strike apparently have accommodated different styles of slip through time. Evidence for normal dip slip on these faults is most pronounced and consists of a) fault surfaces with slickenlines that plunge down dip, b) faults being linked by steeply inclined fractures or by cavities and c) displaced subhorizontal veins. Some faults show evidence for reverse slip. Finally, some faults have accommodated right-lateral strike slip based on steeply-dipping fractures that splay to the northeast. The rather chaotic arrangement of fractures in

zone H, the structural evidence for at least three episodes of slip on zone-parallel faults, and previously published evidence for at least two episodes of mineralization along fractures at Stripa are consistent with the Stripa fracture zones being old reactivated fault zones. The normal faulting could have occurred between 850 Ma and 1000 Ma when a regional set of subvertical north-striking dikes were intruded.

Although most of the permeability and much of the porosity in the Stripa granite is due to the fractures, some porosity occurs in the form of pitting. Some borehole cores are pitted and in one case a pitted region in the SCV block has been located through geophysical techniques. The pitting has been interpreted to reflect dissolution of quartz from the granite. Pitting also occurs in a drift exposure at the 410 level along a zone H fault. At that spot fluorite was precipitated in pits in the granite and calcite was precipitated in cavities along the fault. These observations suggest that some porosity in the SCV block may be due to the flow of reactive fluids along faults and associated rock/fluid reactions.

Direct information on the fractures within the SCV site comes from four sets of boreholes. Although these holes trend in a variety of directions, most are shallowly inclined, so they are best-oriented to detect steeply-dipping fractures. Most of the fractures that are open in recovered drill cores are along pre-existing mineralized (or otherwise sealed) fractures. Independent of the location and orientation of a borehole, there is a strong tendency for the fractures intersected by a hole to be nearly perpendicular to the borehole. To test the extent to which this reflects borehole sampling bias, the actual fracture orientation distribution encountered in each borehole was compared with a synthetic distribution obtained as if the borehole had sampled a uniform distribution of fracture orientations. The comparison indicates 1) there probably is a strong uniform random component to the actual distribution of *in situ* fracture orientations and 2) the observed distribution is strongly affected by the orientation of the borehole. The holes through zone H do show a higher density of steeply-dipping fractures that strike subparallel to the zone than would be expected if the *in situ* distribution of orientations were uniform. Zone-parallel fractures are therefore larger and/or more abundant within zone H than fractures of other orientations. The conclusion that zone H contains fractures of numerous orientations, but with fractures subparallel to the zone being largest or most common, squares with drift wall observations by the author and with the inferred history of fracturing and faulting.

The hydraulic conductivity of a fracture in zone H is expected to reflect the orientation of the fracture and the state of the current stress field. Based solely on the varied orientations of fractures in zone H, one might expect its bulk conductivity to be nearly isotropic. However, because the stress field at the mine appears to be strongly anisotropic, the hydraulic conductivities of the fractures in the zone should vary as a function of their orientation. Other factors being equal, the most conductive fractures are likely to be perpendicular to the least compressive stress, with the least conductive fractures being perpendicular to the most compressive stress. The stress measurements in the mine to date indicate that the ambient most compressive horizontal stress is oriented WNW and the least compressive stress is vertical. Steeply-dipping fractures that strike NNE would tend to have the smallest apertures on the average and be least conductive. This is approximately the orientation of the longest fractures in zone H.

The opening of a drift will significantly perturb the stress field in the adjacent rock and hence could potentially change the fracture conductivity within a few diameters of a drift. The elastic effects will be strongest at the drift walls and will die out within a few diameters of a drift. The

magnitude of these effects will depend on the orientations of the drift, on the orientations and magnitudes of the far-field principal stresses, and on the orientation of the fractures near the drift. In most cases, the excavation of a drift at depth will promote the opening of pre-existing fractures that parallel the perimeter of the drift, whereas pre-existing fractures oriented such that they radiate from the drift will tend to close. The effect on fractures that are approximately perpendicular to the drift axis would be minor. Because the radial and drift-perpendicular fractures would carry water into the drift, the stress effects on these fractures are particularly important. The perturbing effects would be greatest for drifts that trend perpendicular to the most compressive far-field principal stress (σ_1) and least for drifts that trend parallel to σ_1. For a drift oriented obliquely to the principal stress axes, perturbation effects will vary significantly along the drift.

The stress perturbation caused by the excavation of the Validation drift was analyzed to examine the possible effect of flow along zone H near the drift. This was to test whether elastic effects associated with drift excavation could account for an inferred 8-fold decrease of flow to the region of the drift after the drift was excavated. The Validation drift at Stripa trends at 287° and is inclined down to the WNW at 3° and has a radius of approximately 1.5 m. Zone H intersects the drift approximately 30 m from its east end. The orientations of the drift and the most compressive far-field horizontal stress differ by only 4°, indicating that a 2-D plane strain analysis is useful for analyzing the stress effects on zone H due to excavation. Using the most recent stress measurements for the SCV area, the compressive normal stress tangential to the drift should increase between 50% (at the drift walls) and 133% (at the roof and floor of the drift); these effects decay to less than 10% within a few meters from the drift. At the levels of normal stress near the Validation drift, experimental work by others suggests that fracture hydraulic conductivity decreases as the compressive stress across a fracture increases in a power-law fashion; the ratio of the change in fracture hydraulic conductivity to the change in normal stress is between zero and one. The hydraulic conductivity along fractures oriented radially to the drift should decrease by less than 10% as averaged over a 6-m distance from the drift. The absolute magnitude of the normal stress changes parallel to the drift are small (<15%) and average to zero around the perimeter of the drift. There should be little direct effect on the inflow along drift-perpendicular fractures (i.e. the longest H zone fractures). The excavation of the drift causes the compressive stress normal to the drift walls to be reduced to atmospheric pressure and pre-existing fractures that ring the drift should open. Although this should cause the hydraulic conductivity to increase, these fractures would not be oriented to conduct water into the tunnel. Elastic stress changes should have little effect on fracture conductivity along the H-zone near the Validation drift and are unlikely to account for the inferred 8-fold decrease in flow near the drift.

2 INTRODUCTION

In many places and in diverse rock types, fluids flow primarily along fractures. Fractures commonly are not sufficiently interconnected for the rock to behave as a porous medium, even where fractures appear to be numerous (Billaux *et al.*, 1989; Long *et al.*, 1989). As a result, porous media models may not reliably describe the localization of flow or fracture flow rates; in some cases they severely underpredict flow velocities. In certain situations, fracture flow must be considered explicitly as part of a hydrologic characterization effort.

Work at several sites around the world has demonstrated that fracture systems can dominate the hydrologic behavior of a rock mass. For example, at the SCV test block in the Stripa mine in Sweden, fracture zones in the granite occupy no more than 4% of the rock volume encountered by boreholes yet account for 94% of the hydraulic transmissivity (Olsson *et al.*, 1989). Most of the water-producing intervals in boreholes at Yucca Mountain also are associated with fracture zones (Geldon, 1989, written communication). These observations suggest that gathering information on the prominent fracture zones at a site (as opposed to every individual fracture) may be an efficient way to help characterize the hydrology at a given site.

The purpose of this report is to present geologic evidence that can be used either to help build or to test a hydrologic model of the Stripa Site Characterization and Validation (SCV) block at Stripa. Ideally geologic information can contribute to a comprehensive hydrogeologic modeling effort in two main ways. First, although many hydrologic models may fit the available hydrologic data equally well, some will be inconsistent with the site geology. A model of the site geology can reduce the number of hydrologic models that must be examined. Second, a geologic model can help guide a hydrologic characterization effort by identifying critical areas where hydrologic tests might be conducted to assess the validity of competing hydrologic models. At Stripa, fluid flow is considered to be concentrated within fracture zones, the locations of which have been inferred primarily on the basis of geophysical data. The focus of this report is thus not on the locations of the zones, but rather on the internal makeup of the fracture zones, how flow may occur within them, and how the elastic effects of drift excavation are likely to affect flow into the drift. A concerted effort is made in this report to show that regional geologic work can be meshed with subsurface driftwall observations and borehole observations to produce a coherent picture of the current state of fracturing and of fracture evolution; this is the central thread that runs through the report.

3 THE STRIPA MINE AND THE SCV SITE

Since 1977, the Stripa mine in Sweden has hosted a variety of experiments directed towards improving our ability to characterize fractured rock and understand fracture flow. The mine is located about 170 km WNW of Stockholm (Fig. 3.1) and 13 km north of the town of Lindesberg. It had been one of the world's oldest operating iron ore mines; between the middle of the 15th century and 1977 approximately 60 million tons of ore were removed from the mine (Carlsten, 1985). The Stripa mine has functioned purely as a research mine since 1977. Approximately 25 km of drifts exist at the mine, the deepest extending to 430 m below the surface.

The SCV (Site Characterization and Validation) block, the object of this report, is located at the far northeastern part of the mine. Locations in the mine are described by a right-handed coordinate system. The x, y and z directions correspond to "mine north", "mine east" and "down," respectively; mine north is 10° west of true north. The mine level is 30 m greater than the depth below the surface (McKinnon and Carr, 1990, p. 7), so, for example, the 360 level would lie 330 m below the surface. The SCV block as defined by Olsson *et al.* (1989) is bounded by the planes x = 400 m, x = 550 m, y = 1000 m, y = 1150 m, z = 310 m and z = 460 m (Fig. 3.2 and Appendix 1). The SCV block thus is a cube with sides 150 m long. This report describes fracture systems exposed in the vicinity of the SCV block in drifts at the 310-, 360-, 385- and 410-m levels (Fig. 3.2). Most of the drifts shown in Fig. 3.2 are nearly horizontal; three are inclined. Both the validation drift and the validation access drift are inclined. The SE end of the validation drift and the NE end of the validation access drift lie at the 385 level. The validation drift is inclined down to the WNW at approximately 3°. The validation access drift is inclined down to the SW at approximately 14° and its SW end is approximately at the 410 level. The third inclined drift extends up and NW from the 3-D access drift (from near x = 300, y = 1050) to drifts at the 335 level west of the SCV site.

The hydrologic tests at the SCV site relied primarily on four sets of boreholes designated W, N, C and D (Fig.3.2 and Appendix 2). The two W holes (W1 and W2) trend to the west from the 3-D migration drift and are inclined down at angles of 4-5°. They effectively lie in the same plane. Holes N2, N3, and N4 are very nearly parallel (all are inclined 18° down to the north), but the three are not coplanar. N4 was bored from the top of the inclined drift, N3 from the 3-D access drift, and N2 from the northern crosshole access drift. The five C-holes extend down to the west or northwest from a common point near the mouth of the W1 hole and range in inclination from 15° to 43°. Any pair of C holes would be coplanar. Finally, the six D-holes were drilled along a bearing of 288° at an inclination of 3° (down to the west). These holes were designed to lie along the surface of a cylinder with a diameter of approximately 2.5 m. The Validation drift has been excavated along these holes.

Before proceeding further we clarify the use of some terms used in this report. A fracture (i.e. a geologic structural discontinuity) is classified as either a fault or a joint depending on whether there is clear evidence for or against appreciable shear displacement across it. The term "joint" is used where there is evidence for a lack of appreciable shear displacement across a fracture and the term "fault" is used where there is clear evidence of appreciable shear displacement. The term "fracture zone" refers to an extensive tabular body of highly fractured rock.

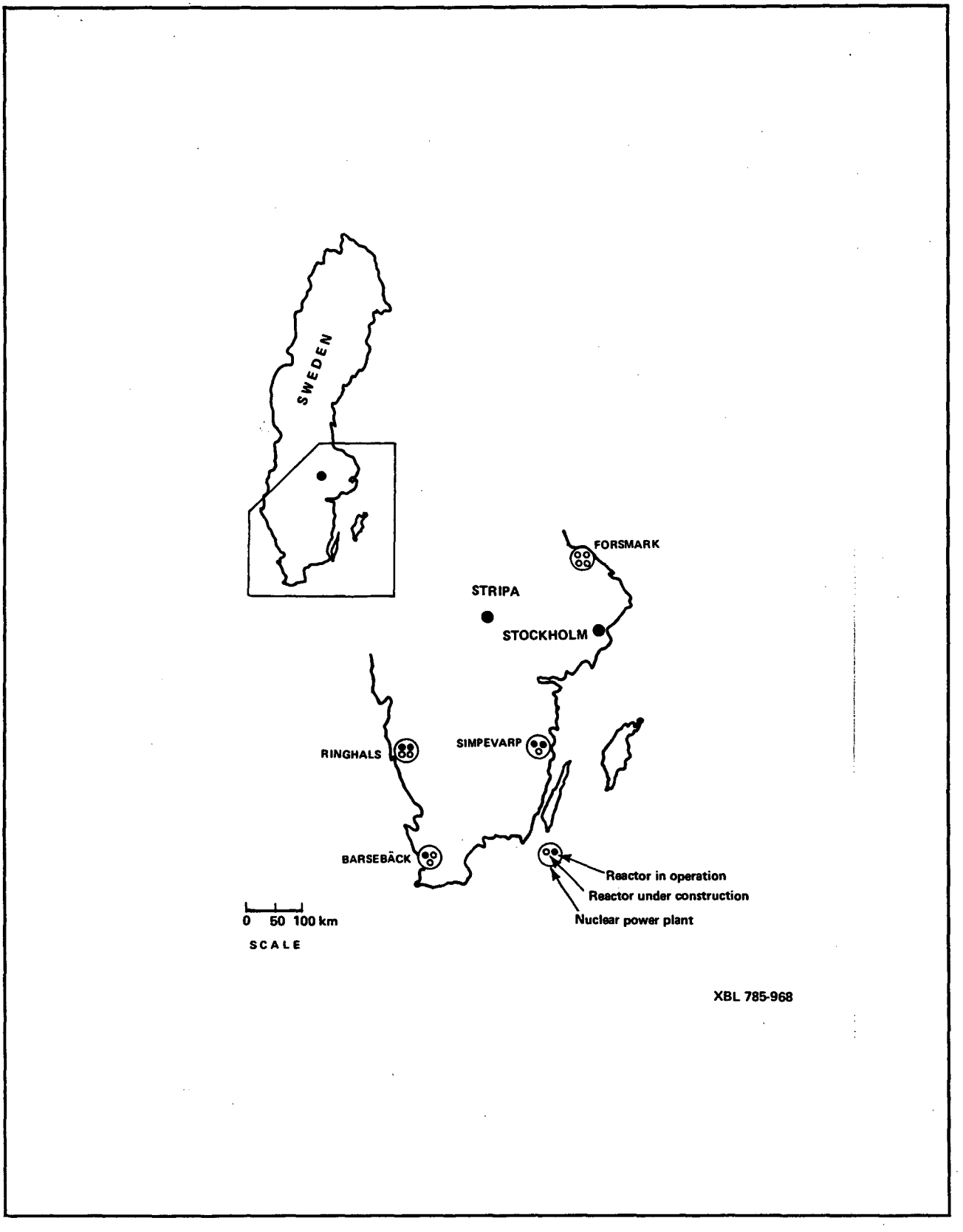

Figure 3.1. Map showing the location of the Stripa mine.

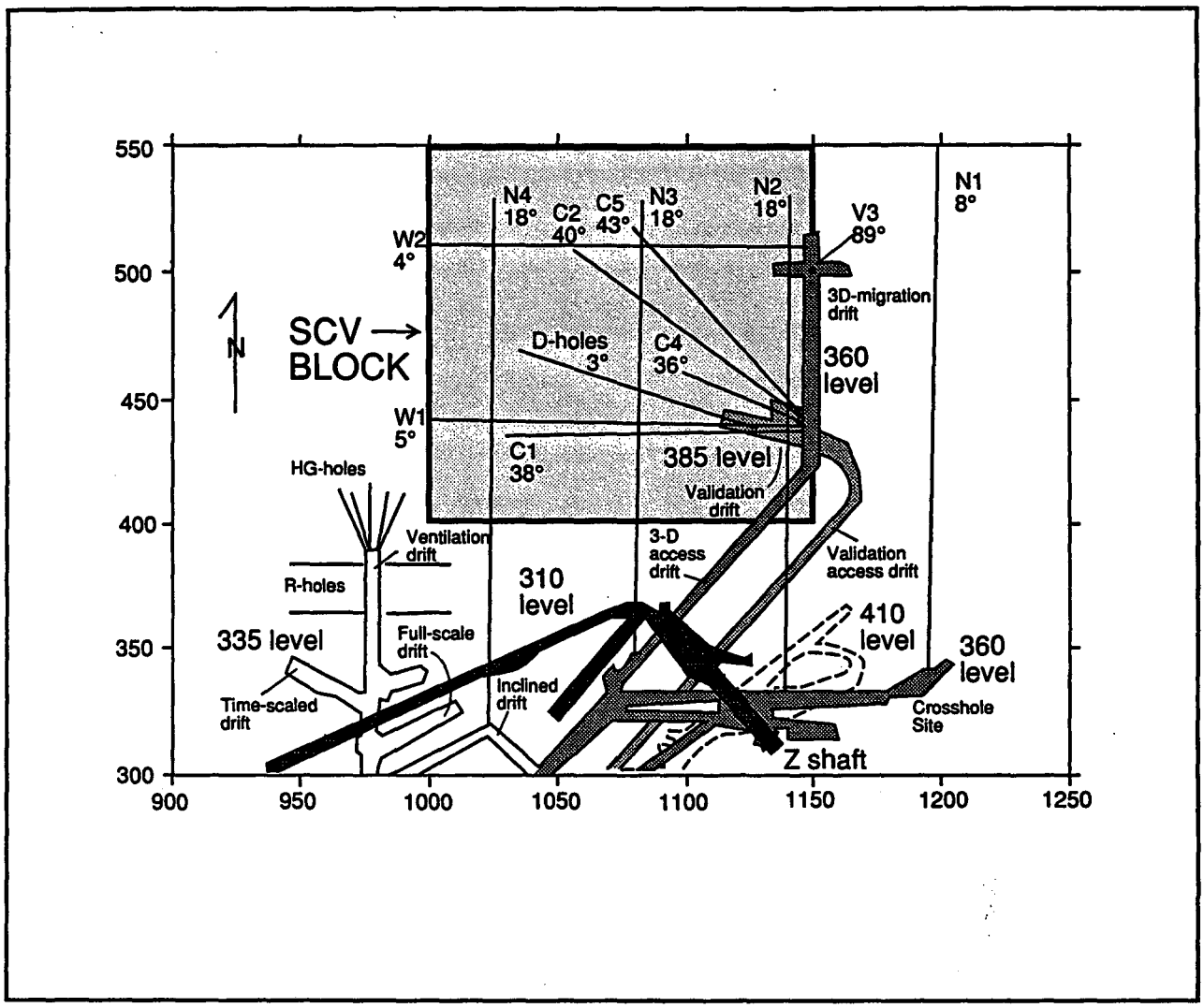

Figure 3.2. Map showing the location of drifts and boreholes near the SCV block at the Stripa mine. Boreholes and drifts are projected orthogonally onto a horizontal plane. Angles denote overall inclination of the boreholes and are rounded off to the nearest degree. Borehole C3 is not shown; it projects along the line of the D-holes. The north arrow points in the direction of mine north.

4 REVIEW OF THE GEOLOGY AT STRIPA

4.1 Summary of Local Geologic History

4.1.1 Svecokarelian crystalline basement rocks

The Stripa mine lies in the Bergsalgen district of central southern Sweden. Bergsalgen rocks share an affinity with rocks that extend west from the Baltic Sea to the Protogine zone (Welin, 1990), an ancient north-striking zone of deformation about 70 km west of Stripa (Fig. 4.1).

Metamorphosed rocks and plutonic rocks formed during the Svecokarelian orogeny (1.6 - 2.0 Ga) constitute most of the Bergslagen basement rocks (Lundqvist, 1979; Olkiewicz *et al.*, 1979; Wollenberg *et al.*, 1980; Carlsten, 1985; Carlon and Bjurstedt, 1990; Welin, 1990). The oldest rocks exposed in the district, and the oldest rocks at Stripa, are metamorphosed volcaniclastic rocks (schists, hälleflintas, and leplites) and carbonate rocks (Fig. 4.2). The sedimentary protoliths for these rocks were deposited more than 2 billion years ago. These rocks were folded 1.85–1.95 billion years ago and again approximately 1.8 billion years ago. Two ages of Svecokarelian plutons are recognized. The older plutons (termed synorogenic or gnejsgranit in the Swedish geologic literature) were intruded during the older episode of folding and are locally foliated (Olkiewicz *et al.*, 1979). The younger (serorogenic) suite of plutons were intruded during the second half of the Svecokarelian orogeny. Except for dikes, which are discussed below, these plutons are the youngest of the basement rocks that are widely exposed in central southern Sweden. The Stripa granite is among the youngest plutons; Wollenberg *et al.* (1980) dated muscovite from the granite at 1691± 16 m.y. using potassium-argon methods.

4.1.2 Post-Svecokarelian tectonic history

Post-Svecokarelian tectonic events

Quaternary glacial, alluvial and lacustrine deposits mantle most of the Bergslagen basement rocks at the surface. Other than these deposits and igneous dikes, geologic units younger than 1.6 billion years are scarce. This pronounced gap in the geologic record between the end of Svecokarelian time and the beginning of the Quaternary period presents many difficulties in establishing the tectonic history of central southern Sweden over the last 1600 m.y. Examinations of dikes, fracture systems, and shear zones suggest that the region has been tectonically active since Svecokarelian time; establishing a tight tie between local deformation and major Scandinavian tectonic events is somewhat problematic however. A key theme that does emerge in studies of southern Sweden (and of Scandianavia as a whole) is that deformation has been repeatedly localized along ancient (Precambrian) fault zones or shear zones (Talvitie, 1979; Röshoff, 1979; Mörner, 1979; Erlstrom, 1987; Lopez-Montano and Nisca, 1987; Talbot and Heeroma, 1989; Talbot and Munier, R., 1989, Tirén and Beckenholm, 1989; Bäckblom and Stanfors, 1989; Andréasson and Rodhe, 1990; Talbot, 1990). Post-Svecokarelian tectonic events in which Precambrian basement fracture zones were reactivated include the Sveconorwegian orogeny at 850-1200 Ma (Daly *et al.*, 1983; Andréasson and Rodhe, 1990) and the Caledonian orogeny at approximately 400–510 Ma (Dallmeyer *et al.*, 1985; Dallmeyer and Gee, 1986; Simon, 1987; Dallmeyer *et al.*, 1990). Talbot and Slunga (1989) suggest that Swedish fault zones have also been reactivated in association with the opening of the Norwegian Sea in the last 50 million years. Ancient faults have also been reactivated since the retreat of Pleistocene glaciers (Bäckblom and Stanfors, 1989).

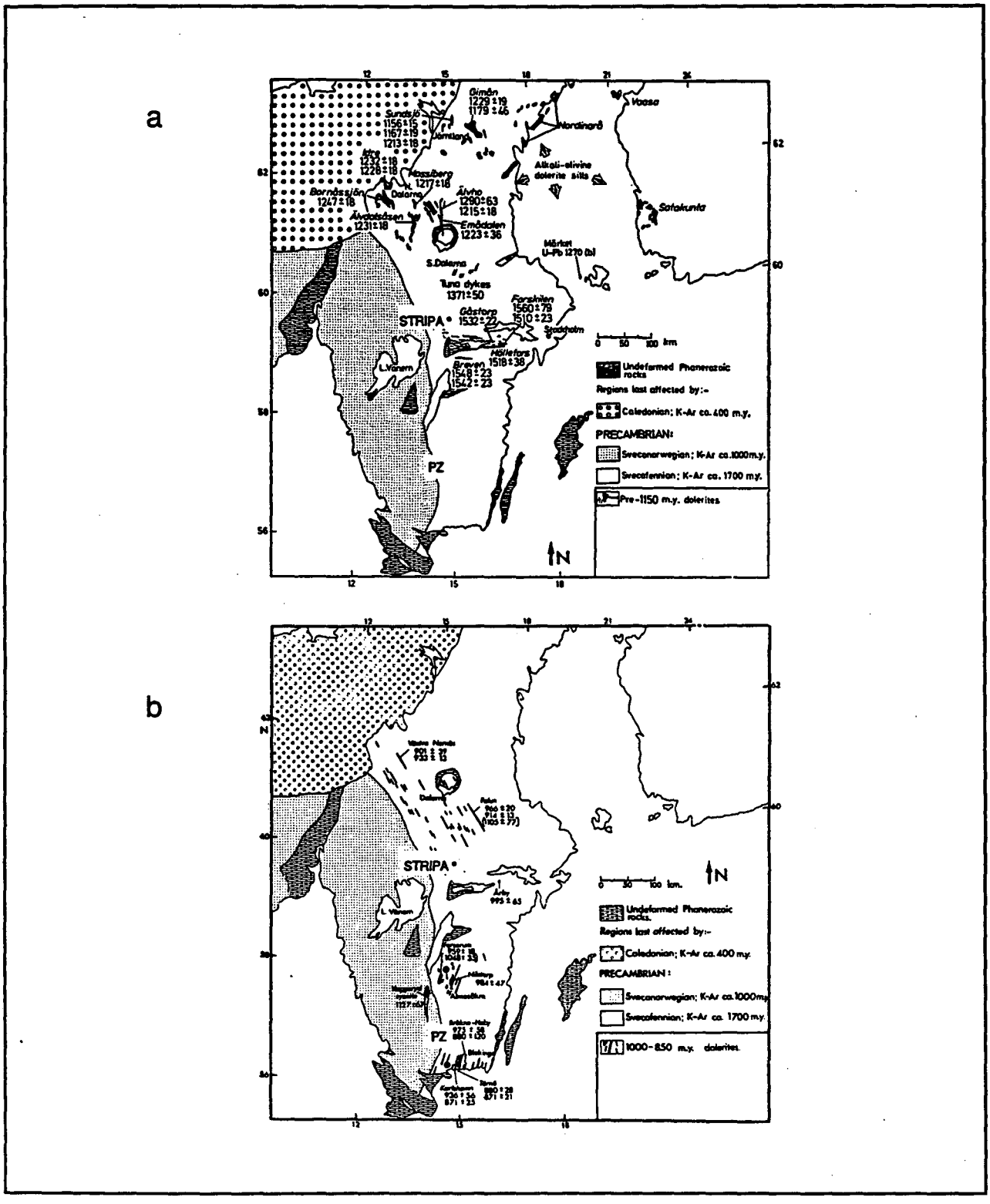

Figure 4.1. Generalized geologic map of southern and central Sweden showing dolerite intrusions a) older than 1150 Ma and b) younger than 1150 Ma (modified from Patchett, 1978). The Protogine zone (PZ) lies along the boundary between rock assemblages labeled Sveconorwegian and Svecofenninan (Svecokarelian). The lake southeast of Lake Vänern is Lake Vättern.

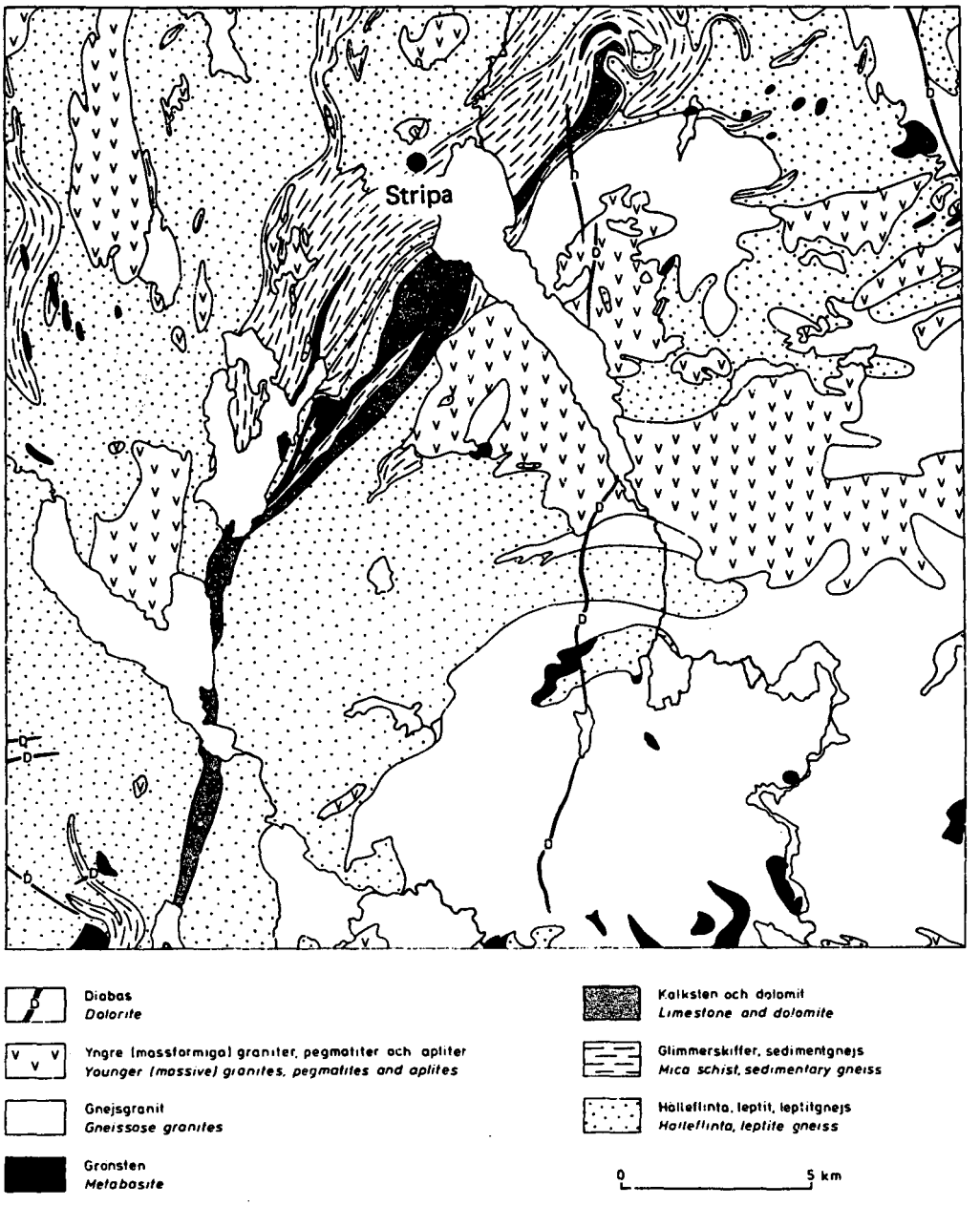

Figure 4.2. Geologic map of the Lindesberg SV quadrangle (from Olkiewicz *et al.*, 1979).

Regional fracture patterns

The regional pattern of fractures (i.e. joints, faults, and dikes) in the Bergslagen district is expressed by geomorphic lineaments which have been investigated at a variety of scales. Lineaments of numerous orientations occur at the scale of the district (Fig. 4.3). In the general vicinity of Stripa, Carlsten (1985) concludes that the lineaments trend primarily NNW or E-W. However, Tirén (see Black *et al.*, 1991) interprets the most prominent lineaments in a 400 km^2 area about Stripa as trending NE, with subordinate sets trending E-W and N-S (Fig. 4.4). A more-tightly focused map of a 48 km^2 area about Stripa (Fig. 4.5) shows the longest lineaments trending NW. According to Carlsten (1985) the regional NNW set is less pronounced on Fig. 4.5 than in adjacent areas and the regional E-W set is not present at all. Figure 4.5 shows two linear features about 3 km long intersecting near the Stripa mine; one (inferred from aeromagnetic work) trends at 353°, the other E-NE. At an even finer scale, 75% of the 26 linear features measured at the ground surface above the mine "in the immediate area of the granite outcrop" trend NE or NNE (Olkiewicz *et al.*, 1979, p. 14). Based on the work cited above, it is clear that a broad spectrum of fracture orientations exists in the Bergsalgen district. One also could conclude that the dominant fracture orientation near the Stripa mine varies as a function of scale. The fracture systems expressed at the surface at Stripa do not fit neatly into a simple regional pattern; at least some of the major fracture systems at the Stripa mine could potentially be restricted to the Stripa pluton.

Dikes

One way that post-Svecokarelian deformation is manifest is by patterns of dikes. Patchett (1978) has established three broad periods of post-pluton dolerite dike intrusion east of the Protogine zone (dolerites are pyroxene-rich rocks of basaltic composition). Patchett used single-sample Rb-Sr mineral methods for dating. The oldest dikes (Fig. 4.1a), those of the Breven-Hällefors dike swarm, were intruded at approximately 1530 Ma. The dikes strike roughly E-W and dip steeply (Patchett, 1978; Wikström, 1985). They are located WSW of Stockholm, with the north edge of the swarm being 20-30 km south of Stripa. The second major episode of dike intrusion is manifest by the Tuna dikes; these were intruded at approximately 1370 Ma. The Tuna dikes strike NNE and are located near Falun, about 70 km north of Stripa. The third and youngest set of dikes (Fig 4.1b) range in age from 850–1000 Ma. These dikes generally strike parallel to the Protogine zone, striking NNE near the southern part of the zone and NNW near the northern part of the zone. In addition to the dikes, Patchett has calculated a mean age of 1218±18 Ma for thirteen dolerite sills in central Sweden. Patchett interprets the ages of these dikes and sills as reflecting ages of intrusion.

Three groups of mafic dikes can also be distinguished on the geologic map of the Lindesberg SV quadrangle. The oldest set (not shown on Fig. 4.2) consists of metamorphosed dikes that strike ENE to ESE. These dikes intrude the older suite of plutonic rocks but apparently predate the younger suite of plutons, so although they are subparallel to dikes of the Breven-Hällefors dike swarm, they would be distinctly older. The second and third sets are shown on Figure 4.2. This second set strikes E to NE. Although this set is considered to be post-date the younger suite of plutons, no dikes of this orientation are shown cutting the younger plutons. The third set strikes approximately N-S, contains some dikes more than 50 m thick, and cuts the plutons of the youngest suite. Lopez-Montano and Nisca (1987) consider these north-striking dikes to belong to the youngest set of dikes defined by Patchett (1978).

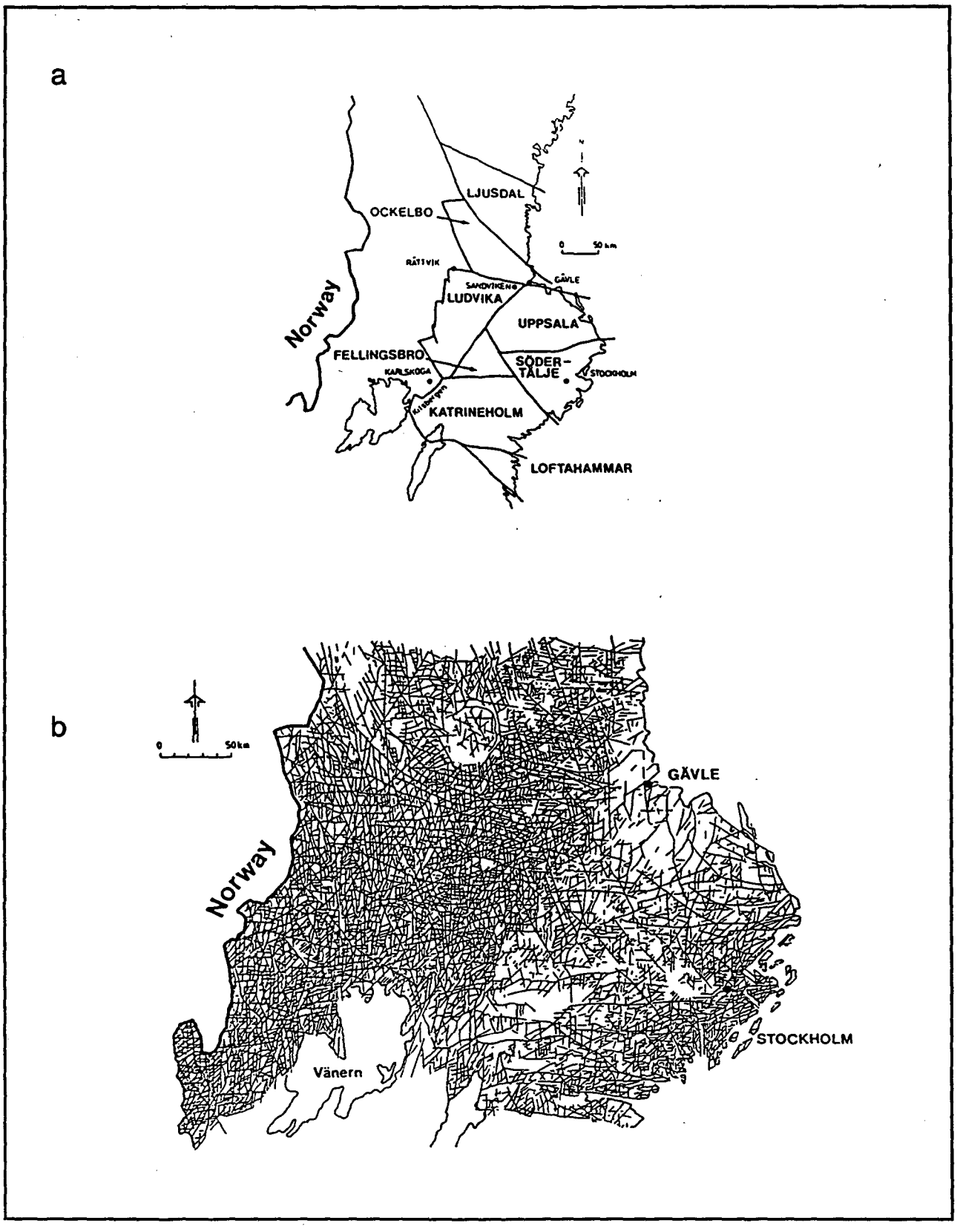

Figure 4.3. a) Rock block map of the Bergslagen district and surrounding environs (from Tirén and Beckenholm, 1990, p. 198). Lines denote geomorphic lineaments.

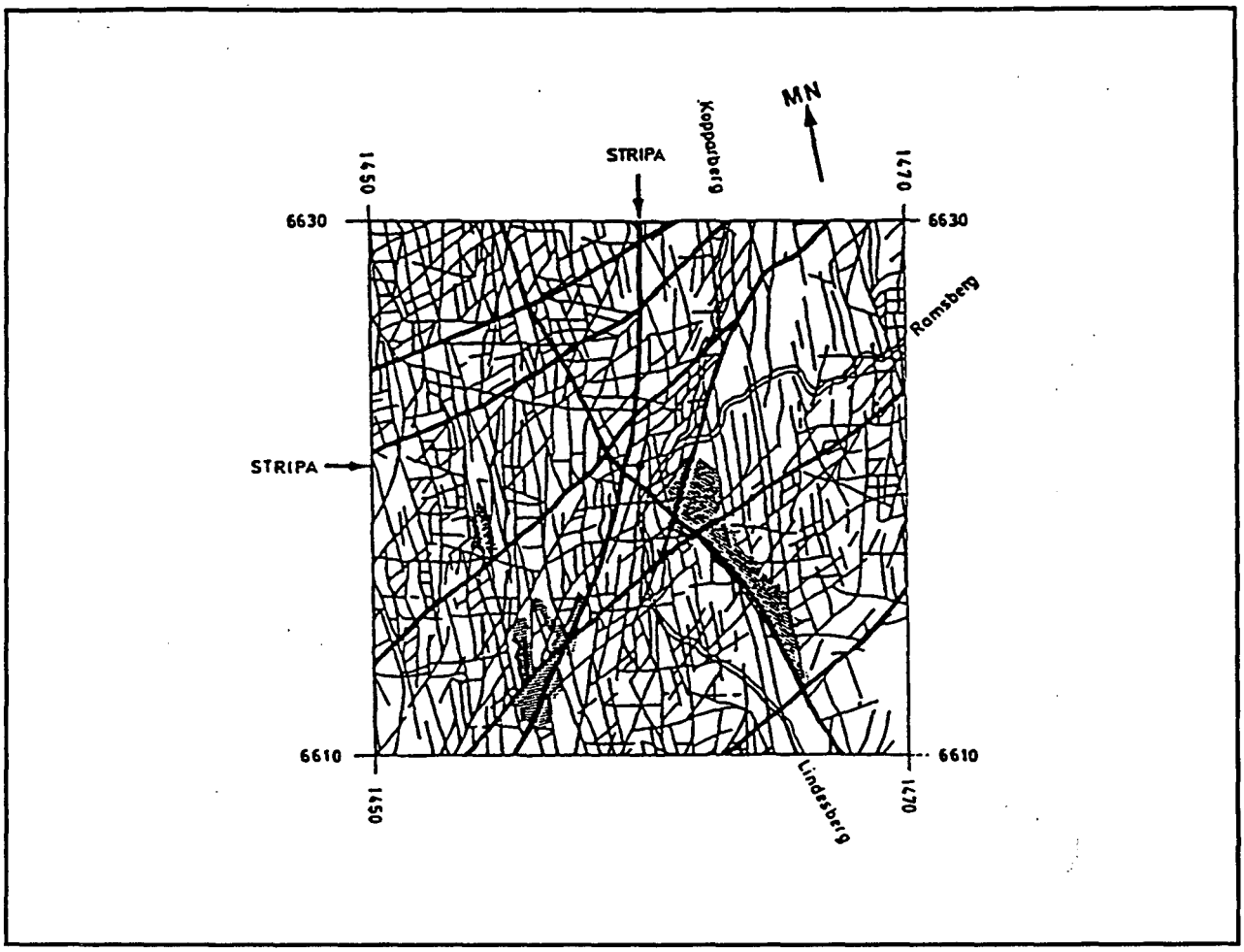

Figure 4.4. Lineament map of a 400 km^2 area centered about the Stripa mine (from Black *et al.*, 1990, p. 197). Lakes are shown in grey. This figure was prepared using a computer-assisted terrain analysis with the direction of synthetic "illumination" being from the northwest. This "illumination" direction would preferentially emphasize northeast-trending features.

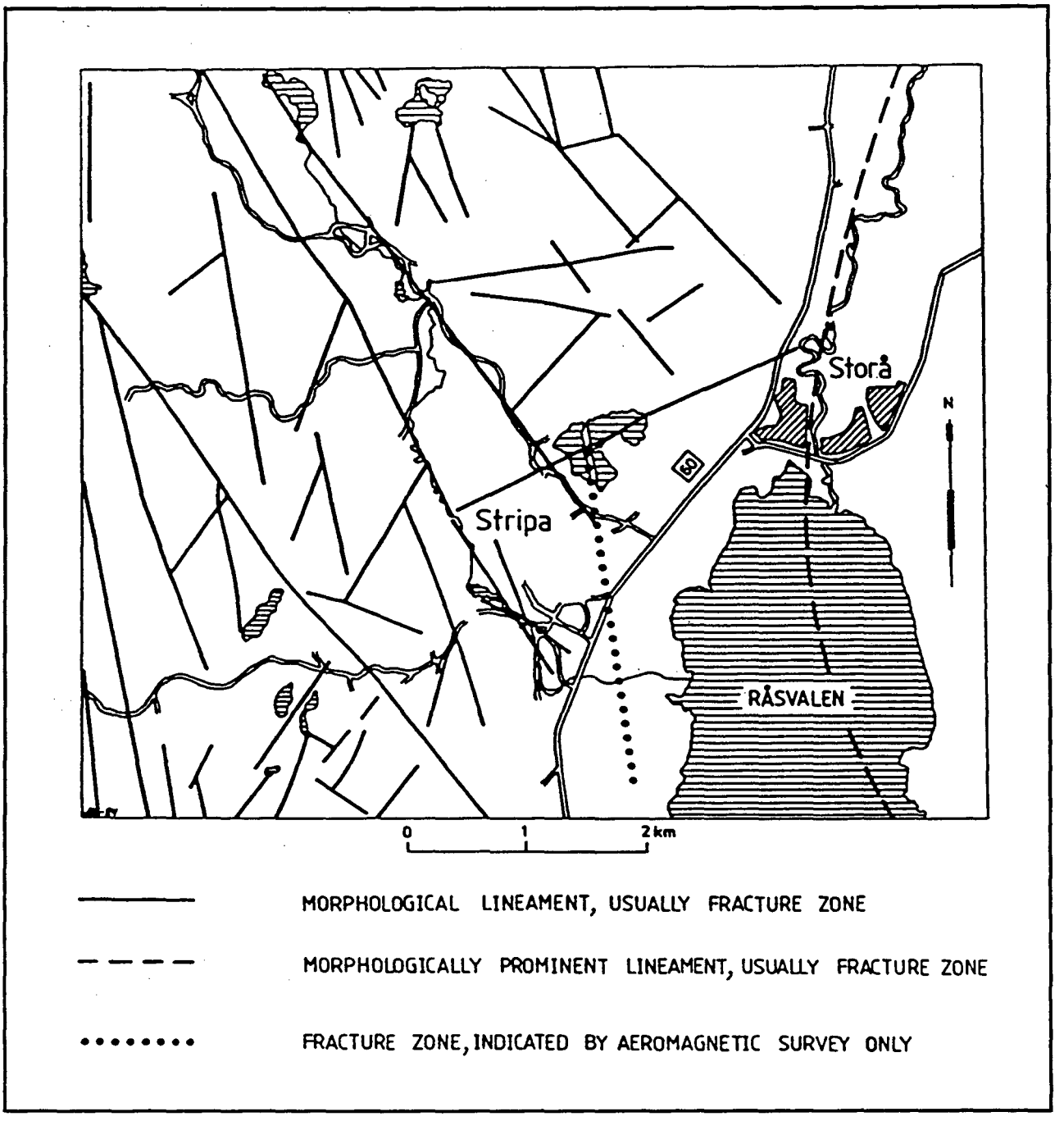

Figure 4.5. Lineament map of a 48 km^2 area about the Stripa mine (from Carlsten, 1985, p. 34).

The dikes described above 1) have fairly constant orientations over large distances, 2) mostly cut rather massive rocks, and 3) maintain their orientation independent of the character of the host rocks. These observations indicate that the dike orientations were controlled either by pre-existing fractures of regional extent or by strongly anisotropic regional stresses at the time of dike intrusion. Patchett (1978) notes that prominent fractures east of the Sveconorwegian fault zones (i.e. Protogine zone) commonly parallel dolerite dikes, but there has not yet been sufficient detailed study of the type outlined by Delaney *et al.* (1986) to establish in general whether the dikes pre-date, post-date or accompanied the formation of these fractures. However, if the dikes themselves do not reflect strongly anisotropic regional stresses at the time of their intrusion, then the pre-existing fractures the dikes must have intruded would reflect strongly anisotropic regional stresses at the time the fractures formed. The metamorphosed dikes of the Lindesberg quadrangle thus reflect at least one episode of *pre*-serorogenic fracturing during which the least compressive horizontal stress was oriented approximately N-S. This fracturing event would pre-date the intrusion of the Stripa pluton. The Lindesberg dikes that strike E to NE might represent a second dilation of those pre-serorogenic fractures. The north-striking dolorite dikes of the Lindesberg quadrangle reflect at least one episode of *post*-serorogenic fracturing during which the least compressive horizontal stress was oriented approximately E-W. This fracturing event, which affected much of southern Sweden, would post-date the intrusion of the Stripa pluton and most likely occurred during or prior to the interval from 850 Ma to 1000 Ma.

Faulting along the Breven-Hällefors dike swarm could also have occurred during the opening of regional north-striking fractures. Wikström (1985) and Lopez-Montano and Nisca (1987) show NW-striking faults offsetting dikes of the Breven-Hällefors dike swarm (as well as older leptite units) in a right-lateral sense. Lopez-Montano and Nisca also show left-lateral slip on faults that strike NE, and Wikström also notes vertical displacements of some of the dikes across faults that strike N-S. The faulting could have occurred contemporaneously when the most compressive stress was vertical, the most compressive horizontal stress was oriented N-S, and the least compressive horizontal stress was oriented E-W. If the lateral separations reflect only strike slip and not dip slip, then right-lateral slip along the northwest-striking faults is also required before the dikes were intruded in order to account for the offset of the leptites.

The Protogine zone

The Protogine zone (Fig. 4.1) is one of the most prominent ancient zones of deformation in Sweden, and it reflects a long and complicated history of deformation. It is several hundred kilometers long, has a maximum width of 30 km (Andréasson and Rodhe, 1990), and passes about 80 km west of Stripa. The zone extends north from near the southern tip of Sweden, along Lake Vättern and the northeast end of Lake Vänern, and up along the Klaralven River into Norway, where it is cut off or concealed by rocks of the Caledonian fold belt. The Protogine zone consists of a series of steeply-dipping, anastomosing fault zones and narrow shear zones that range in strike from NNW to NNE (Andréasson and Rodhe, 1990). Numerous north-striking dolerites intrude the zone and the rocks adjacent to it; the zone also contains the 60-km-long Vaggeryd syenite body (Klingspor, 1976; Patchett, 1978; Lundqvist, 1979; Andréasson and Rodhe, 1990).

Field observations indicate that the Protogine zone has experienced multiple episodes of deformation. Larson *et al.* (1986) documented several generations of superposed folds and deformation fabrics in rocks in and along the zone. Lundqvist (1979) noted that some Protogine dolerites are strongly deformed and metamorphosed, whereas others show little sign of metamorphism, indicating that dikes were intruded along the zone in at least two different periods. Members of the

older set of dikes have experienced two episodes of folding (Lundqvist, 1979). Along the southern half of the zone, offset markers and S-C rock fabrics indicate that left- and right-lateral strike slip as well as dip slip displacement have occurred across north-striking faults and shear zones within the Protogine zone, with the imprint of normal slip being pronounced (Andréasson and Rodhe, 1990).

Radiometric ages from intrusions along the Protogine zone vary over a broad range, but interpreting the ages in terms of times of intrusion or slip along the zone is complicated by the effects of a pronounced thermal event of Sveconorwegian age (Magnusson, 1960; Welin and Blomqvist, 1966). Priem *et al.* (1968) dated five dolerite dikes from the Protogine zone using K-Ar whole rock techniques. The ages clustered into two sets, one at 800-900 Ma, the other at 1500-1600 Ma. They considered the group with the greater age to reflect an episode of dike intrusion and the group with the lower age to reflect a reheating event. Klingspor (1976) obtained a whole-rock Rb-Sr isochron age of 1600±230 Ma from fourteen Protogine dolerite samples. She also dated thirty seven Protogine dolerite samples using K-Ar whole-rock and K-Ar mineral-separate analyses. Her K-Ar ages are distributed between 800 and 1500 Ma, with clusters at ~1200 and ~900 Ma. She interpreted her results to reflect an episode of intrusion at 1450-1600 Ma and a reheating event at 900-950 Ma rather than successive intrusion events over a 700-800 m.y. span. Klingspor considered all of her samples with dates less than ~1450 m.y. to have been affected by reheating. In contrast, Andréasson and Rodhe (1990) and Bylund (1992) consider the dike age clusters of ~1500 Ma, ~1200 Ma, and ~900 Ma to represent separate dike intrusion events, the younger two events being Protogine zone counterparts to dolerites east of the zone dated by Patchett (1978). Even where constraints have been placed on the timing of some of the deformation along the Protogine zone, the constraints are broad. Patchett (1978) interpreted his Rb-Sr dates on whole-rock, on metamorphic muscovite, and on metamorphic biotite samples from the deformed Vaggeryd syenite to reflect an intrusion age of ~1130 Ma and a Rb-Sr thermal closure age of the micas of approximately 900 Ma. These ages would bracket the time of deformation above 300°-500° C for the syenite, but they do not constrain deformation of the dolerites. In light of actual or potential overprinting effects due to the Sveconorwegian thermal event and to dolerite dike intrusion, additional careful dating seems necessary to establish the timing of pre-Sveconorwegian faulting episodes in the Protogine zone.

Although most of the fracturing along the Protogine zone is of Precambrian age, some fracturing has occurred subsequently (Röshoff, 1979). Andréasson and Rodhe (1990) note that steep north-striking faults of the zone can be mapped out into Vättern graben sedimentary units with an age of ~700-800. Some Jurassic intrusions occur along the southern part of the zone (Hjelmqvist, 1975; Klingspor, 1976), and faulting is cited along the zone in Permian, Jurassic, and late Quaternary times (Mörner, 1979).

As a tectonic feature, the Protogine zone has been considered to represent an ancient crustal suture zone based on plate tectonic reconstructions (e.g. Zeck and Mallin, 1976) or to be a major intraplate thrust fault front (Gorbatschev, 1980). Some investigators consider the Sveconorwegian thermal event of ~900 Ma to be associated with uplift of the crust west of the Protogine zone (e.g. Magnusson, 1960; Welin and Blomqvist, 1966; Klingspor, 1976) without specifying whether the uplift was by thrust faulting or normal faulting. Patchett and Bylund (1977) proposed that the dolerite intrusions along the zone occurred contemporaneously with widespread fracturing to the east and uplift of the crust to the west during Sveconorwegian time. Andréasson and Rodhe (1990), reasoning that the presence of normal faults and multiple parallel sets of dikes along one narrow

zone is characteristic of rift systems and not collisonal thrust fronts, suggest that Precambrian deformation along the Protogine zone reflects, at least in part, an episode of regional rifting.

4.1.3 Neotectonics, seismicity, and post-glacial rebound

Regional deformation in Sweden is not restricted to the ancient geologic past. The crust of the region has flexed measurably in isostatic response to the retreat of Quaternary ice sheets. The Swedish crust at the latitude of Stripa has rebounded 500-600 m in the last 13,000 years (Mörner, 1980); the uplift continues to this day. Several faults in Scandinavia displace recent glacial deposits by 10–30 m (Lagerbäck, 1979; Muir Wood, 1989; Bäckblom and Stanfors, 1989).

Much of the historic seismicity and Holcene faulting in the Scandinavian region has occurred along ancient (Precambrian) fault zones or shear zones. Post-glacial faulting in the Lansjärv area of northern Sweden occurred along pre-existing ancient faults (Bäckblom and Stanfors, 1989). Talvitie (1979) has observed that seismicity in Finland is largely concentrated along ancient faults. He has also noted that seismicity is most concentrated where ancient faults intersect each other. Tirén and Beckholmen (1989) argue that ancient north-striking faults along the southeast Swedish coast between Västervik and Oskarshamn have been reactivated repeatedly. They note that maps of relative post-glacial uplift show relative-uplift contours that trend N-S in that area, and they infer that post-glacial slip has occurred along some north-striking faults. Historical seismicity has also been concentrated in the area where the Protogine zone passes beneath Lake Vättern (Stephansson, 1979).

4.1.4 Conclusions regarding post-Svecokarelian fracturing

The fracture patterns near Stripa are complex, as they are for southern Sweden as a whole. These patterns reflect the cumulative effects of deformation over a period of at least 1.6 billion years. Many ancient Swedish fracture zones have been reactivated during this period, and some are actively deforming now. Given the occurrence of distinctly different regional orogenic events and the existence of dike sets of different ages and orientations, episodes of fracturing (and fracture reactivation) must have occurred under distinctly different regional stress fields. At least one fracturing event of regional extent has left a strong imprint on the youngest plutons near Stripa. This event occurred during or prior to the interval from 850 Ma to 1000 Ma and is reflected by the opening of steeply-dipping fractures that strike N-S.

4.2 The Stripa Granite

The two main rock types at the Stripa mine are layered metamorphic rocks (collectively referred to as "leptites") and the Stripa granite (Olkiewicz *et al.*, 1979). The leptites are the older rocks and contain the iron ore at the mine. The leptites occupy a synclinal fold that dips gently to the ENE (Olkiewicz *et al.*, 1979). The SCV block is located in the Stripa granite, which intrudes the leptites, below the north limb of the syncline. The generally massive nature of the granite has been interpreted to reflect a low level of plastic deformation in the granite since its emplacement (Carlsten, 1985).

The size and shape of the Stripa pluton are not well resolved. The Stripa granite is exposed at the surface amidst glacial deposits over an area of approximately 4000 m^2 (Olkiewicz *et al.*, 1979); this provides a minimum area for the granite at the surface. A borehole at the mine shows that the

pluton extends to a depth of more than 1.2 km (Carlsson *et al.*, 1982). Heat flow calculations indicate that if the Stripa pluton formed an extensive horizontal layer it would most likely be less than 1.5 km thick, but the available data on pluton geometry are sparse and do not require the Stripa pluton to be a sheet-like body (Wollenberg *et al.*, 1980). According to Olsson *et al.* (1989) the contact between the leptite and the granite has been identified in the subsurface only along mine workings on the south side of the pluton, but no mention is made of the nature of the contact there. The nature of the granite-leptite contact is not well constrained based on the surface exposures. Nearby plutons of comparable age to the Stripa granite typically intrude their host rocks conformably (Olkiewicz *et al.*, 1979); that is, the pluton boundaries typically parallel layering in the host rocks. Although the contact between the Stripa granite and the leptites could be subparallel to layering in the leptites (Carlsten, 1985), a wide variety of shapes for the Stripa pluton are permitted based on the data at hand. The available information on the geometry of the Stripa pluton is so limited that it cannot be used to infer possible fracture geometries within the pluton.

The granite is generally grey or pink, massive, and medium-grained. For the most part the granite is low in iron relative to other nearby plutons (Wollenberg *et al.*, 1980; Carlsten, 1985). Locally, however, the granite is red due to the presence of finely disseminated hematite (Carlsten, 1985). Hematite is the primary iron ore mineral in the leptite, so the granite may have been colored by hematite derived from the leptite. Although the granite is massive on a macroscopic scale, on a microscopic scale the granite is highly fractured and shows abundant evidence for recrystallization due to deformation (Wollenberg *et al.*, 1980).

Fluid inclusions are abundant in the Stripa granite (Lindblom, 1984). The inclusions are overwhelmingly of a secondary (i.e. post-intrusion) nature and occur along healed fractures. The inclusions show a wide range of chemistries, indicating that they formed over a broad range of temperature and pressure conditions. Some fracture fillings contain multiple generations of fluid inclusions, indicating repeated displacements along fractures. In keeping with the microstructural observations, the fluid inclusion data indicate that the Stripa granite has been deformed repeatedly since its emplacement (Lindblom, 1984).

4.3 Previous Mapping of Fracture Systems at the Stripa Mine

A compilation by Olkiewicz *et al.* (1979) of maps and cross sections published between 1938 and 1966 shows that most of the mapping done before the 1970s (i.e. when iron ore was being mined) concentrated on areas south and west of the SCV site, areas where the leptite occurs. Olkiewicz shows dozens of faults with a variety of orientations in the leptite; in this sense the fracture pattern resembles regional patterns. Several faults extend into the granite. Some mapping extended into the granite near the SCV site, but the maps show little detail.

Fractures in the granite have been mapped in detail only since the onset of cooperative work between Sweden and the United States in the late 1970s. Detailed maps of fractures have been made at several places at the 335- and 360-m levels near the edges of the SCV block (Olkiewicz *et al.*, 1979; Thorpe, 1979; Abelin and Birgersson, 1987). Although some of the maps show areas of abundant fractures with diverse orientations, those areas are not shown as being part of extensive fracture zones. A generalized map of the 335 level (Fig. 4.6) reveals that steeply-dipping fractures that strike north and northwest are prominent, and a detailed map of the ventilation drift (Fig. 4.7) shows a 10-m-long fracture zone that strikes north. Driftwall information has also been collected at

the SCV block by Gale and Stråhle (1988) and Gale *et al.* (1990), but this information has been presented in the form of tables rather than geologic maps.

4.4 Fracture Fillings

Wollenberg *et al.* (1980) examined fracture fillings at Stripa in detail and recognized two distinct sets of fracture-filling minerals. Chlorite, quartz, sericite, feldspar, and epidote are the major minerals in the older set. Calcium carbonate is the primary mineral in the younger set. The sets of minerals indicate at least two episodes of fluid flow under distinctly different environmental conditions; these episodes may have been widely separated in time. Interestingly, the detailed descriptions that Wollenberg *et al.* (1980) provide indicate that even where the granite is red (i.e. hematite-bearing) that hematite typically is absent or scarce within the older fractures. This indicates that hematite was introduced into the granite before many (if not all) of the older, chlorite-bearing fractures formed.

In addition to the mineral fillings, two kinds of deformation products are common in fractures at Stripa: breccias and mylonites (Wollenberg *et al.*, 1980, Carlsten, 1985). The presence of breccia (a product of brittle deformation) and mylonites (a product of ductile deformation) suggest that the fracture systems at Stripa contain faults that have been reactivated at different strain rates, temperatures and/or pressures. Some of the breccias contain clay-rich fault gouge. The fracture-filling matrix in some breccia-bearing fractures (faults) is red, suggesting that hematite was remobilized and incorporated into the faults. No recurring cross-cutting relationships have been identified between breccia-bearing and mylonite-bearing fractures to determine their relative age.

4.5 Conclusions Based on Previous Work on Fractures at Stripa

As is the case for the Bergslagen district as a whole, the fracture pattern at Stripa is complex. Fractures of numerous orientations are present, and some of the fractures are faults. The nature of the fracture fillings, fluid inclusions, and the microscopic character of the Stripa granite indicates that the Stripa fractures have opened and/or slipped repeatedly. As is the case for the Bergslagen district, some of the most prominent SCV fracture systems strike N-S, and they appear to dip steeply.

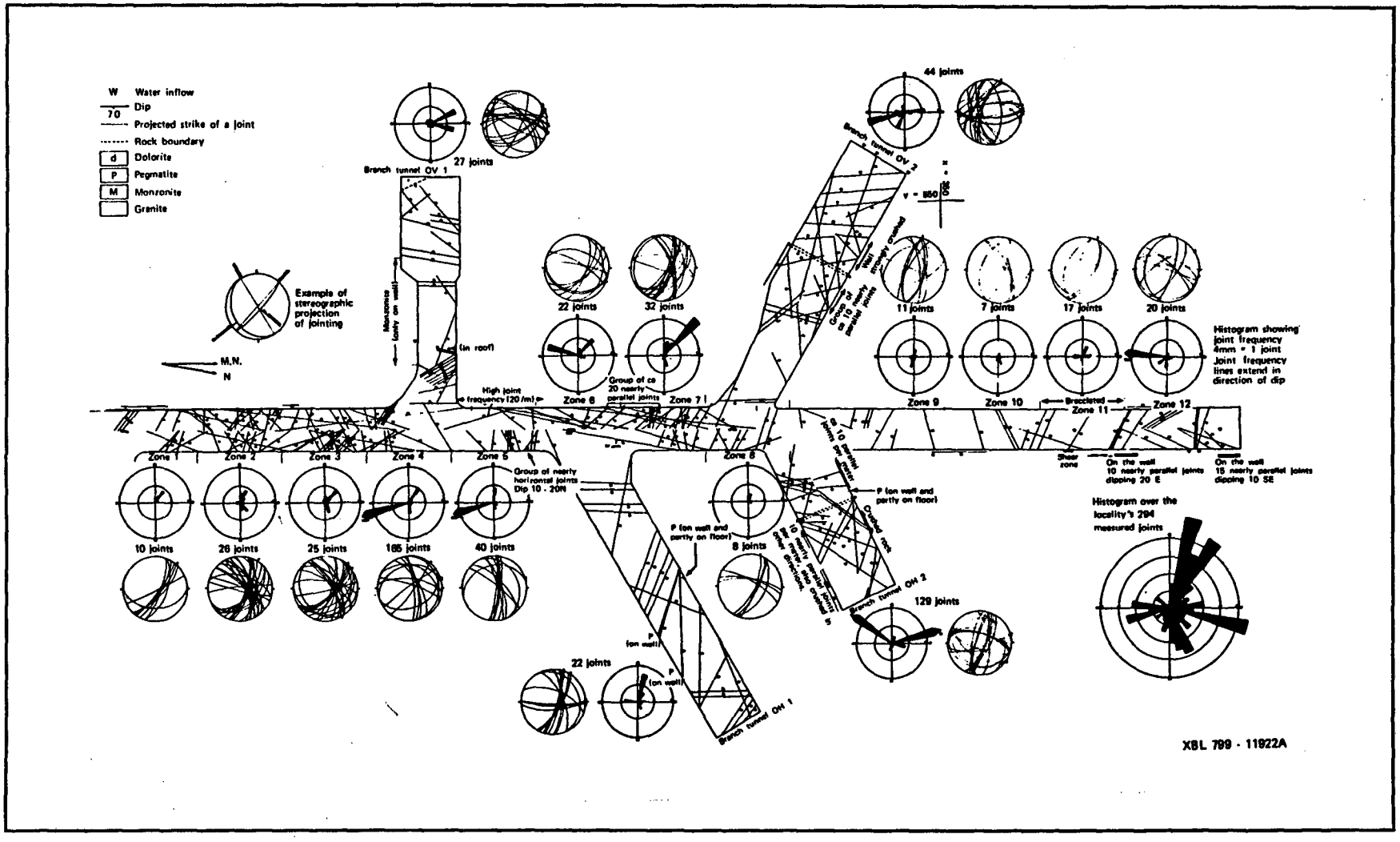

Figure 4.6. Generalized fracture trace map of the 335-level showing the ventilation drift and branching drifts. The northeastern branch drift is the computer room. The southeastern branch drift is the full-scale drift. The southwestern branch drift is the Luleå drift. The northwestern branch drift is the time-scaled drift. From Olkiewicz *et al.*, 1979.

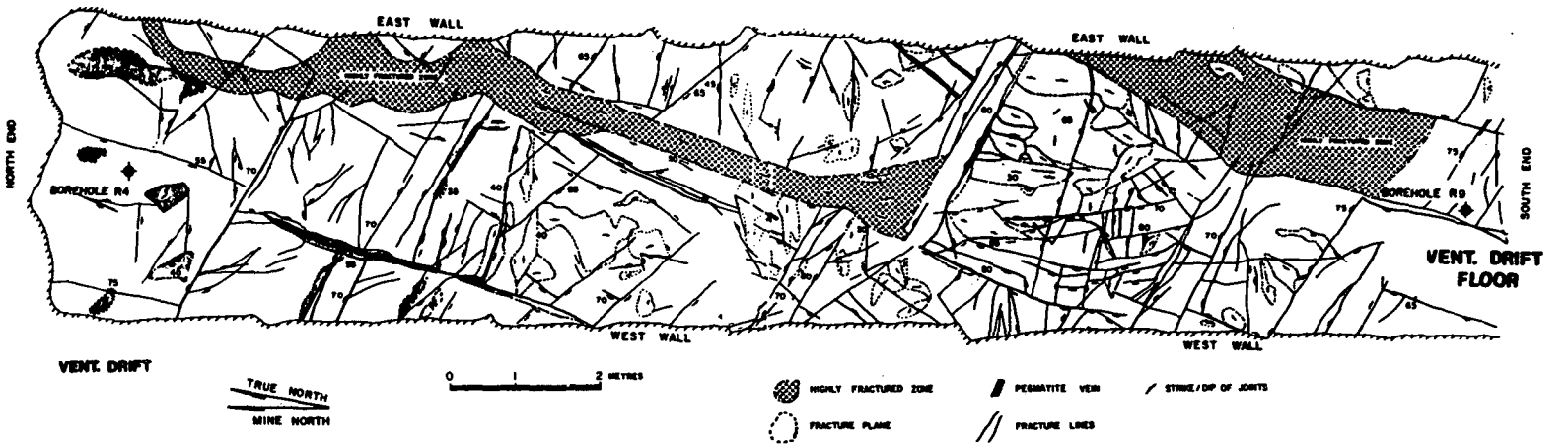

XBL 798-11062

Figure 4.7. Detailed fracture trace map of the north end of the ventilation drift. From Olkiewicz *et al.*, 1979.

5 CONCEPTUAL MODEL OF FRACTURE ZONES AT STRIPA

The conceptual model of the fracture zones at Stripa, as defined in the site characterization report by Black *et al.* (1990), has been constructed principally on the basis of (1) geophysical and hydraulic data collected from single boreholes and (2) geophysical remote sensing techniques. Geophysical information was weighted more than hydraulic data in constructing the model. The single-borehole information was used to identify and define fracture zones at *points* within the SCV block. Weighted single-hole measurements of normal electrical resistivity, sonic velocity, hydraulic conductivity, abundance of coated (open) fractures, and radar reflection values were used to pinpoint fracture zones. The extents and orientations of the fracture zones *away* from boreholes were determined using radar and seismic tomography together with radar and seismic reflection techniques. Where available, directional radar reflection data were relied upon heavily to evaluate fracture zone orientations. The resulting set of fracture zones in the conceptual model do not account for every single-hole anomaly, nor are all the single-hole anomalies that are accounted for perfectly intersected by fracture zones; the focus was on obtaining a "best fit" with as small a number of zones as seemed reasonable. Geologic data were used sparingly in constructing the conceptual model of the SCV site; this reflects the scarcity of bedrock exposures at the surface and the scarcity of immediate geologic data on this relatively deep, remote portion of the mine. For a more detailed discussion of how the conceptual model was constructed and for more information on the geophysical techniques used, one should consult the report by Black *et al.* (1990) and the references cited therein.

The conceptual model of Black *et al.* (1990) contains seven major fracture zones (A, B, H, Hb, I, M and K); these are shown in Figures 5.1, 5.2, and 5.3. Zones M and K were designated as major fracture zones after completion of the field studies conducted for this report. The orientations of the zones and the coordinates of a point in each zone are shown in Table 5.1. The *calculated* intersections of the zones (as defined in Table 5.1) with several boreholes at the SCV site are listed in Table 5.2. The *recorded* intersections of the zones with the boreholes are listed in Table 5.3. A comparison of Tables 5.2 and 5.3 shows a good correspondence between the calculated and recorded values (Fig 5.4). All of the zones have been interpreted to be planar features, but as Olsson *et al.* (1989) note, these zones all have irregular appearances on geophysical tomograms and probably vary considerably in thickness and in their bulk material properties. Deviations from planarity probably account for some of the differences between the recorded and calculated points of intersection.

These zones can be grouped into three sets based on their orientation (Fig. 5.2). Zones H and Hb, which together form the feature with the most prominent geophysical fingerprint, dip steeply to the east, as does zone I. Zones A and B dip moderately to the SE. Zones M and K dip steeply to the NE. Zones H, Hb, A, and B are considered to be extensive and continue well outside the SCV test volume (Black *et al.*, 1990). Of these extensive zones, only zone H (together with Hb) is oriented such that it would intersect accessible drifts within or adjacent to the SCV site. Zone H should intersect accessible drifts at the 310-, 365- and 410-m levels. Zones I, M and K are inferred to have in-plane dimensions roughly equivalent to the length of the SCV block (approximately 100 m). Of these nonextensive zones, only zones M and K might extend to drifts bordering the SCV block.

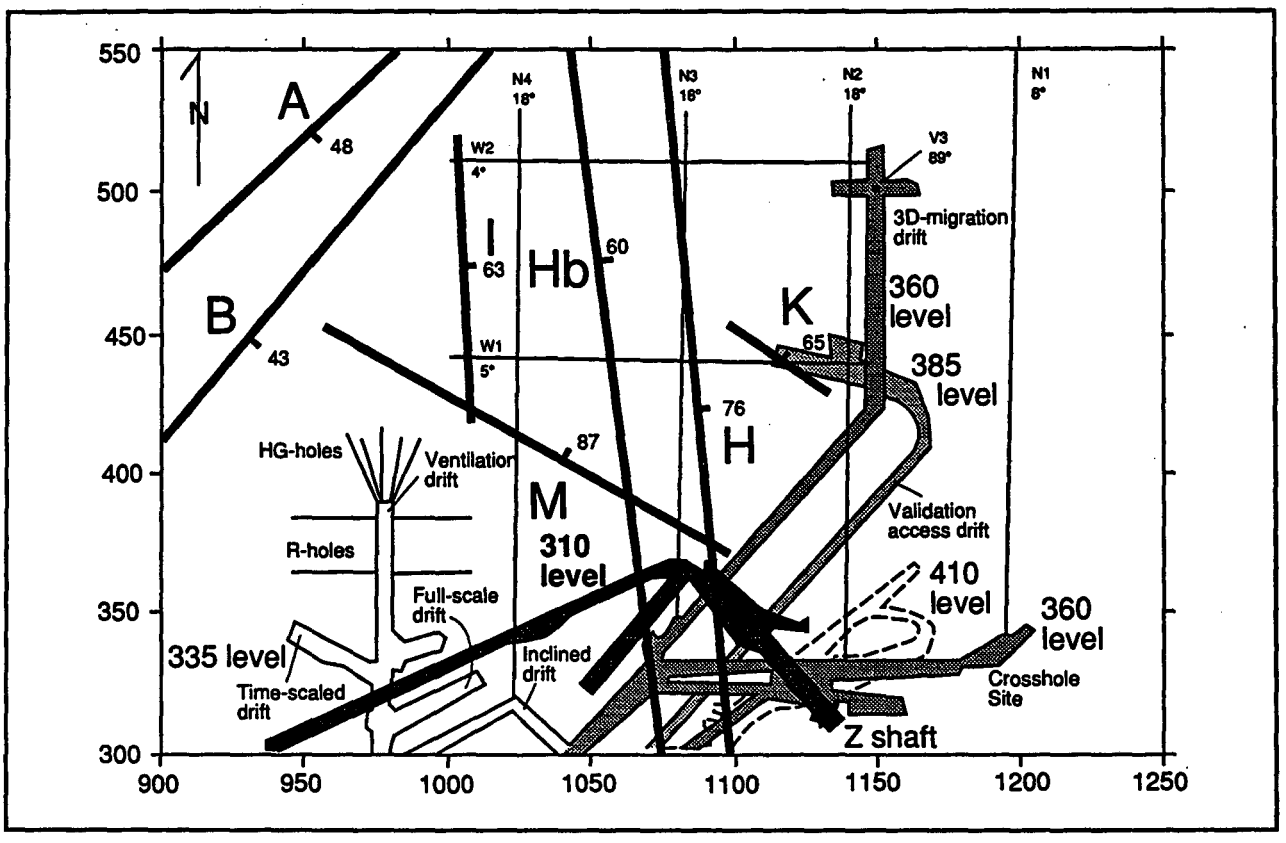

Figure 5.1. Maps showing traces of the major inferred SCV fracture zones at the 310 level.

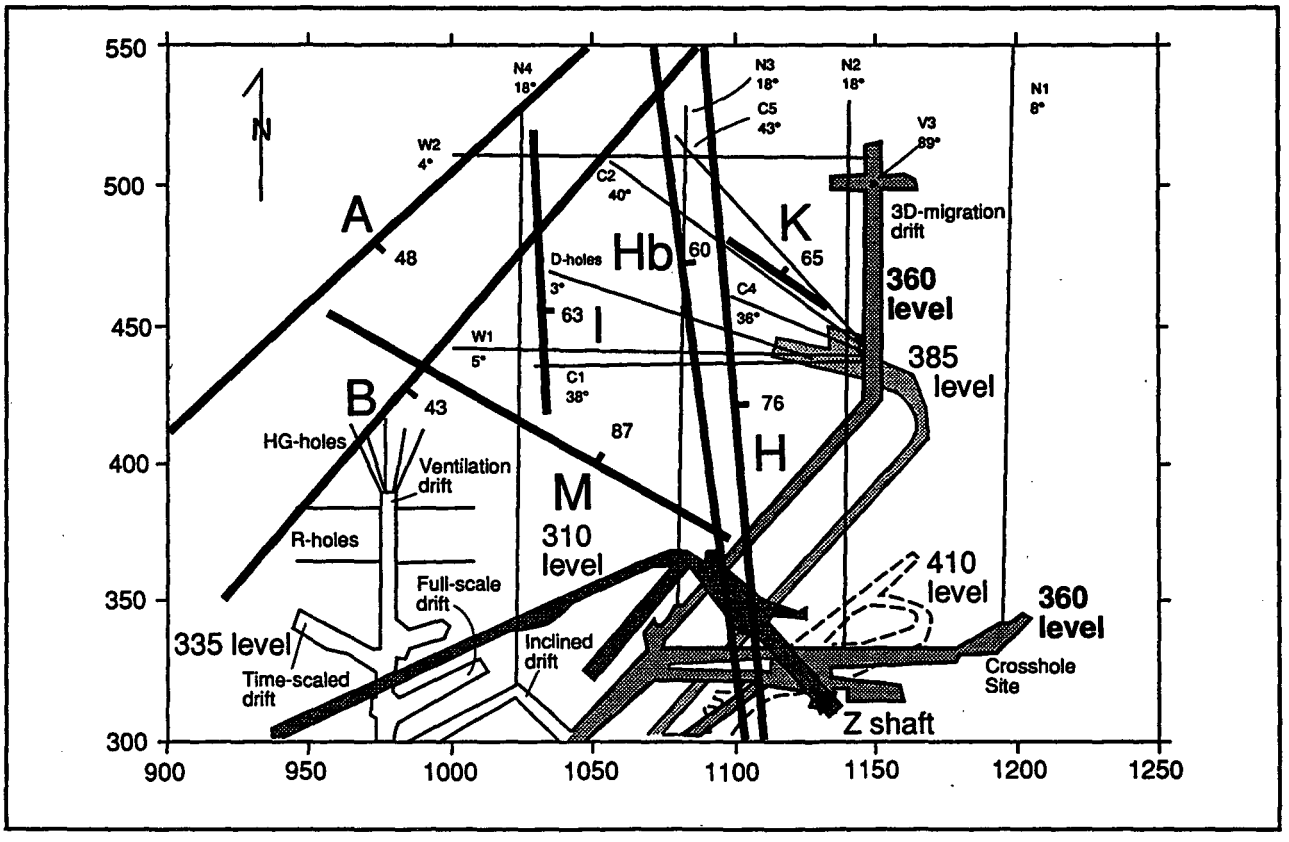

Figure 5.2. Maps showing traces of the major inferred SCV fracture zones at the 360 level.

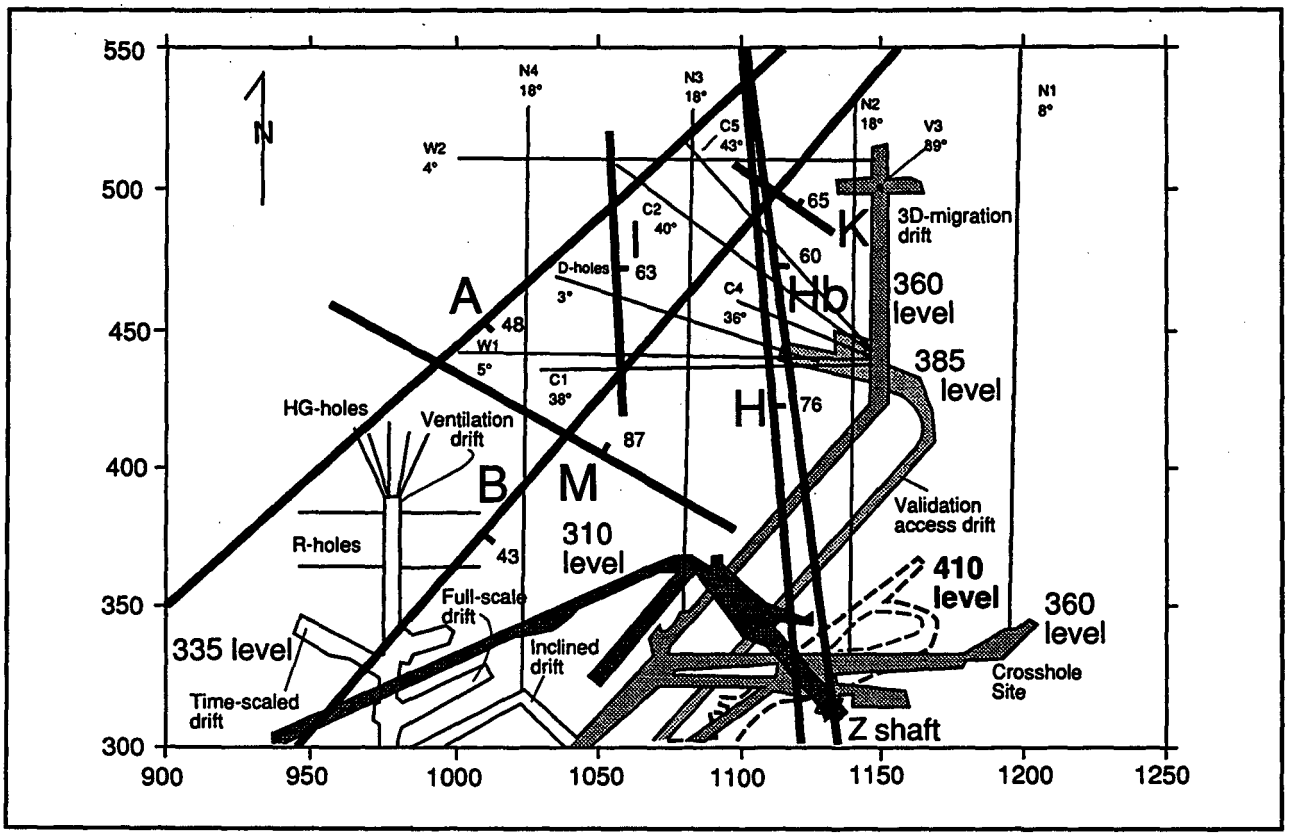

Figure 5.3. Maps showing traces of the major inferred SCV fracture zones at the 410 level.

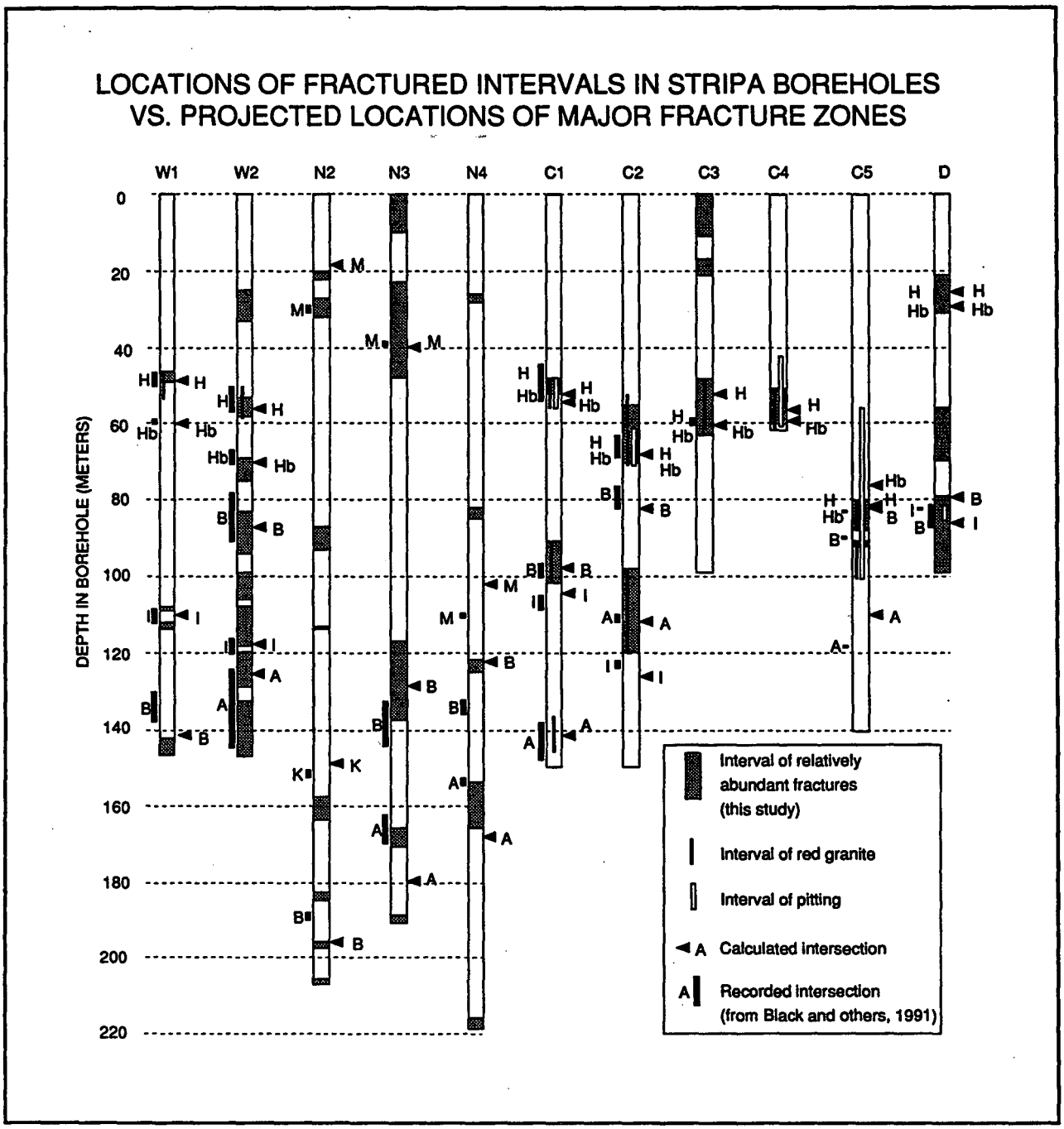

Figure 5.4. Comparison of SCV borehole core characteristics against the locations where SCV fracture zones project into the boreholes. The column labeled D is a composite from all the D holes.

Direct information on the unexposed portions of the SCV fracture zones comes from cores from the W, N, C and D boreholes. Nearly 100% of the core was recovered from these holes. The vast majority of the open fractures in the cores occur along pre-existing, sealed, chloritized joints and faults. Not all the pre-existing fractures in the cores have opened; the percentage of sealed fractures that are cracked open in the cores is actually rather small. The sealed fractures are usually no more than a few millimeters thick and typically are most closely spaced in the intervals of the core that are red. Along some of the faults mylonite and cataclasite could be identified.

Table 5.4 and Figure 5.4 show intervals of enhanced fracturing, red color and pitting that were observed by the author either in photographs of the cores or from direct inspection of several SCV cores. Sealed and open fractures were considered together in evaluating the extent of fracturing. Fractures do exist in many intervals of the core that were not considered as highly fractured. Designations here of intervals of core as being highly fractured were made on a subjective basis, and as a result, in some places the interpretations here differ from quantitative measures of fracture abundances (Fridh, 1987; Andersson, 1989; Gale and Stråhle, 1988; Black *et al.*, 1990). Still, with few exceptions, intervals considered here to have enhanced fracturing occur at or near all the places where the zones intersect the boreholes (Fig. 5.4). Intervals of enhanced natural fractures also were identified in places that are not part of recognized fracture zones, so fracturing by itself is not necessarily diagnostic of the presence of a zone; this conclusion is consistent with the quantitative data presented by Gale and Stråhle (1988) and Black *et al.* (1990). However, *all* intervals in Figure 5.4 identified as being red or as being pitted *are* near projected borehole-zone intersections. All intervals intersected by zone H are red, and pitting occurs where zone H intersects holes C1, C2, C3, and C5. In no other zone was red color or pitting as pronounced as in zone H. Interestingly, an isolated feature termed RQ which was identified by geophysical means (Olsson *et al.*, 1989) coincides with an interval of fractured, red, pitted granite encountered by the D-holes at a depth of ~85–95 m. One would expect that highly fractured, hematite-rich portions of the granite would in many places have different geophysical characteristics than sparsely fractured grey granite.

Table 5.1. Orientation and position of SCV fracture zones (from Black *et al.*, 1990).

Zone	Strike (degrees)	Dip (degrees)	Thickness (m)	Fixed Point Coordinates x	y	z
A	47°	48°	1–10 m	598	1100	360
B	40°	43°	1–10 m	567	1100	360
H	355°	76°	~20 m	450	1097	360
Hb	353°	60°	~5?	450	1085	360
I	356°	63°	1–10 m	450	1033	360
M	300°	87°	1–10 m	450	967	360
K	305°	65°	1–10 m	479	1100	360

Table 5.2. Calculated depths of intersection of SCV fracture zones with SCV boreholes. Fracture zone geometries are defined in Table 5.1.

Zone	W1	W2	N2	N3	N4	C1	C2	C3	C4	C5	D1
A	—	125.5	—	179.5	168.7	141.1	112.1	—	119.5	110.5	—
B	141.7	87.4	196.3	139.1	122.8	98.0	82.6	—	86.7	82.2	79.7
H	49.1	56.6	—	—	—	53.0	68.0	52.4	56.6	81.7	25.7
Hb	60.3	70.7	—	—	—	54.7	67.4	61.1	59.0	77.1	29.7
I	110.9	118.1	—	—	—	104.4	125.9	—	110.9	—	85.9
M	—	—	18.2	39.9	102.1	—	—	—		—	—
K	—	—	149.0	—	—	—	—	—		—	—

Table 5.3. Recorded depths of intersection of SCV fracture zones with SCV boreholes (from Black *et al.*, 1990). No intersections are recorded for borehole C4.

Zone	W1	W2	N2	N3	N4	C1	C2	C3	C4	C5	D1
A	—	124-145	—	162-170	153-155	138-148	109-112	—	*	119	—
B	130-138	78-91	188-190	133-145	122-126	96-100	76-82	—	*	90	81-89
H	46-50	50-57	—	—	—	45-54	63-69	59-61	*	84-85	23-28
Hb	59-60	67-71	—	—	—	45-54	63-69	59-61	*	84-85	23-28
I	108-112	116-121	—	—	—	105-109	122-124	—	*	—	83
M	—	—	29-31	39	111	—	—	—	*	—	—
K	—	—	151-153	—	—	—	—	—	*	—	—

Table 5.4. Characteristics of SCV borehole cores as determined by inspection by the author. Intervals of pronounced fracturing (F), red color (R), or pitting (P) are noted. Regular and bold fonts mark observations from photographs and cores, respectively. In general, drilling-induced fractures are not distinguished here.

		Distances in meters from mouth of borehole
W1	F	**45.5–49.2**, 108–109, 112–113.5, 142–145
	R	**45.5–53.5 (granite is pink)**
	P	
W2	F	25–33, **52.8–55.6**, 55.6–58, 69–75, 83–94, 99–106, 108–118, 120–129, 133–147
	R	**50.2–59 (granite is pink)**
	P	
N2	F	20–22, 27–32, 87–93, 113–114, 158.5–163.5, 183.5–184.5, 196–198, 206–207
	R	
	P	
N3	F	0–10, 23–48, 117–138, 166–171, 189–191
	R	
	P	
N4	F	**26–27.5 (drilling induced)**, 82–84.5, 122-125, 154–165, 216-220
	R	
	P	
C1	F	**47.3–51.8, 91–101.55**
	R	**47.4–56.3, 91–101.55**, 135.5-145
	P	**47.3–56.3**
C2	F	55-70, 98–120
	R	52–61.6, **62.0–71.3**, 98–120
	P	**61.6–71.3**
C3	F	17–21, **48.4–57.5**, 57.5–63
	R	**48.4–62**
	P	
C4	F	**51.4–60.0** (Core photographs not reviewed)
	R	**51.4–60.0**
	P	**42.67–61.5**

Table 5.4 (cont'd)

		Distances in meters from mouth of borehole
C5	F	**80.35–88.0, 90.85–92.35** (Core photographs not reviewed)
	R	**80.35–88.0, 90.85–92.45, 93.25–100.25**
	P	**76.65–100.25**
D1	F	21–28, 81–100
	R	21–31, **86–100 (salmon–colored)**
	P	**82.2–85.9**
D2	F	21–28, 56–66, 84–88.5
	R	20.5–30.5, **61–100 (salmon–colored)**
	P	
D3	F	23–31, 79–82
	R	21.5–31, **64–100 (salmon–colored)**
	P	
D4	F	21–31, 84–96
	R	24–30.5
	P	
D5	F	69–70, 80–96
	R	23–31.5, **80–100 (salmon–colored)**
	P	
D6	F	21.5–31.3, 58.3–66.2, 69.5–100.1
	R	20.5–31.3, **60.5–100 (salmon–colored)**
	P	**93.45–94.1**

6 OBSERVATIONS AND INTERPRETATIONS OF FRACTURE ZONES EXPOSED IN DRIFTS

Individual fractures and fracture zones in and near the SCV block were examined to define the fracture patterns within the major zones and to gain insight into how fluid might flow along the zones. A total of ten days was devoted to the subsurface observations. Six days were allocated to mapping fractures on base maps with scales of 1:1500 and 1:500. These observations provide a base for interpreting the history of fracturing. They also provide an alternative source of fracture information that can be compared with drillhole information and scanline maps of fractures on drift walls (e.g. Gale and Stråhle, 1988).

6.1 Zone H

Zone H is the most prominent SCV structure, and it might be associated with the regional areomagnetic anomaly shown in Fig. 4.5. Zone H projects through accessible drifts at the 310, 360 and 410 levels, as well as through the validation access drift. Exposures near all of the places of intersection are distinguished not so much by the style or intensity of the fracturing, but instead by the red color of the granite. The margins of the red coloration are somewhat irregular in shape at a given level, and the apparent thickness of the red exposures decreases with depth. The red color is distinctly different from the grey color typical of the Stripa granite in most of the SCV block and is considered to reflect the presence of finely disseminated hematite (Wollenberg *et al.*, 1980). Because the red color pervades zone H granite and is not confined to fracture faces or coatings on mineral grains, it may well be that hematite is pervasively distributed in microcracks along zone H. It was not possible to distinguish zone H from its companion Hb.

An average strike and dip for zone H can be estimated using three points from zone H exposures at the 310, 360 and 410 levels (Table 6.1). The plane through these points strikes N-S and dips 64° east. The local strike and dip of zone H could differ from these values by several degrees owing to the apparently irregular shape and variable thickness of the zone. The uncertainties associated with the strike and dip are estimated to be about 12° each. As defined in Table 5.1, zone H strikes N5°W and dips 76°E, and zone Hb strikes N7°W and dips 60°E. The orientation determined from the red exposures can not be distinguished from the orientations of zones H and Hb in Table 5.1 given the uncertainty in the orientation estimates and the possibility that the exposures provide information on both H and Hb. The field observations are more in keeping with zones H and Hb constituting a single zone that narrows with depth rather than H and Hb being separate and distinguishable zones of slightly different orientation.

Table 6.1. Coordinates of central points zone H exposures (as defined by red granite) at 310, 360 and 410 levels.

Level	x	y	z
310	367	1076	310
360	365	1100	360
410	332	1124	410

6.1.1 360 Level

Zone H is most extensively exposed at the 360 level where it can be observed in the 3-D access drift and the northern and southern access drifts to the crosshole site (Fig. 6.1). The borders of zone H are defined by the transition from red granite (inside the zone) to grey granite (outside the zone). The transition in most places occurs over a distance of a few meters or less. The overall strike of the zone is to the north. The width of zone H in map view varies from approximately 20 m to 45 m. Assuming a dip of 64° for the zone, its true thickness would vary from approximately 18 m to 40 m.

The borders of the zone are not sharply defined on the basis of its fracture characteristics. The zone is not delimited by fractures parallel to the zone, or by a sharp gradient in the intensity of fracturing. An inspection of the drift walls reveals no marked difference in the range of fracture orientations inside and outside the zone. Fractures show a broad range of orientations both inside and outside the zone. Many of the fractures contain a dark green (chloritic?) material that appears to be mylonitic or cataclastic.

Although fractures of numerous orientations occur within zone H, the distribution of fractures is not completely random. The longest fractures in the zone consistently strike to the north or NNW and dip steeply to the east, that is, they are subparallel to the zone as a whole. Some of these fractures can be traced for several meters from one drift to another (Fig. 6.1). There is some tendency for the longest fractures west of the zone to strike NW and the fractures east of the zone to strike NNE. Smaller fractures tend to splay off of the north-striking fractures in the zone.

Three different lines of evidence suggest that many of the fractures in zone H are faults. The most direct evidence comes from offset features. For example, in Figure 6.1, fault F7 (the easternmost labeled fault in the crosshole access drifts) displaces a 2-cm-thick quartz vein with an apparent normal separation of 180 cm. The fault strikes N43°W and dips 57°E, whereas the vein strikes N75°E and dips 65°N, so the apparent separation could be due to either right-lateral slip or normal slip on the fault. About 7 m west of this fault is another fault (F6, Fig. 6.1) that strikes NNE and dips ~45° NW. It shows an apparent reverse offset of 15–20 cm.

The second type of evidence of fault slip comes from short fractures that splay from long zone-parallel fractures (Fig. 6.2). The long fractures are interpreted as faults and the short fractures are interpreted as having opened in response to slip on the faults (e.g. Martel and Pollard, 1989). In some cases the faults will be isolated. In other cases the splay fractures are confined between a pair of parallel faults, and the splay fractures and faults together constitute part of a narrow fault zone. Faults and fault zones like these have been well documented in the Sierra Nevada of California (Segall and Pollard, 1983; Martel *et al.*, 1988; Martel, 1990). Examples of apparent fault/splay crack combinations at the 360 level are shown in Table 6.3. A normal component of dip-slip and/or right-lateral component of strike slip is indicated for all the faults in Table 6.3.

The third type of evidence for faulting is slickensided (polished) surfaces on fractures. In some cases these surfaces display striations. The striations are interpreted as being parallel to the direction of the most recent slip on the fault. As Table 6.4 reveals, the slickenline orientations collectively suggest that several distinctly different episodes of slip have occurred, for subparallel faults show different directions of slip.

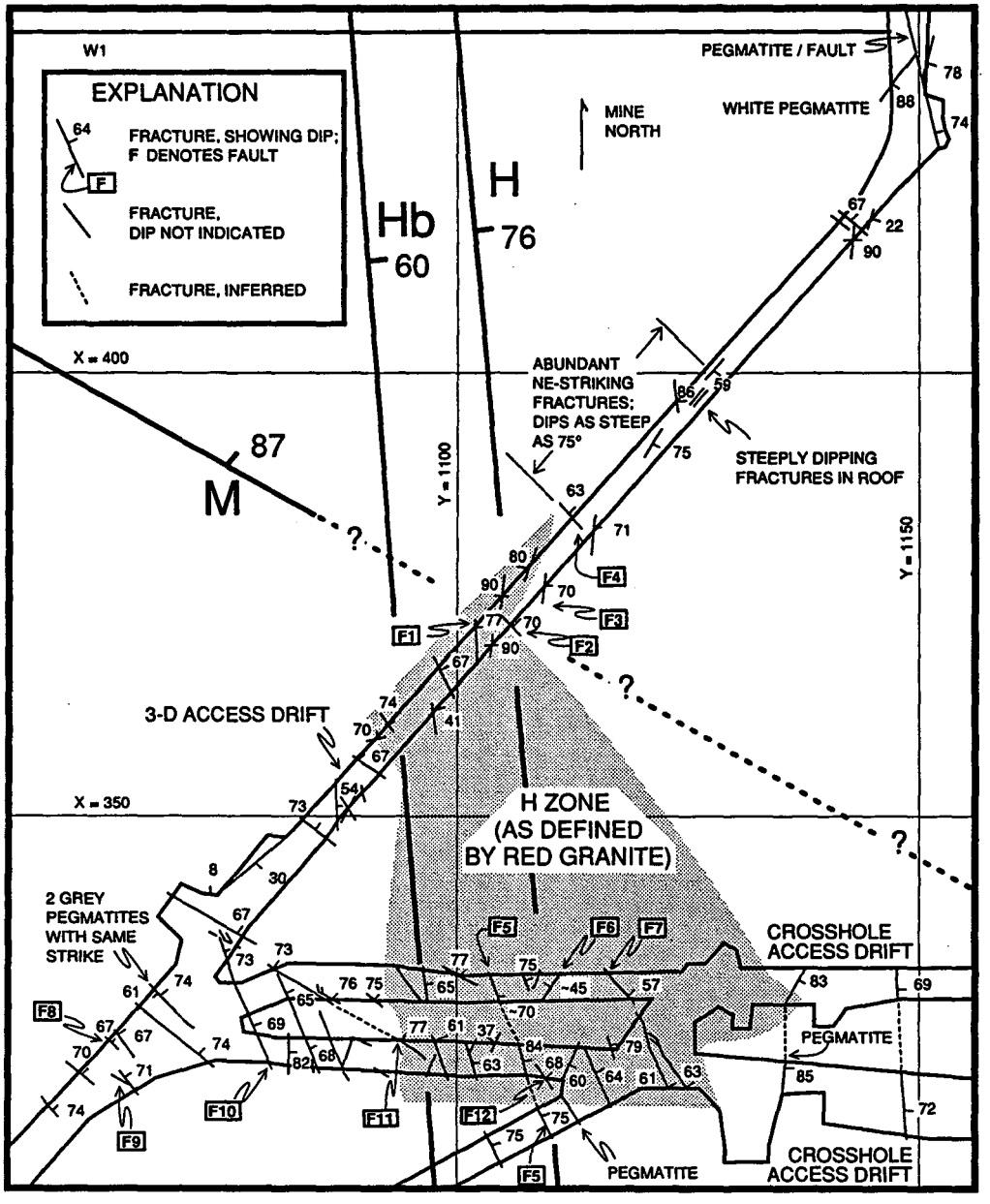

Figure 6.1. Map showing traces of major fractures within zone H at exposures at the 360 level. Faults are labeled drift by drift, with increasing numbers from left to right. The scale is given by the 50 m grid. The swath of red granite is strippled.

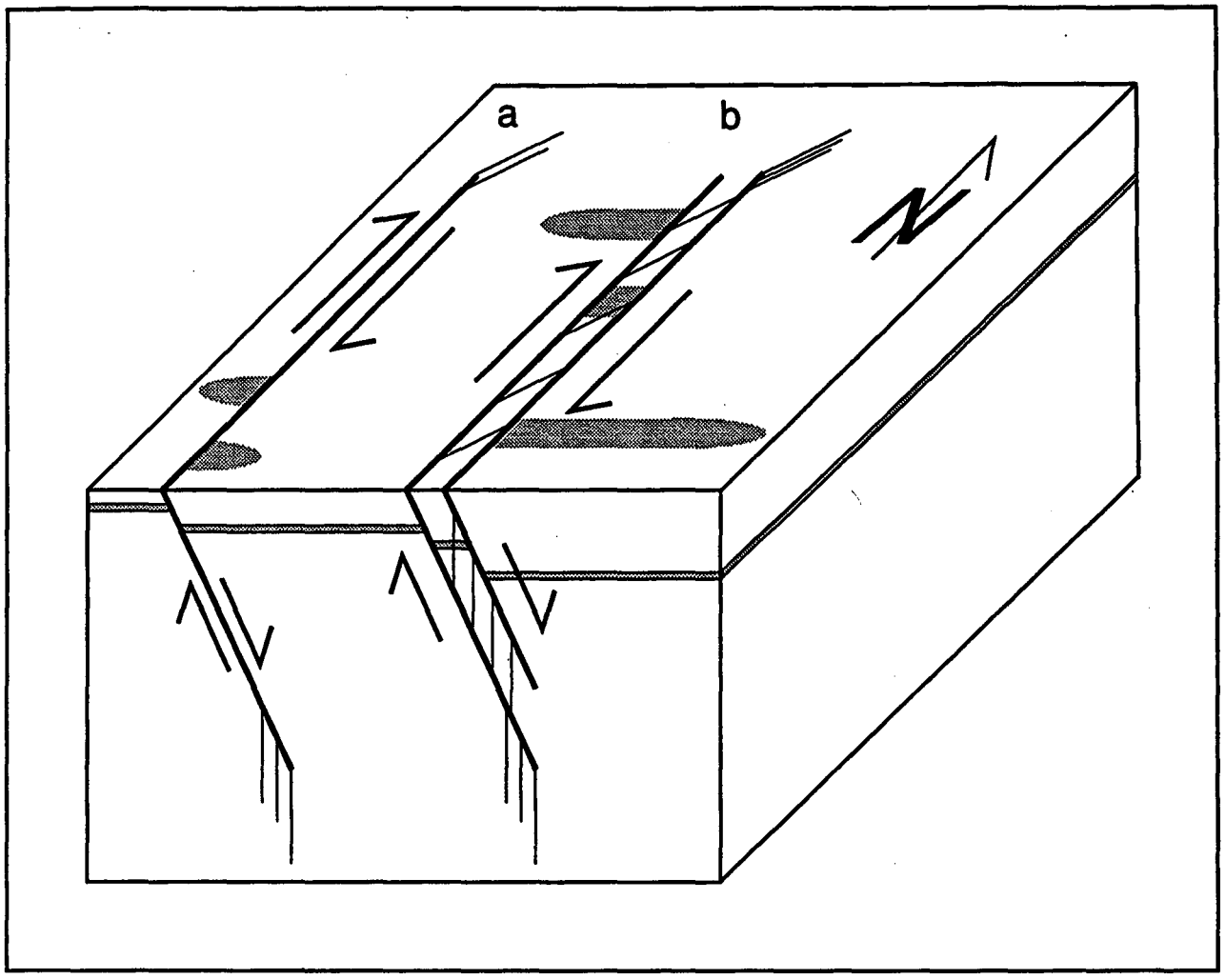

Figure 6.2. Diagram showing splay cracks along a) an isolated fault, and b) a fault zone that is bounded on both sides by faults (heavy lines). The fault zone here strikes north, dips steeply to the east, and has slipped in a right-lateral, normal oblique fashion. In map view, the traces of the splay cracks (light lines) trend ENE. In cross section view, the traces of the splay cracks are vertical.

Even some individual faults show evidence for multiple directions of slip. For example, two sets of slickenlines on calcite patches on fault F1 (see Table 6.4) suggest two different episodes of slip. The slickenlines of fault F4 plunge directly down the fault dip (see Table 6.4), indicating that the most recent slip involved pure dip slip movement. However, some splay cracks a few meters south along the fault strike nearly N-S (see Table 6.3), suggesting that at an earlier time the fault had slipped right-laterally.

Table 6.2. Evidence for faulting at 360 level based on offset markers.

Location (x, y, z)	Fault Name On Fig. 6.1	Fault strike, dip	Offset Marker strike, dip	Inferred Slip Sense
(367, 1102, 360)	F1*	N5°W, 77° E	NE, dip uncertain	Uncertain
(328, 1109, 360)	F6*	N26°E, 45° NW	uncertain	Reverse(?)
(332, 1116, 360)	F7*	N43°W, 57° E	N75°E, 65°N	Normal or reverse
(372, 1102, 360)	Not shown on map†	N22°W, ~70° E	~North, ~50° E	Right-lateral or reverse

*Denotes faults in zone H.
†Denotes faults not in zone H.

6.1.2 310 Level

Zone H is projected to intersect the 310 level near x = 365, y =1070 (Fig. 6.3). Red granite is exposed in the interval from y = 1056 to y = 1085 and may extend somewhat farther to the east (higher y-values). Assuming the zone strikes to the north and dips 64°E, the minimum thickness of the zone would be 26 m.

The nature of fracturing in the 310 level exposure resembles that at the 360 level. First, much of the fracture pattern appears chaotic and fractures of many different orientations are exposed (Fig. 6.3). Second, the longest continuous fractures strike north (or northwest) and dip steeply to the east. Third, there is clear evidence for normal faulting. A fault near y = 1059 offsets a pegmatite dike, with a normal separation of 19 cm. The observed separation is probably close to the actual displacement, because a) the fault and the dike share nearly the same strike (the fault strikes N20°E and dips 57°E, and the dike strikes approximately N10°E and dips 78°E) and b) slickenlines on the fault plunge nearly directly downdip. What appears to be a small left-lateral, normal fault zone is present near y = 1064. The fractures (faults?) that bound this small zone strike N30°W and dip 60°E, and they are linked by shorter fractures that strike N40°W and dip 78°W.

Table 6.3. Evidence for faulting at 360 level based on splay cracks.

Location (x, y, z)	Fault Name On Fig. 6.1	Fault strike, dip	Splay Crack strike, dip	Inferred Slip Sense
(372, 1102, 360)	F1*	N5°W, 77° E	N28E, 85°	Normal/ right-lateral
(371, 1106, 360)	F2*	N35°W, 70° E	uncertain, steep	Normal(?)
(375, 1109, 360)	F3†	N10°E, 70° E	N68°W, 70°N	Normal/ right-lateral
(384, 1112, 360)	F4†	N37°W, 63° NE	N-S, uncertain	Right-lateral
(331, 1103, 360)	F5*	N22°W, ~70° E	NNW?, ~75° E	Normal
(332, 1116, 360)	F7*	N43°W, 57° NE	N28°E, 79°W	Normal/ right-lateral
(326, 1060, 360)	F8†	N45°W, 67° NE	N3°W, 81°W	Normal/ right-lateral
(318, 1063, 360)	F9†	N46°W, 80° NE	N20°W, 85°W	Normal/ right-lateral
(320, 1109, 360)	F12*	N35°W, 68° NE	N35°W, 76°W	Normal
(319, 1064, 360)	Not shown on map†	N46°W, 80° NE	N10°E, 90°	Normal/ right-lateral

*Denotes faults in zone H.
†Denotes faults not in zone H.

Table 6.4. Evidence for faulting at 360 level based on slickenlines. For oblique slipsenses, N=normal, R=reverse, RL=right-lateral and LL=left-lateral.

Location (x, y, z)	Fault Name On Fig. 6.1	Fault strike, sip	Slickenline trend, plunge	Inferred Slip Sense
(372, 1102, 360)	F1*	N5°W, 77° E	N32°E, 46°	oblique: N/LL or R/RL
(372, 1102, 360)	F1*	N5°W, 77°E	S10°W, 25°	oblique: N/RL or R/LL
(384, 1112, 360)	F4†	N37°W, 63° NE	N53°E, 63°E	dip slip
(326, 1077, 360)	F10†	N25°W, 69°E	N10°E, 50°	oblique: N/RL or R/LL
(324, 1094, 360)	F11†	N64°W, 77° NE	S80°E, 50°	oblique: N/RL or R/LL
(440, 1163, 360) (location of striae)	Pegmatite/Fault† (see NE corner of Fig 6.1)	N10°W, 47°E (fault dip is variable)	N88°E, 45°	normal
(326, 1077, 360)	Not shown†	N13°W, 69°NE	northeast, moderate	oblique: N/LL or R/RL

*Denotes faults in zone H.
†Denotes faults not in zone H.

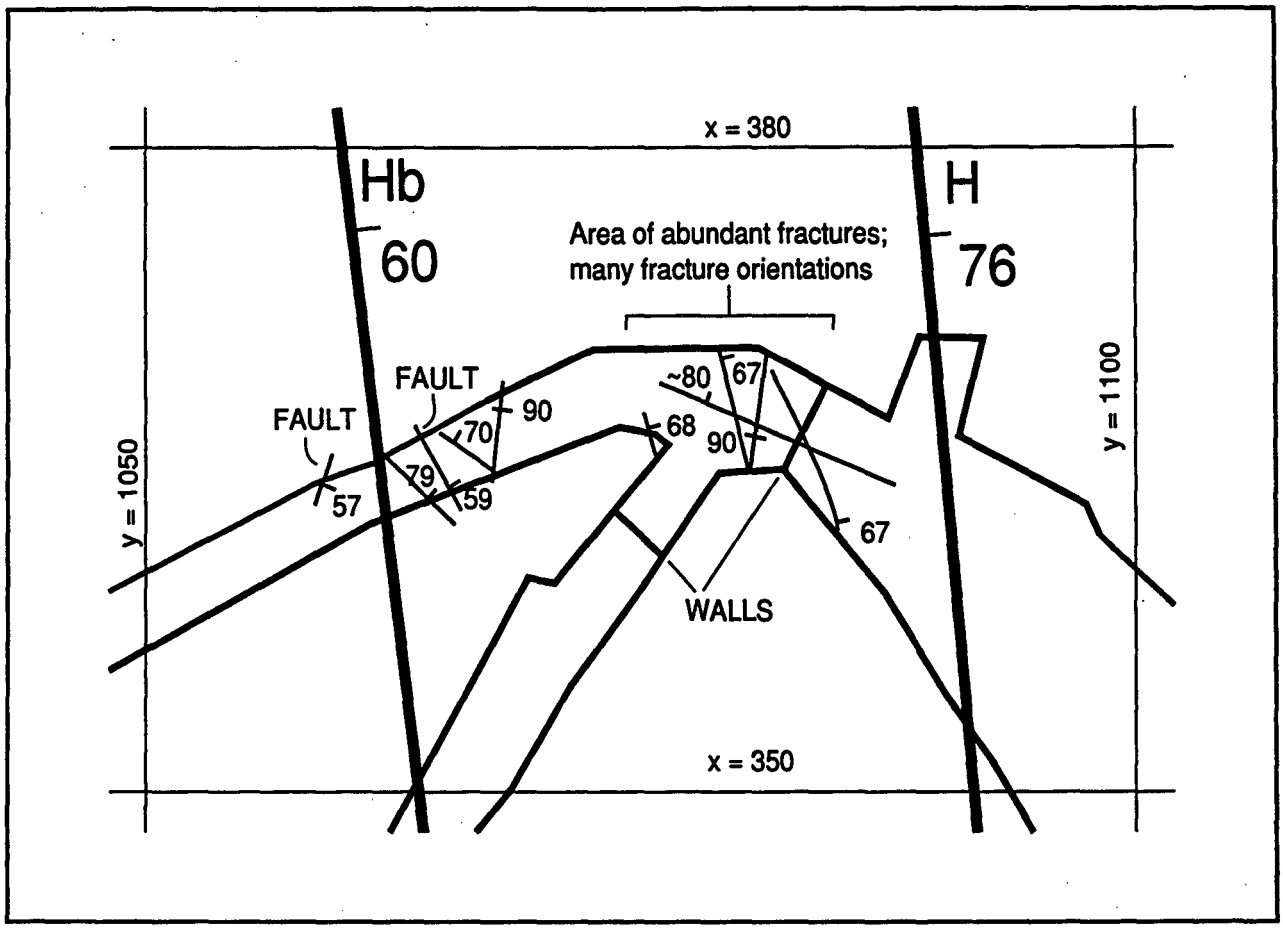

Figure 6.3. Map showing traces of the major fractures of zone H at the 310 level. The scale is given by the mine coordinate grid lines. The traces of zones H and Hb as defined in Table 5.1 are shown for the 310 level. Numbers by fractures give fracture dips.

6.1.3 410 Level

Exposures of zone H at the 410 level were sought in the drift that trends N50°E and passes immediately northwest of x = 350, y = 1150 (Fig. 6.4). This drift will be referred to as the 410A drift. The portion of the drift that was examined extends from y = 1114 to y = 1145. One zone of red granite was identified in the 410A drift, but it is much thinner than the exposures of red granite observed at the 310 and 360 levels. Starting from y = 1122 along the north wall of the 410A drift, the red granite extends northeast for only 4 m; on the south wall red granite extends over a 9-m interval.

One prominent fracture cuts through this interval of red granite. It strikes to the north and dips 72° to the east. This fracture (as will be explained below) is interpreted to be a normal fault. The fault appears to extend on-strike into the next drift to the south of the 410A drift and is thus at least 15 m long. A few bands of mylonite parallel the trace of the fault in the 410A drift. The mylonites are a few millimeters thick and occur within a meter of the trace of the fault.

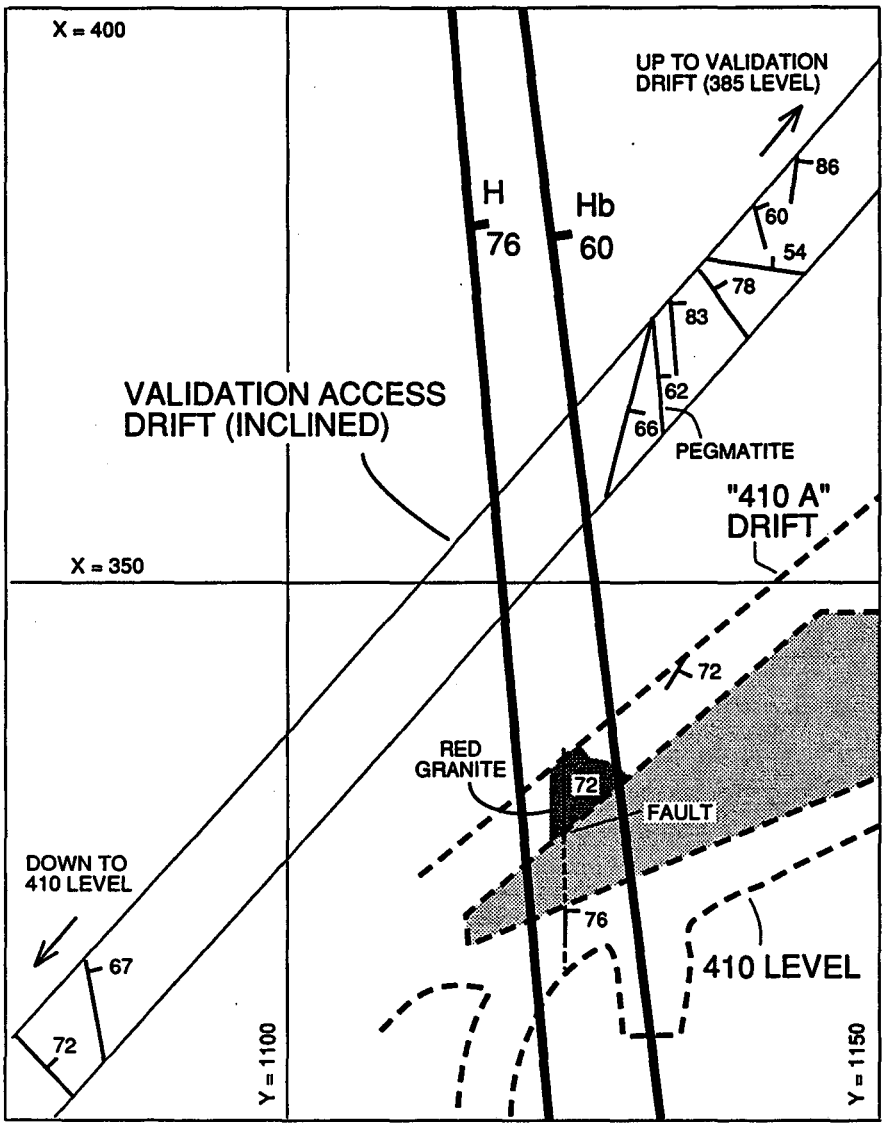

Figure 6.4. Map showing traces of the major fractures in the vicinity of zone H at the 410 level and in the validation access drift. The traces of zones H and Hb as defined in Table 5.1 are shown for the 410 level. Numbers by fractures give fracture dips.

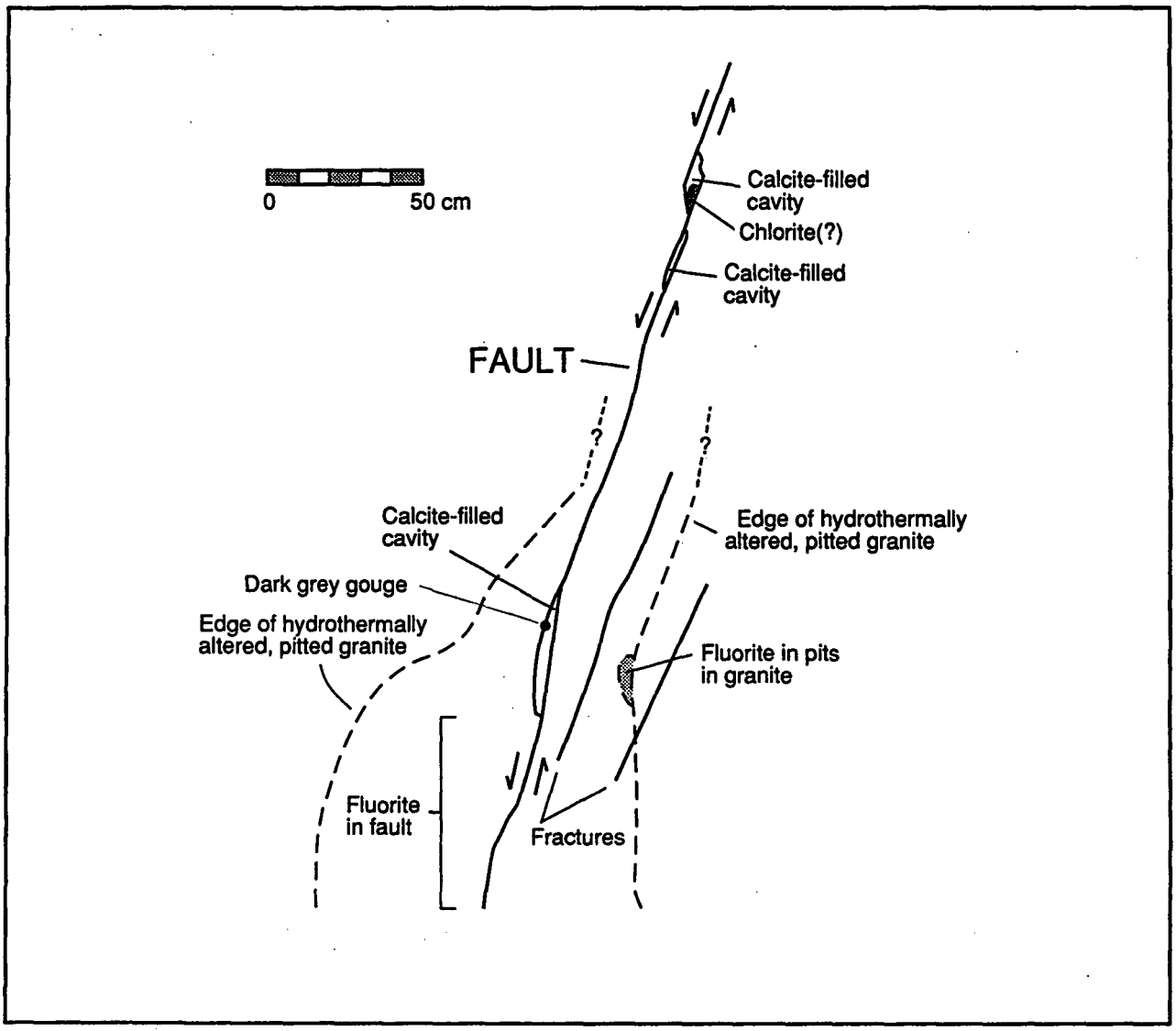

Figure 6.5. Controlled sketch showing the trace of the normal fault on the south wall of the 410A drift. View is along fault strike.

The most compelling evidence for normal slip along the fault comes from its exposure on the south wall of the 410A drift (Fig. 6.5). Three calcite-filled cavities occur between echelon strands of the fault. These cavities are interpreted as having opened as a result of normal slip on the fault strands (Fig. 6.5). A dark grey gouge occurs along the east edge of the lower calcite-filled cavity. Along the north wall of the fault a series of steeply-dipping fractures splay down off the fault and crosscut some of the adjacent mylonites. The geometric relationship of these fractures to the fault is consistent with them having formed as a result of normal slip on the fault.

Hydrothermal deposits and hydrothermal alteration provide clear evidence for fluid circulation along the fault. Fluorite has precipitated in several locations along the south wall exposure of the fault, and the granite along the fault is hydrothermally altered and pitted (Fig. 6.5). The edge of the zone of altered granite extends as much as 55 cm from the fault. Fluorite occurs in a small percentage of the pits. The 410A exposure is the only place along zone H where I observed fluorite min-

eralization along a fault and the pitting in the adjacent granite. However, pitted granite has been penetrated by several boreholes at Stripa and may have been detected in part of the SCV block by geophysical techniques (Feature RQ, Olsson *et al.*, 1989). The pitting in the cores reflects the loss of quartz (Carlsten, 1985). The 410 level observations suggest that the pitting in the SCV block may be due at least in part to the concentrated flow of reactive fluids along fractures.

6.1.4 Validation Access Drift

Only a cursory review was made of exposures in the validation access drift (Fig. 6.4). My observations were concentrated near y = 1130, approximately where zone H would project into the drift. Unlike the other drifts into which zone H projects, no red color in the granite was noticed in the validation access drift, although the lighting was poor when the observations were made. With one exception, the fractures more than a few meters long strike NNW to NNE and dip steeply to the east.

6.1.5 Conclusions Regarding Zone H

Zone H generally is defined in the drift exposures by a zone of red granite. The thickness of the zone thus defined varies from 5–40 m. The thickness of zone H appears to decrease steadily from the 310 level down to the 410 level; this would be consistent with the downward convergence of zone Hb with zone H as the 400 level is approached. Based on the drift exposures, the style and relative abundance of fractures inside the zone does not appear markedly different from that outside the zone. Within the zone, fractures of numerous orientations occur. The vast majority of the fractures are sealed with chloritic material; the fractures are old, not fresh. The longest fractures in the zone strike to the north and dip steeply to the east, subparallel to the zone as a whole. Many of the fractures in zone H are faults. Multiple senses of slip on zone H faults can be inferred, and the variety of fracture orientations observed in zone H is consistent with several episodes of slip on zone H faults. Normal faulting along north-striking faults has left a particularly pronounced imprint, and normal slip is expected to have produced steeply-dipping fractures that strike subparallel to the zone as a whole. Normal faulting may account in large part for a reported abundance of steeply-dipping, north-striking fractures in the SCV block (Long *et al.*, 1990, Figs. 2.6 and 2.7; Long *et al.*, 1991, Figs. 7 and 8).

6.2 Zone M

Zone M strikes WNW, is nearly vertical and projects to intersect the 360-level 3-D access drift very near the spot where zone H intersects the drift (Figs. 5.2 and 6.1). Given the varied orientations of zone H fractures, distinguishing fractures of zone M from those of zone H would be difficult. One might expect that zone M would contain numerous fractures that strike northwest, but fractures of that orientation are scarce where zone M projects into the 3-D access drift (Fig. 6.1). Northwest-striking fractures *are* numerous in the drift exposures west of zone H, but these fractures do not appear to extend on strike SE across zone H. Although there is no strong evidence at the 360 level for a northwest-striking fracture zone cutting zone H at X = 375 (Fig. 6.1), one might extend into zone H from the northwest and terminate against it at X = 325.

6.3 Zone K

Zone K strikes N60°W and dips 65° to the northeast. It projects to intersect the 3-D migration drift at the 360 level (Fig. 5.2) and fractures there have been mapped in detail (Abelin and Birgersson, 1987). There is no evidence of a prominent fracture zone that strikes WNW where zone K would intersect the drift (Fig. 6.6). Several fractures that strike WNW are exposed on the drift roof several meters north of the projected intersection. However, these fractures dip shallowly to the southeast, not steeply to the northeast as zone K is supposed to, and none are shown as cutting completely through the drift. The mapping suggests that zone K does not extend to the 3-D migration drift.

6.4 Evidence for Multiple Generations of Fractures

A variety of observations, both of the drift walls and of borehole cores, indicate that the Stripa fracture zones are ancient structures that have been reactivated repeatedly. First, the pervasive red color along zone H points to an early episode of pervasive fracturing, fluid flow, hematite precipitation, and fracture healing along the zone. Munier and Tirén (1989) have likewise attributed reddening of the granite in the Finnsjön coastal area NNE of Stockholm to the effects of fluid flow along fractures. Much of the transgranular fracturing along zone H must post-date the precipitation of the hematite. Second, several episodes of slip are indicated in light of evidence for both normal and reverse dip-slip and both left- and right-lateral strike-slip on subparallel faults. Third, the materials in the fractures indicate repeated episodes of fluid flow and faulting. At least two distinct sets of minerals (in addition to the hematite) have precipitated from water circulating along the fractures. The mylonitic and cataclastic materials in the faults suggest that episodes of faulting occurred under different pressure/temperature conditions. Although the apparent lack of foliation has been taken as evidence for a lack of plastic deformation in the granite, the evidence cited above indicates that the granite has a long and complicated history of faulting, fracturing, and fluid flow. Multiple episodes of deformation are also consistent with the tectonic history of central Sweden since the emplacement of the Stripa granite.

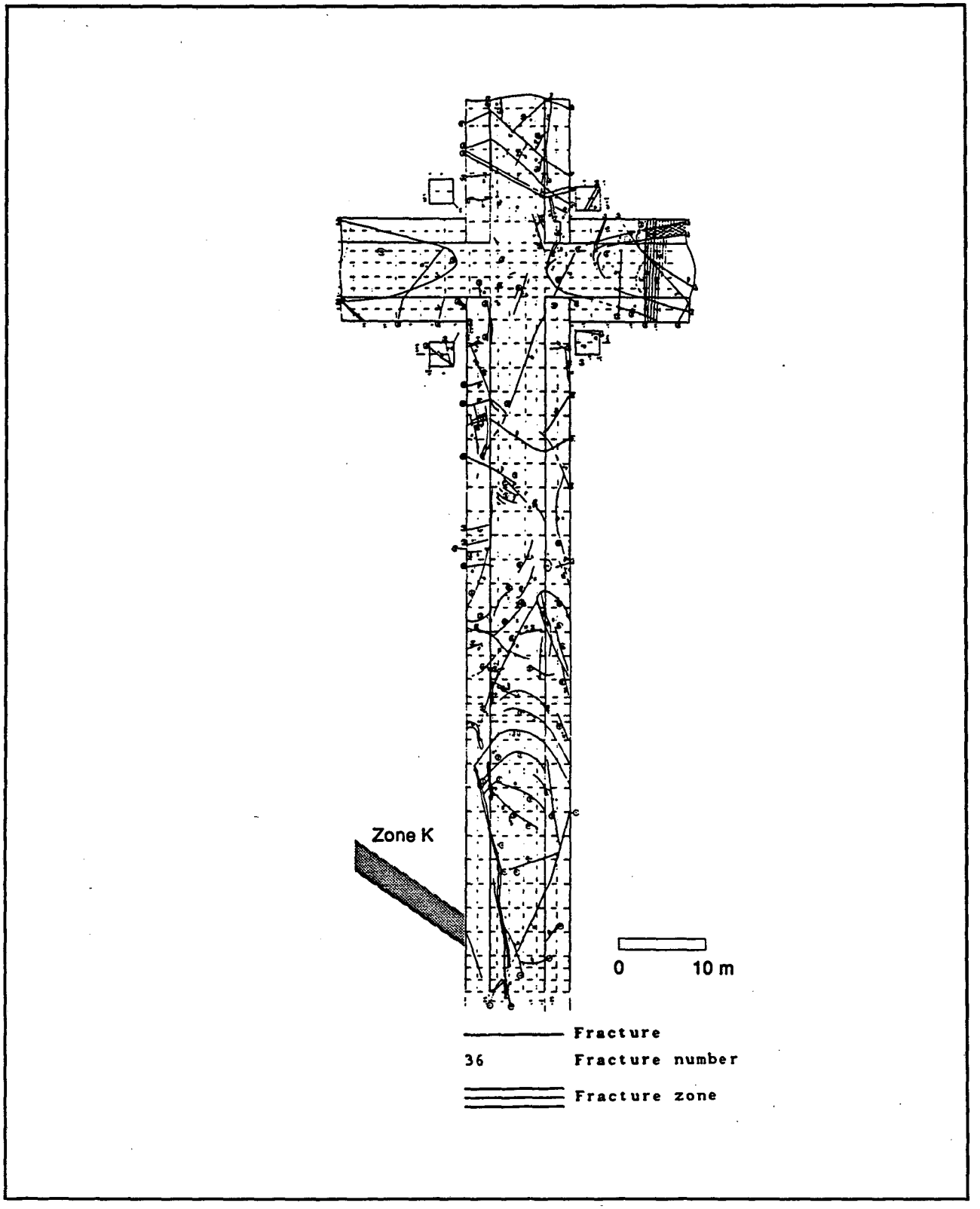

Figure 6.6. Map showing traces of fractures identified in the walls (side panels) and ceiling (central panels) of the 3-D migration drift (360-level) and the projected intersection of zone K with the drift. Mine north is to the top of the page (modified from Abelin and Birgersson, 1987).

6.5 Porosity due to Alteration of the Granite

Although most of the flow at Stripa is inferred to occur through fractures, some flow might occur through regions where porosity exists due to dissolution of quartz (Carlsten, 1985). Pitted granite has been reported in several cores recovered from boreholes at the Crosshole Site at the east end of the crosshole access drifts (Carlsten, 1985). Pitting apparently occupies a large enough volume in part of the SCV block that it can be identified on geophysical tomograms (feature RQ; Olsson *et al.*, 1989). As shown in Table 5.4, pitting can be observed in cores from boreholes C1 (47.3–56.3 m), C2 (61.6–71.3 m), C4 (42.67–61.5 m) and C5 (76.65–100.25). In these intervals the holes penetrate zone H. These portions of the cores are also pink or red and contain many healed fractures (these include potential bands of mylonite and cataclasite). Pitting of granite was also noticed adjacent to the normal fault in the 410A drift (Fig. 6.5). Pitting was not observed in the portions of these cores well removed from zone H. The pitting seems to be localized near fractures and hence may contribute to "fracture flow" through the granite.

6.6 Comparison with scanline information

Scanline maps of driftwall fractures were prepared along the 3-D access drift (Gale and Stråhle, 1988) and the ventilation access drift (Gale *et al.*, 1990). These maps were prepared as 2-m-tall strip maps along selected portions of selected drift walls. Fractures were documented through a combination of photographs and driftwall measurements. The function of the scanlines was to provide a data base allowing a statistical characterization of fracture orientations, trace lengths, and spacing. The scanlines provide information on fractures with trace lengths as small as 0.5 m in order to represent a statistically large number of fractures. In contrast, information for this report was collected so that the structure and evolution of the fracture systems could be interpreted; for that reason the larger fractures were targeted. This section does not compare the outcomes or objectives of the two approaches, but rather highlights some differences in the styles of data collection prompted by the different approaches.

The level of detail used in preparing the scanline database was in general considerably finer than what was used in the preparation of this report, so one might expect that all the fractures shown on the maps of this report would be readily identifiable in the corresponding scanline data tables. This is not the case. First, scanline information was collected on one wall of a drift (Figure 6.7), whereas the information presented on the maps herein was collected from both walls and the drift roof. Some fractures with traces that are prominent or structurally significant appear on one wall but do not extend to the other. Second, the locations of fractures in the scanline data base reflect where a fracture would intersect the scanline, which was ~1.5 meters above the drift floor. The maps of this report show the traces of the fractures as they would appear at the level of the drift floor. Some fractures in the scanline database have apparently different locations than shown on the maps of this report because of this. Third, some splay cracks which were used to estimate the direction of fault slip have trace lengths less than 0.5 m, and these would not be part of the scanline data base. Fourth, some splay cracks are very difficult to detect on scanline photographs, and others occur just outside the edges of the scanline maps. Fifth, some features on the map be slightly mislocated. However, even if scanline data and mapping information were collected in a perfectly accurate manner, the two data sets could be somewhat difficult to compare unless they were collected in a carefully coordinated manner. Just as the mapping presented here cannot substitute for the scanline data as a statistical database, the scanline data is not a complete substitute for geologic mapping.

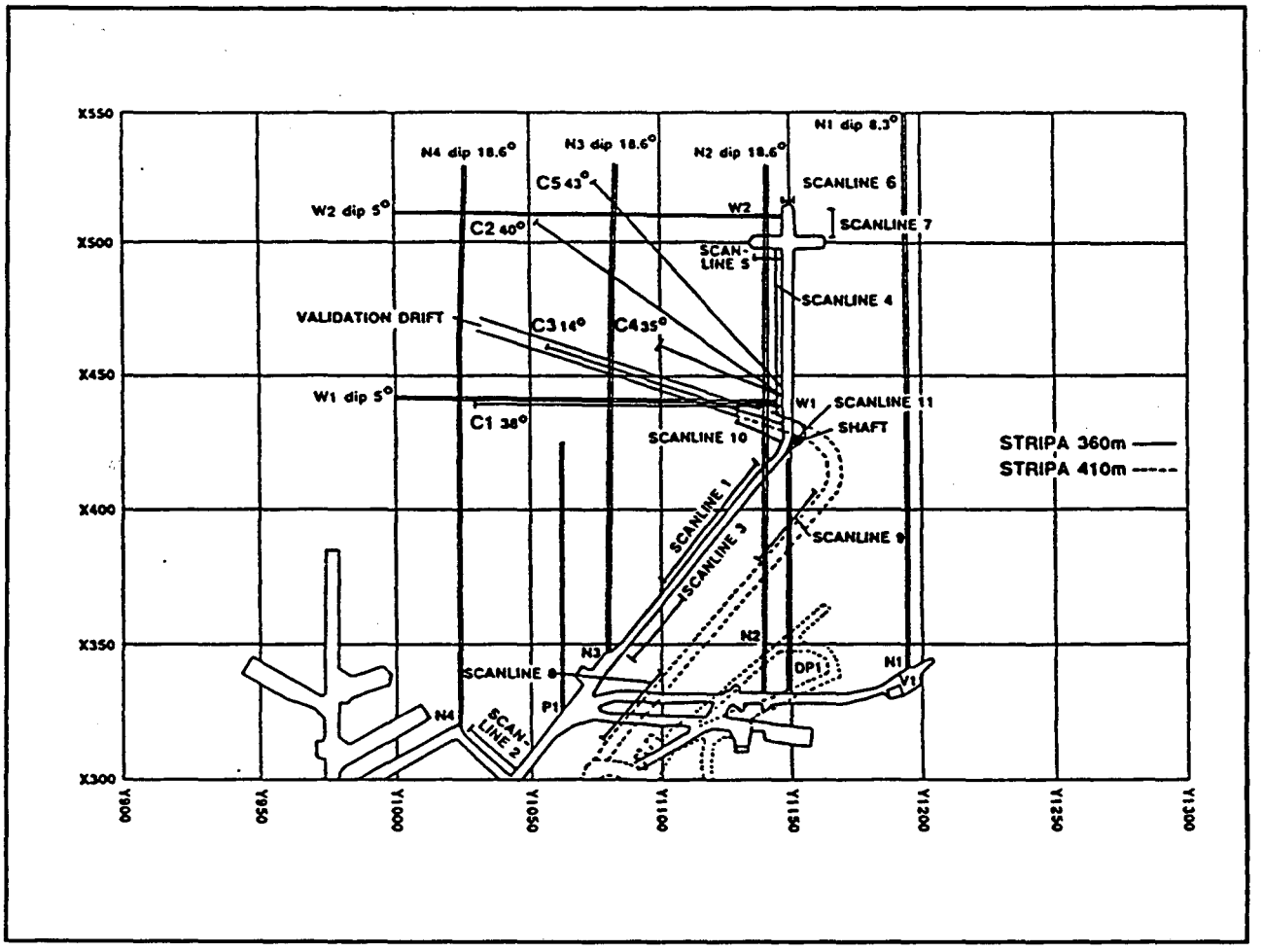

Figure 6.7. Location of scanlines at the Stripa mine. From Gale *et al.* (1990).

6.7 Comparison of geophysical model with drift-wall observations

Of the seven fracture zones (A, B, H, Hb, I, M and K) inferred within the SCV site based on remote sensing techniques, the drift-wall exposures provide evidence for only zone H and/or zone Hb. These two zones could not be identified separately. The geophysically-based model does not require that the other zones intersect the drifts, and no evidence was found to indicate the five other zones extend to intersect the drifts. The seven-zone model and the drift-wall exposures are consistent with each other, but other fracture zone models could also be consistent with the driftwall observations. Given the evidence for multiple episodes of fracturing and faulting, fractures of many orientations are likely to be present in all the fracture zones.

7 BOREHOLE FRACTURE ORIENTATION DATA

In this section the driftwall observations of SCV fractures are compared with fracture orientation data on the SCV block as a whole obtained from boreholes. The two most important points pertaining to the observed geometries of zone H fractures in the drift walls are (1) the multitude of fracture orientations, and (2) the tendency for the longest fractures to parallel the zone (i.e. strike to the north and dip steeply to the east). The results here will also be compared to those obtained by Gale and his co-workers using cluster analyses of borehole and scanline data. Gale and Stråhle (1988) concluded 1) that fractures could be grouped into three major clusters (one steeply-dipping set that strikes N-S, another that strikes NW, and a subhorizontal set), and 2) that "the north-south striking fracture set has a much higher density than the other sets or clusters." Gale *et al.* (1990) analyzed a larger data set and concluded that the fractures could be interpreted as falling into one large cluster (N-S strike), one intermediate-size cluster (WNW-strike), and ten small clusters.

Gale and his co-workers noted that the censoring effect of borehole bias is a critical factor to account for in analyzing the borehole orientation data. In this section the concept of borehole bias is introduced. The distributions of fractures actually encountered in several SCV boreholes is then compared to some synthetic distributions obtained by sampling a uniform random distribution of imaginary fractures with imaginary boreholes.

7.1 Introduction to Borehole Bias

Boreholes have a higher probability of intersecting (i.e. sampling) a fracture the more nearly perpendicular to the hole the fracture is (Terzaghi, 1965); this effect is referred to here as borehole bias . This effect can be quantified, because the reciprocal of the spacing between fractures can be thought of as a linear density or, alternatively, as a measure of the probability of intersecting a fracture of a given orientation. For a set of uniformly spaced, uniformly distributed, identically-shaped planar fractures, the distance between fractures along a given line scales as $1/\cos\theta$, where θ is the angle between the line and the normal to the fracture plane (Fig. 7.1). For a set of uniformly spaced, uniformly distributed, identically-shaped planar fractures, the *relative linear density* (or *relative probability* of fracture intersection) is defined here as $\cos\theta$. The relative probability thus measures the linear density of a set along a given line relative to its linear density along a perpendicular line, and it gives a measure of borehole bias potential. Figure 7.1 illustrates that the relative probability of intersecting a fracture is 50% over a given distance along a borehole for a set of infinite fractures where $\theta = 60°$. Changing the spacing between fractures or the size of fractures would change the absolute probability of intersecting fractures of a given orientation but would not change the relative probability of intersecting them.

To explore the effect of borehole bias, some synthetic cases will be presented. In these cases the imaginary rock mass under consideration contains fractures of identical size and shape, with the orientation of the fractures being uniform and random. The term "uniform" means that the poles to the fractures would have a uniform density if projected onto an enclosing sphere or onto an equal area diagram (Fig. 7.2a). A uniform distribution sampled at random is quite different from a distribution formed by combining randomly selected fracture strikes and randomly selected fracture dips (Fig. 7.2b). In the latter distribution there is an over-abundance of subhorizontal fractures; their poles cluster near the center of an equal area plot.

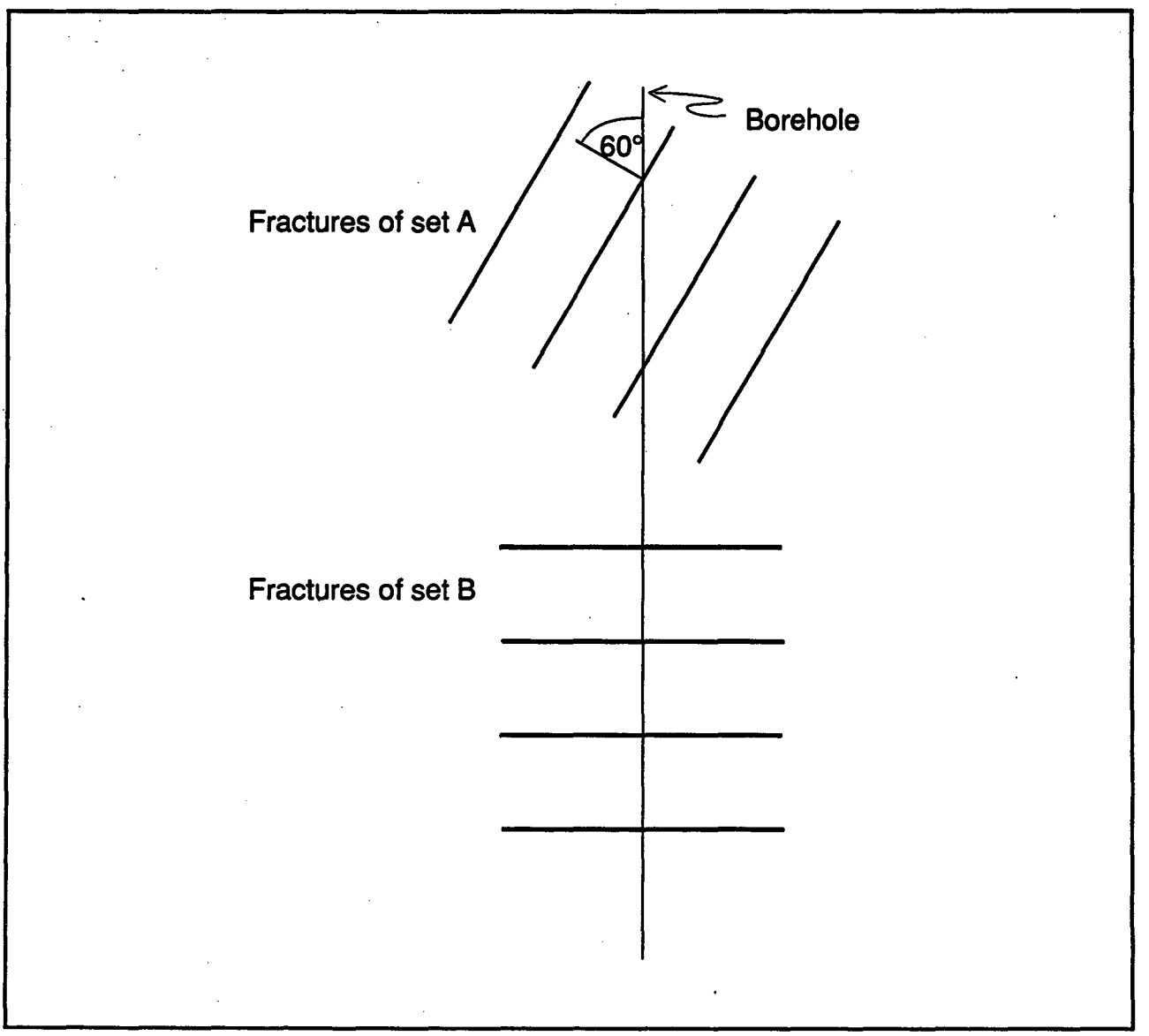

Figure 7.1. Relative probability of a borehole intersecting a fracture. For fractures of set A, $\theta = 60°$, and the relative probability of intersecting a fracture is 0.5. For fractures of set B, $\theta = 90°$, and the relative probability of intersecting a fracture is 1.0. Over a given distance along the borehole, twice as many fractures of set B are intersected as from set A.

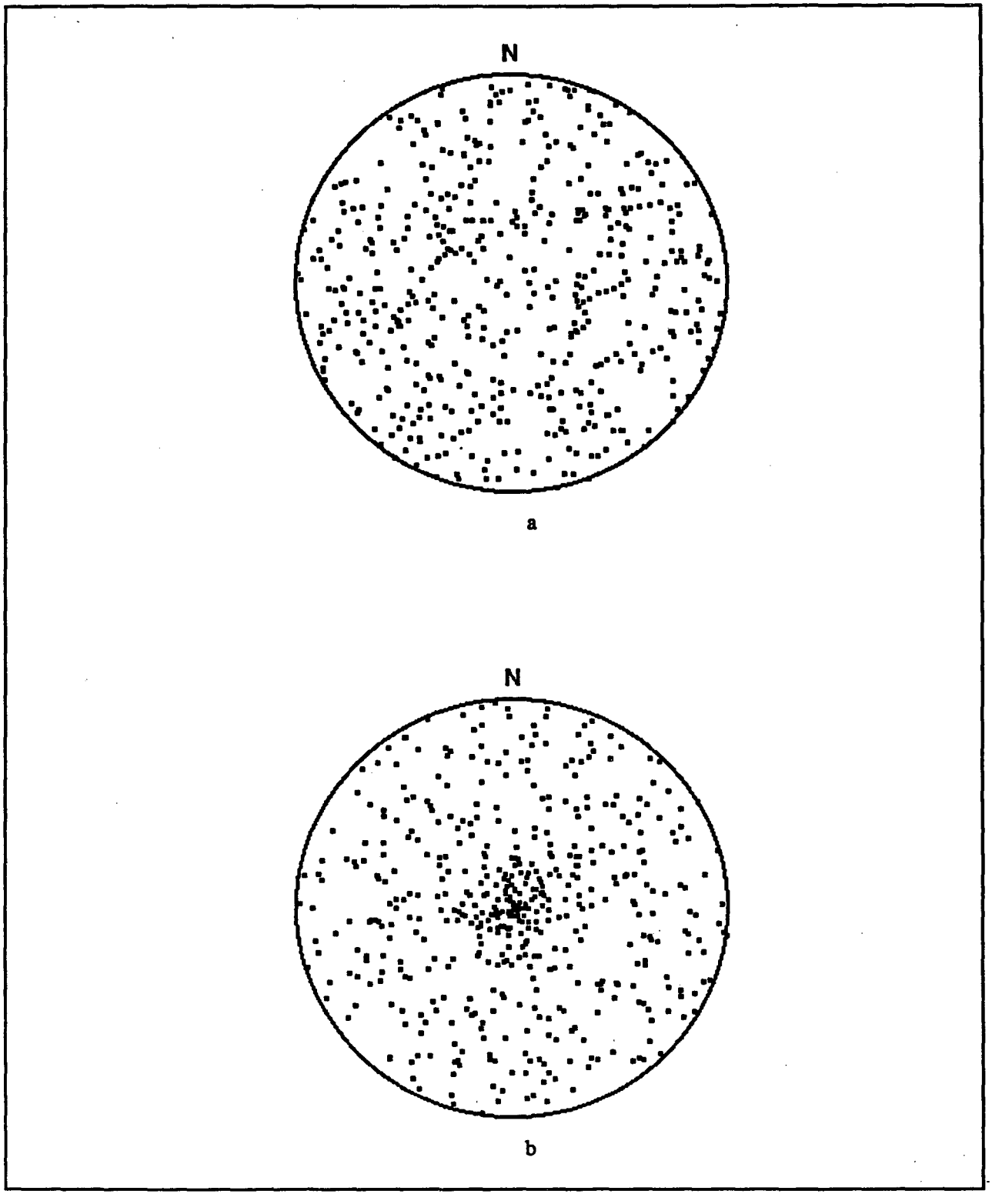

Figure 7.2. Equal area lower hemisphere plots of synthetic distributions of 500 fracture poles from a) a uniform distribution sampled at random and b) a distribution prepared from combinations of fracture strikes and fracture dips selected at random. Note the concentration of poles to subhorizontal fractures in b.

Now suppose an imaginary hole is bored through the imaginary rock mass. The radius of the hole is considered to be tiny relative to the in-plane dimensions of the fractures. The relative probability of intersecting a fracture is taken as cos θ. In the case of a vertical borehole, θ would also be the dip of the fracture, and the strike of the fracture would not affect the probability of intersection. A fracture will be considered as being intersected by the borehole if $N \leq \cos \theta$, where N is a number selected at random between 0 and 1. The fractures nearly perpendicular to the borehole will be over-represented in the borehole sample (Fig. 7.3). If the hole is vertical, subhorizontal fractures will be over-represented in the borehole records (Fig. 7.3a). If a hole trends E-W, steeply-dipping fractures that strike N-S will be over-represented (Fig. 7.3b). For inclined holes the poles have skewed distributions on equal area plots (Fig. 7.3c, d). Three points emerge. First, clustering of fracture poles about the orientation of the borehole is a sign of borehole bias. Second, the magnitude of the borehole bias effect can be so pronounced that a cursory review of borehole fracture orientation data could lead to a grossly incorrect estimate of the *in situ* fracture orientation distribution. Third, the orientation of a borehole must be accounted for in an analysis of the fracture orientation distribution revealed by a borehole survey. The same *in situ* distribution of fractures can yield markedly different samples if investigated by boreholes of different orientation. The difficulty of interpreting borehole fracture orientation data can be compounded if the fractures are not perfectly planar (i.e. the fracture orientation changes as a function of position) and the *in situ* distribution of fractures is nonuniform in space, situations that are not uncommon (Segall and Pollard, 1983; Martel *et al.*, 1988; Martel and Peterson, 1990).

7.2 Interpretation and Discussion of SCV Borehole Data in Light of Borehole Bias

In order to test whether the fracture orientations recorded from SCV boreholes were compatible with a model based on the driftwall observations, a series of comparisons were made. The recorded fracture orientation distribution for each borehole was compared to a uniform random synthetic distribution (of the type described above). If the synthetic distributions match the recorded distributions well, then the recorded orientation distribution would be consistent with a uniform random *in situ* fracture orientation distribution. If the synthetic and recorded distributions are similar except that fractures of a certain orientation are more concentrated in the recorded distribution than the synthetic distribution, then the recorded orientation distribution would be consistent with an *in situ* distribution that had a significant random component but also contained a certain set of fractures that was longer and/or more numerous than fractures of other orientation. The number of fractures in each synthetic plot was selected to match the number of fractures in the corresponding recorded distribution so as not to introduce a bias there.

Recorded distributions (courtesy of John Gale and his co-workers) and synthetic distributions are compared in Figures 7.4, 7.5, 7.6, and 7.7. An inspection of these figures reveals three key points. First, there is a strong clustering of fracture poles in the direction of the borehole. Second, the boreholes individually and collectively detect a range of fracture orientations. Third, the patterns of the recorded and synthetic distributions are similar at a gross level for nearly all of the boreholes, but most of the recorded and synthetic distributions show distinct differences in detail. These observations collectively suggest that fractures in the SCV block are oriented in a largely chaotic manner, with the recorded distributions being strongly influenced by borehole bias. However, there also appears to be a distinct heterogeneity in the fracture-orientation distribution within the SCV block. The recorded distributions show different degrees of clustering about the orientation of a borehole (relative to the corresponding synthetic distribution) depending on the orientation and location of a borehole. For the W holes (Fig. 7.4) and the D holes (Fig. 7.7) the poles are more

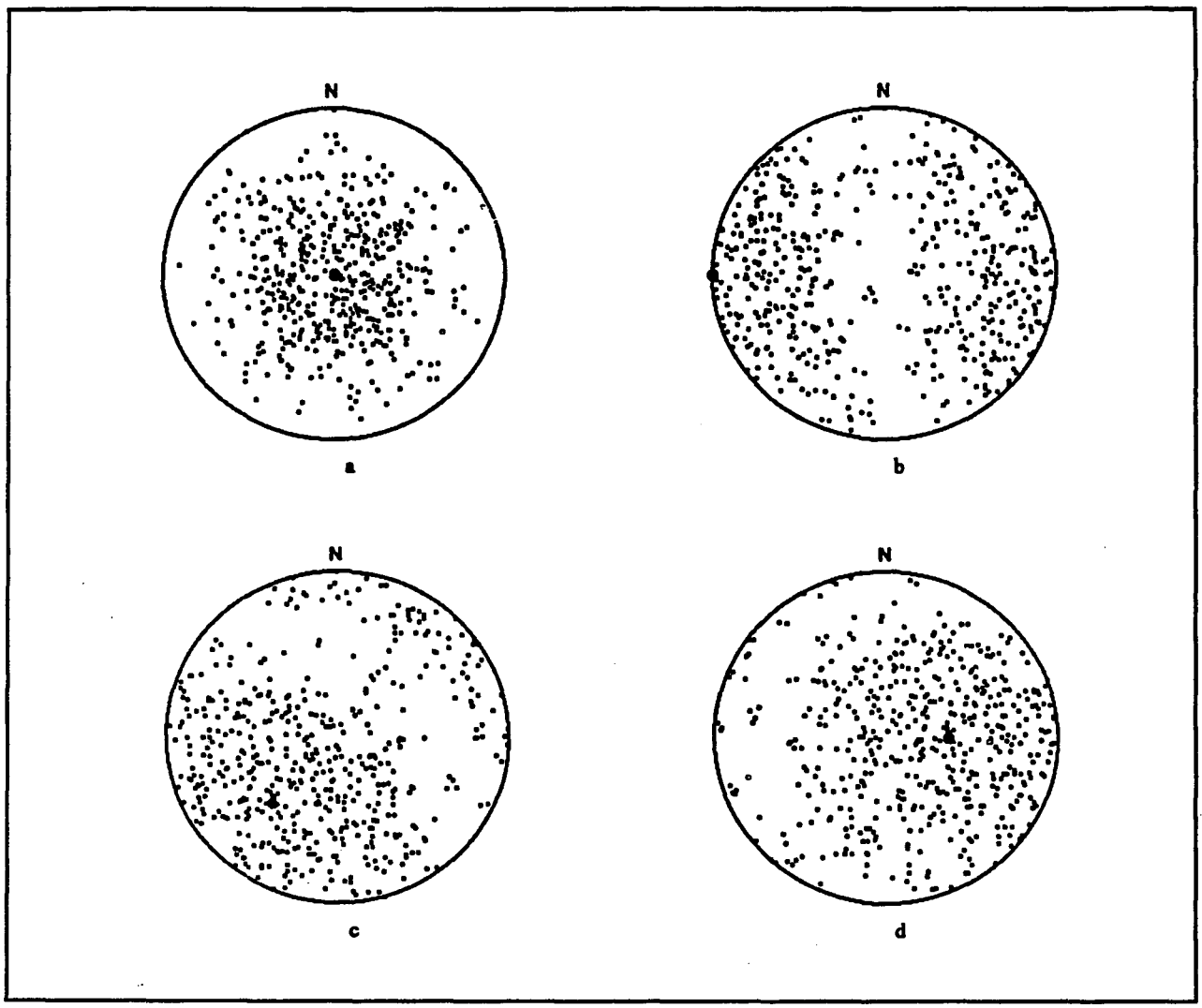

Figure 7.3. Comparison of synthetic distributions of 500 fracture poles selected from a uniform fracture distribution sampled along boreholes of four orientations. Plots are equal area lower hemisphere projections. Borehole orientations are marked by large dots. Note the clustering of fracture poles about the borehole orientations. a) Vertical borehole. b) Borehole trends west and is horizontal. c) Borehole trends southwest and plunges 45°. d) Borehole trends east and plunges 60°.

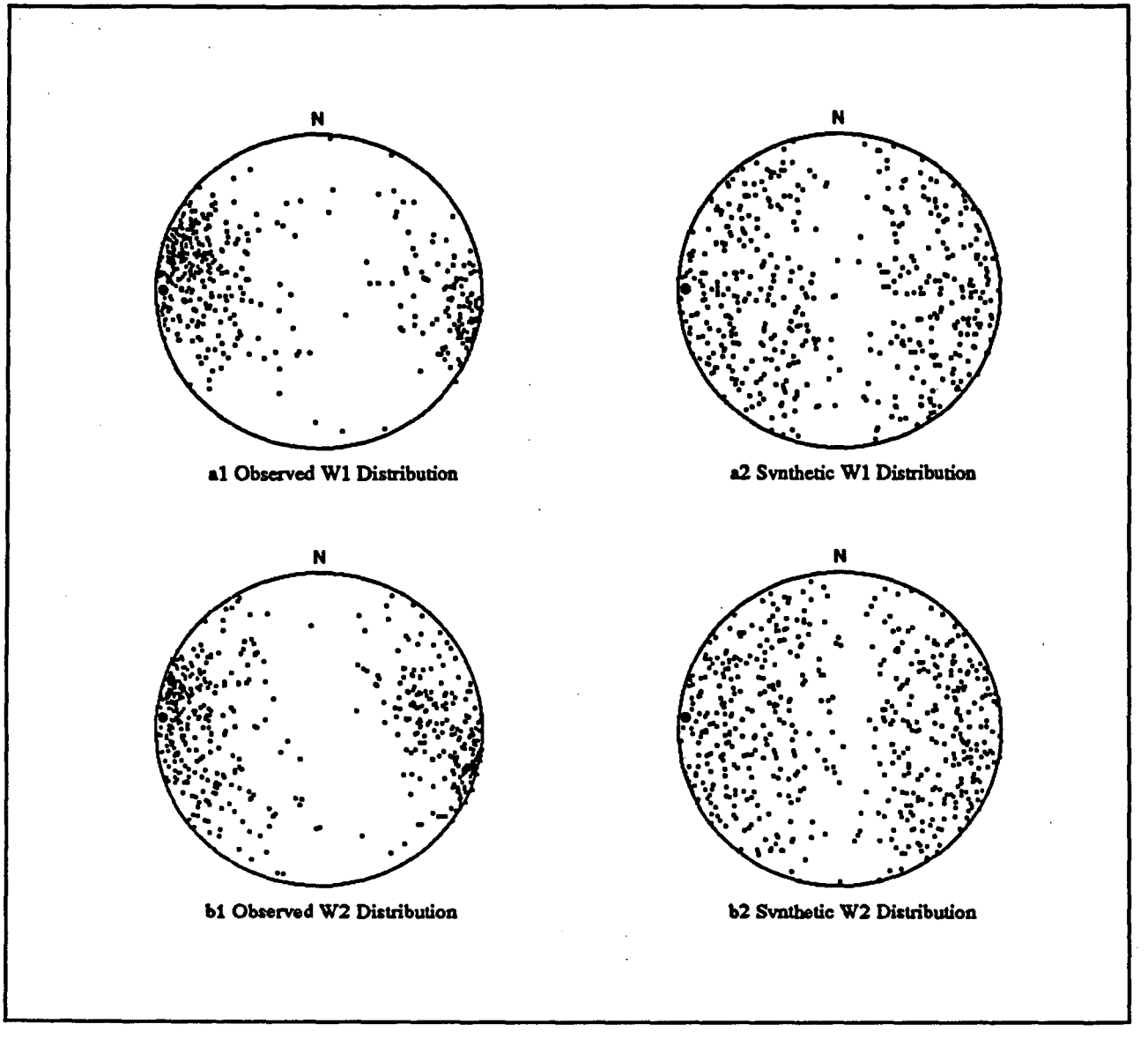

Figure 7.4. Comparison of recorded (left) and synthetic (right) fracture orientation distributions for boreholes a) W1 and b) W2. Orientations of boreholes are marked by large dots. Data points touching the borehole orientation dots have been removed for the sake of clarity.

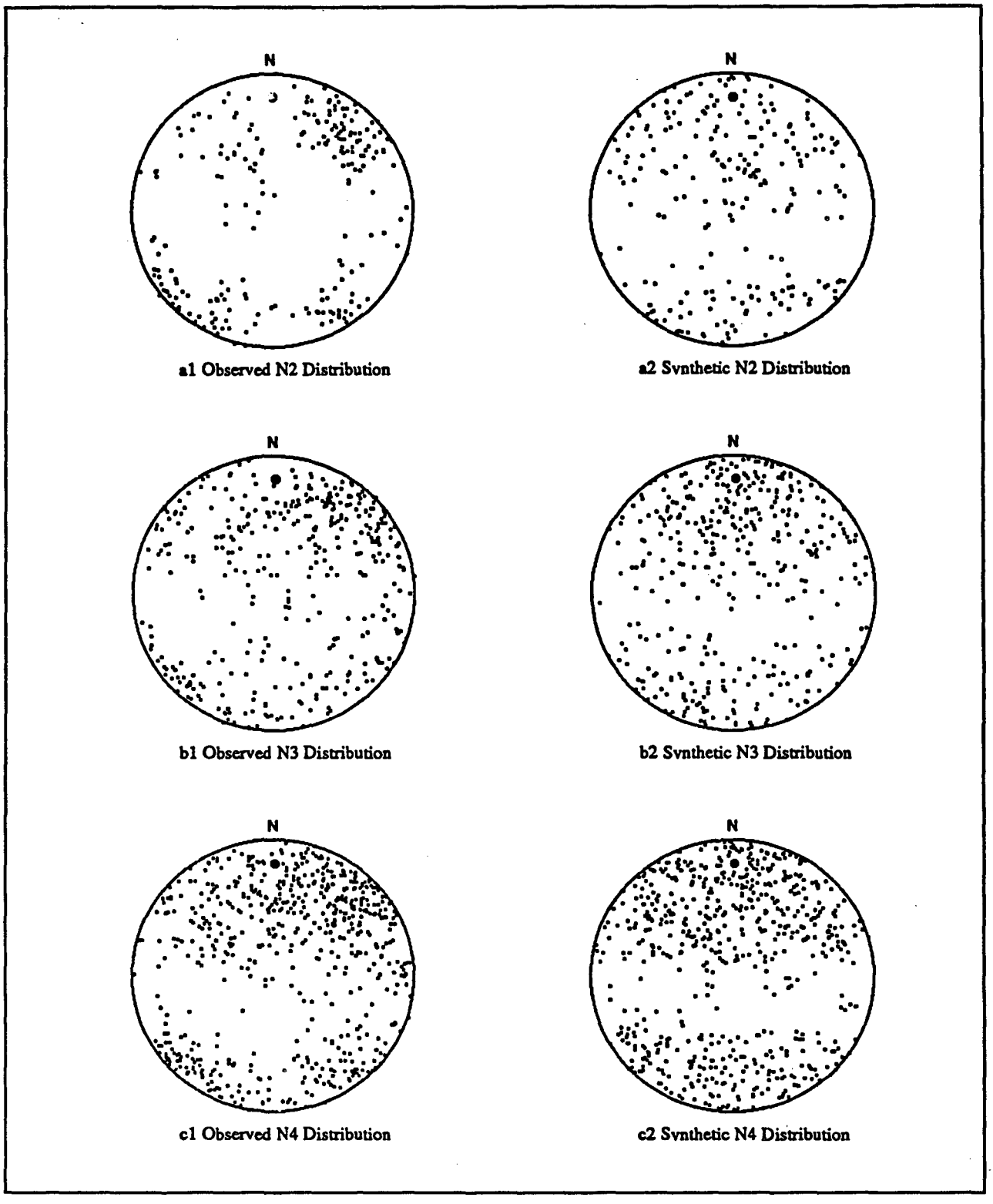

Figure 7.5. Comparison of recorded (left) and synthetic (right) fracture orientation distributions for boreholes a) N2, b) N3, and c) N4. Orientations of boreholes are marked by large dots. Data points touching the borehole orientation dots have been removed for the sake of clarity.

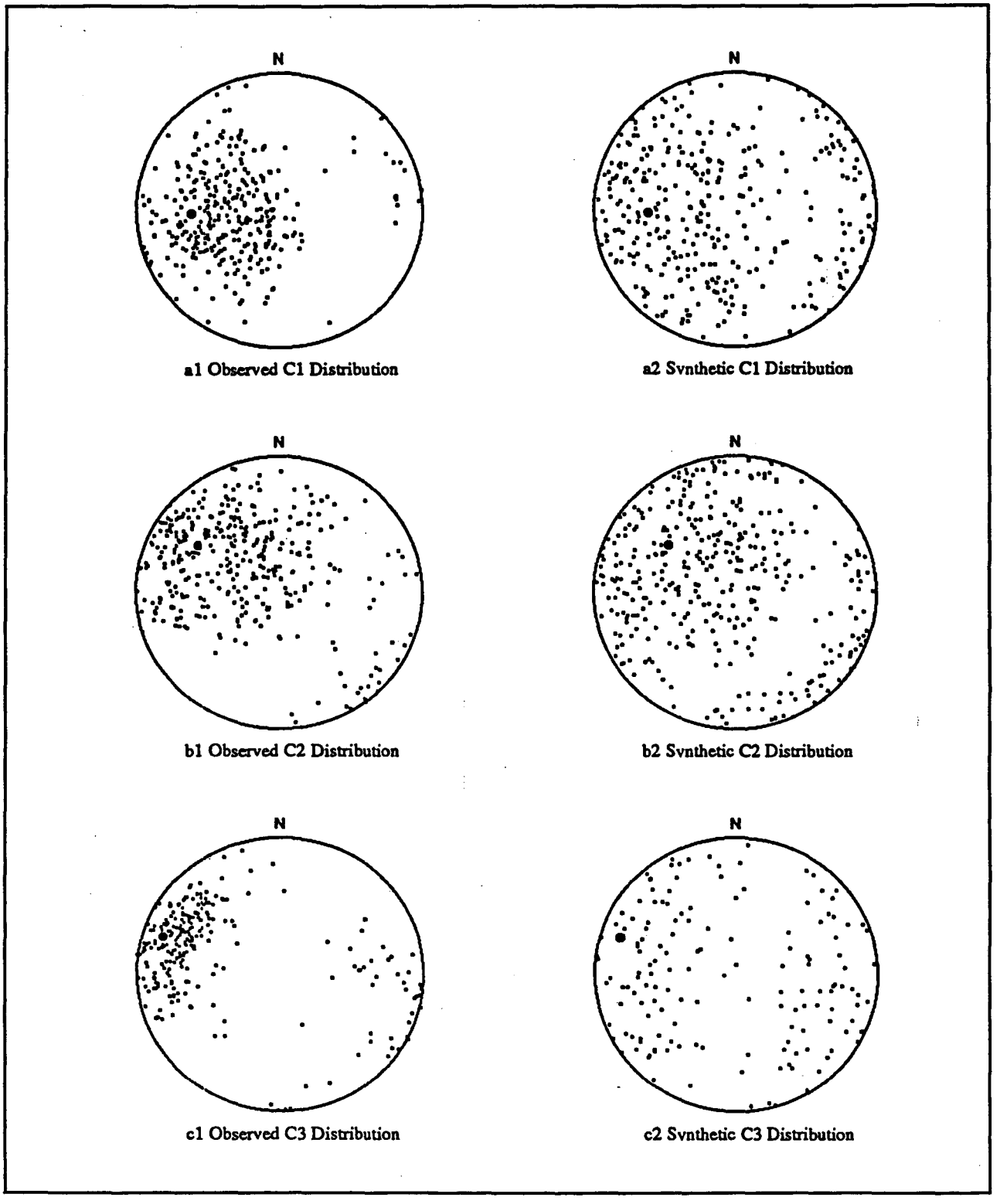

Figure 7.6. Comparison of recorded (left) and synthetic (right) fracture orientation distributions for boreholes a) C1, b) C2, and c) C3. Orientations of boreholes are marked by large dots. Data points touching the borehole orientation dots have been removed for the sake of clarity.

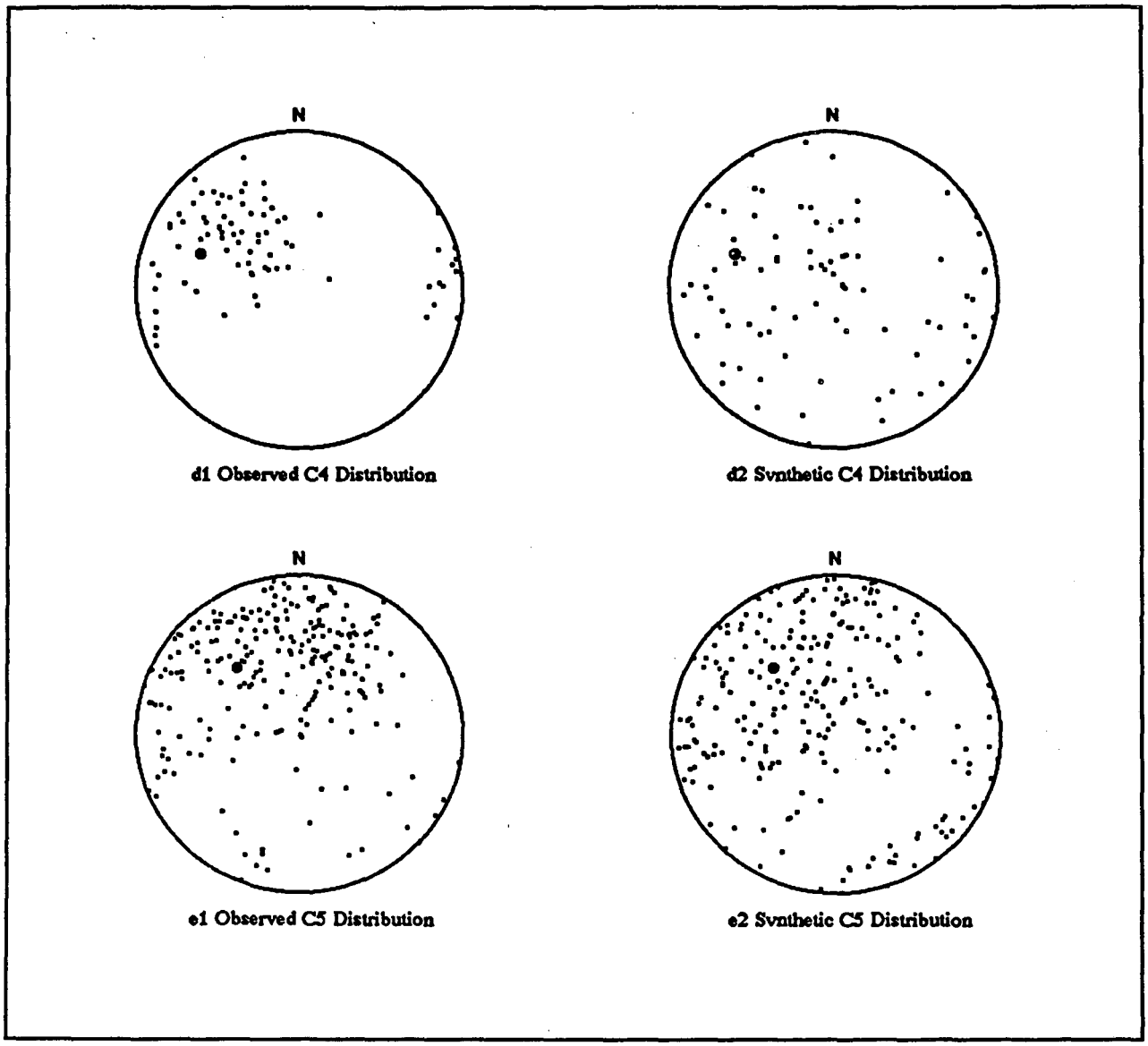

Figure 7.6. (continued). Comparison of recorded (left) and synthetic (right) fracture orientation distributions for boreholes d) C4 and e) C5. Orientations of boreholes are marked by large dots. Data points touching the borehole orientation dots have been removed for the sake of clarity.

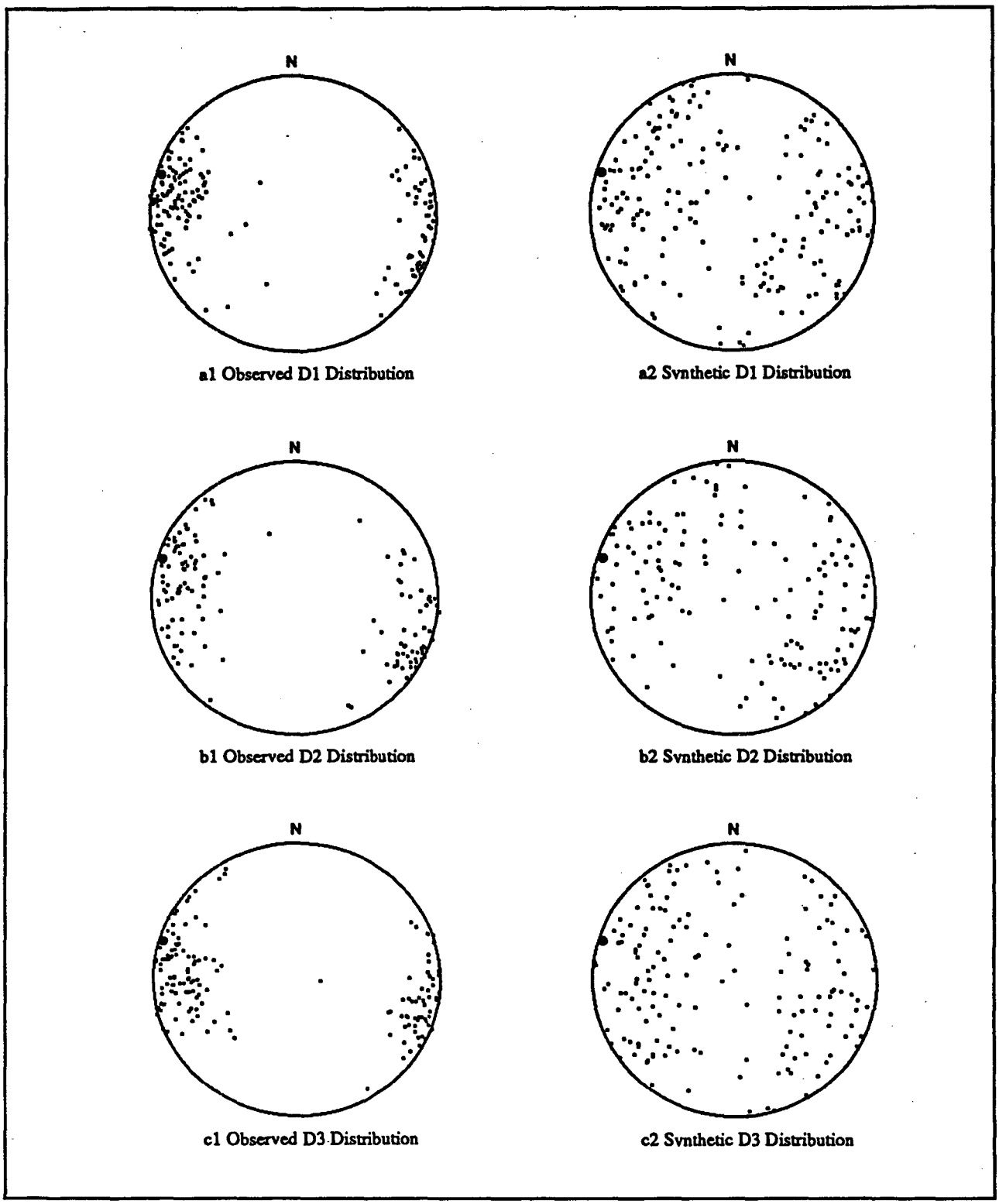

Figure 7.7. Comparison of recorded (left) and synthetic (right) fracture orientation distributions for boreholes a) D1, b) D2, and c) D3. Orientations of boreholes are marked by large dots. Data points touching the borehole orientation dots have been removed for the sake of clarity.

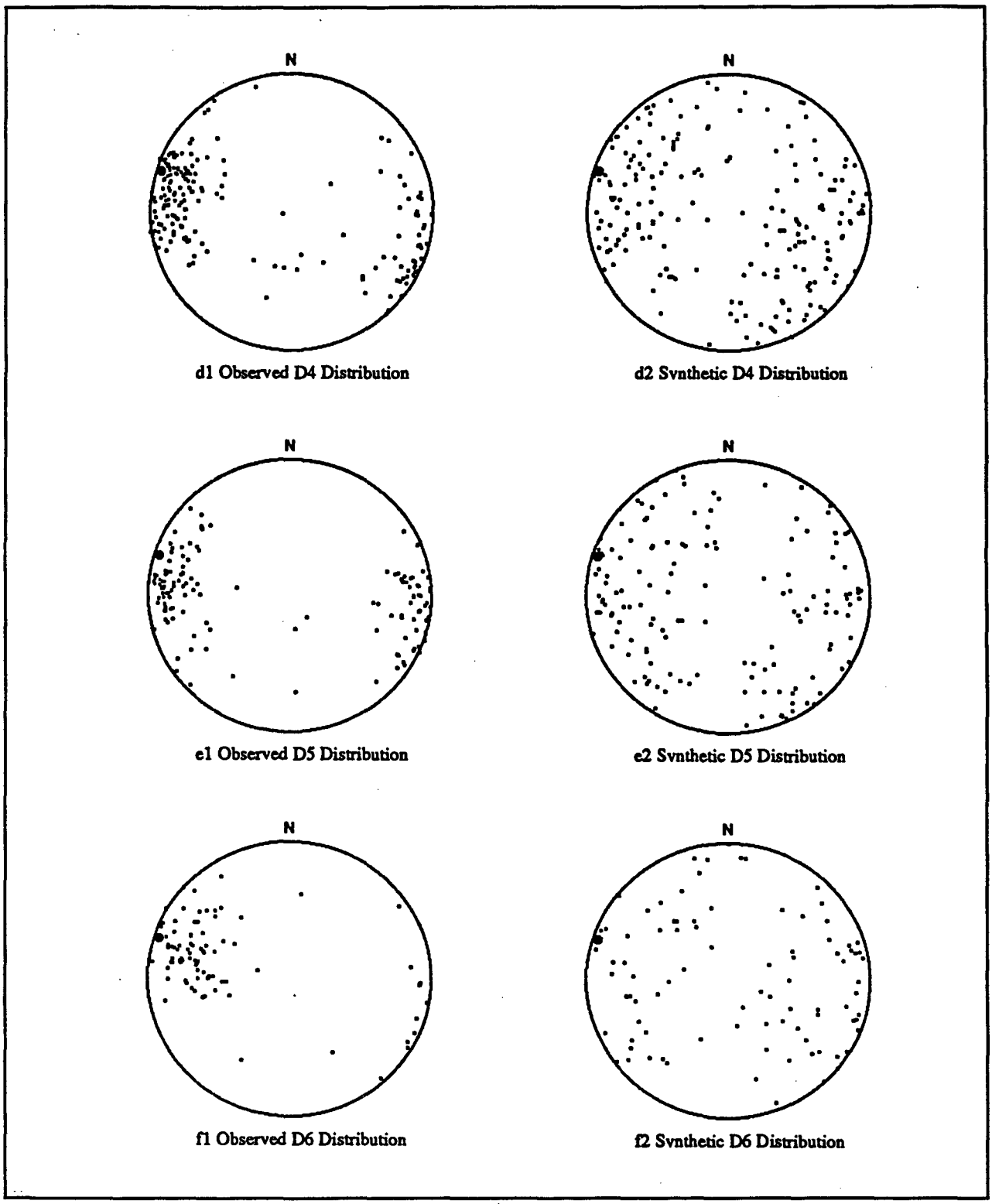

Figure 7.7. (continued). Comparison of recorded (left) and synthetic (right) fracture orientation distributions for boreholes d) D4, e) D5, and f) D6. Orientations of boreholes are marked by large dots. Data points touching the borehole orientation dots have been removed for the sake of clarity.

tightly clustered about the boreholes for the recorded distributions than for the synthetic distributions. These holes, which penetrate zone H, intersect a distinctly higher proportion of fractures with northerly strikes and steep dips than would be the case for a uniform distriubtion. A similar, but somewhat less pronounced concentration of steep fractures with northerly strikes can be inferred for the C holes (Fig. 7.6), which also intersect zone H. In contrast, for the N holes (Fig. 7.5), two of which do not intersect zone H, the recorded and synthetic distributions match quite well. The N holes yield recorded fracture-orientation distributions that are difficult to distinguish from randomly sampled uniform distributions.

The comparisons thus suggest that the SCV fractures have both a chaotic component and a component parallel to zone H. The chaotic component is most pronounced outside zone H, and the zone-parallel component is most pronounced within zone H. This pattern is consistent with the fracturing having accompanied repeated slip along steep north-striking faults during distinctly different episodes of deformation. The borehole data are thus compatible not only with the driftwall observations but also with the inferred history of faulting and fracturing at the mine.

The conclusions reached here regarding the orientations of fractures in the SCV block are compatible with those of Gale and Stråhle (1988) and Gale *et al.* (1990) but have a slighlty different emphasis. As was the case in this study, Gale and his co-workers detected fractures of numerous orientations and concluded that steep north-striking fractures formed the most prominent set. They chose to group fractures of other orientations into a variety of sets. The somewhat simpler interpretation presented here is that these other fractures are largely chaotic.

Gale and his co-workers emphasized the need to carefully collect and analyze borehole orientation data in order to avoid introducing errors into an analysis of fracture orientation data. This point should not be taken lightly. A variety of errors can compound or obscure borehole bias effects. Orientation errors can be introduced in evaluating the orientations of fractures on televiewer or borehole camera logs. Errors can also be introduced when fracture orientations are measured in cores and when these measurements are transformed to give the *in situ* orientations. Finally, the *in situ* orientations of individual segments of core must be determined accurately in order to properly transform the fracture orientation data obtained from core measurements, and this is not a trivial matter. Core orienation errors will tend to randomize the orientation data, increasing the difficulty of detecting fracture sets in largely chaotic fracture distributions.

8 THE MODERN STRESS STATE

The hydraulic conductivity of a fracture depends on its aperture distribution, which in turn is a function of the normal stress acting across the fracture (Tsang and Witherspoon, 1981; Black *et al.*, 1990). The excavation of a tunnel will significantly perturb the stress state around tunnel and thus could significantly affect fluid flow in fractures near the tunnel. This section reviews the data on the modern stress state in the vicinity of the Stripa mine as a prelude to examining how excavating the Validation drift might influence fractures in the SCV block.

The orientation and magnitude of the maximum horizontal compressive stress (S_H) in the vicinity of Stripa can be identified through a combination of regional and local examinations. In southern Sweden S_H is oriented NW-SE based on modern seismicity (Slunga, 1989). This orientation is consistent with the findings from the Fennoscandian Rock Stress Data Base (Stephansson, 1989). The most recent measurements on the stress state at Stripa are by McKinnon and Carr (1990). Their description of the "virgin" stress state for the SCV block is tabled below:

Table 8.1. "Virgin" stress state for the SCV block

Principal Stress	Alternative Name	Trend	Plunge	Magnitude (MPa) by Depth (D) in m
σ_1	S_H	285°	0°	7.5 + 0.044 D
σ_2	S_h	195°	0°	2.5 + 0.035 D
σ_3	S_v	0°	90°	0.0 + 0.026 D

The respective magnitudes of SH, Sh and Sv at a depth of 352 m (mine level of 382 m) are 23.0 MPa, 14.8 MPa and 9.9 MPa. These values compare favorably with earlier values reported by Doe *et al.* (1983). The vertical stress gradient of 2.6 Mpa/m is the unit weight of Stripa granite.

9 POSSIBLE DRIFT EXCAVATION EFFECTS

Possible effects on the inflow to the Stripa Validation drift can be examined in light of the elastic stress perturbations induced by the excavation of the drift to assess whether they are the likely cause of an estimated 8-fold reduction of flow to the Validation region (Olson *et al.*, 1992). The analysis is restricted exclusively to *elastic* effects associated with drift excavation, so potentially important non-elastic excavation effects (such as those accompanying the advance of the front of the drift or those due to blasting) are not considered. Only the changes in conductivity due to changes in normal stress were examined. Changes in normal stress induce relatively straightforward effects on fracture aperture (i.e. increases in the compressive stress applied across a fracture causes the average fracture aperture to decrease) and have been measured in the laboratory (see work by Gale in Black *et al.*, 1990). The effects on fracture aperture due to changes in resolved shear stress are not so straightforward but are probably small on average provided the amount of slip across the fracture is small (Black *et al.*, 1990). Changing the shear stress parallel to a fracture may or may not cause it to slip. If it does slip, then its average aperture may increase or decrease, whereas if it does not slip its average aperture should change very little.

For the purposes of a stress analysis, a drift can be modeled as a long cylindrical cavity under plane strain loading if one of the principal stresses acts parallel to the drift/borehole axis (Fig. 9.1). The Stripa validation drift trends 287° and plunges 3° to the west and the most compressive principal stress is considered to trend 285° and be horizontal, for an angular mismatch of only 4°. The excavated length of the drift as of the writing of this report is approximately 50 m and zone H intersects the drift between 25 and 30 m from the east end of the drift; Figures 5.1-5.3 show the drift before it had been fully excavated. The stresses away from the ends of the drift (i.e. near zone H) are amenable to continuum plane strain modeling. Details of the stress analysis are given in Appendix 3.

Four key points emerge from the stress analysis. First, the elastic stress changes due to the presence of the drift are nearly insignificant more than a few diameters away from the drift (Fig. 9.2). Second, the magnitudes of the elastic stresses or elastic stress changes at the walls of a cylindrical cavity are independent of its radius. The stress levels will be the same along the walls of a 4-cm borehole as along a 2-m-diameter bored drift. However, the perturbing effects of a small-diameter borehole will die off within a shorter distance than the effects of a drift. Third, the maximum and minimum stress levels and stress changes will occur at the walls of the drift ($\theta = 0°$ or 180°) or at its roof and floor ($\theta = 90°$ or 270°). The magnitude of stress or stress change predicted along the Validation drift perimeter (see Table 9.1) were calculated assuming that $\nu = 0.25$ and that S_H, S_h and S_v equal 23.0 MPa, 14.8 MPa and 9.9 MPa, respectively. Fourth, as averaged around the drift perimeter, the radial stress (σ_{rr}) becomes less compressive, the hoop stress ($\sigma_{\theta\theta}$) becomes more compressive as a result of drift excavation, whereas the drift parallel stress (σ_{zz}) and first stress invariant (I_1) do not change.

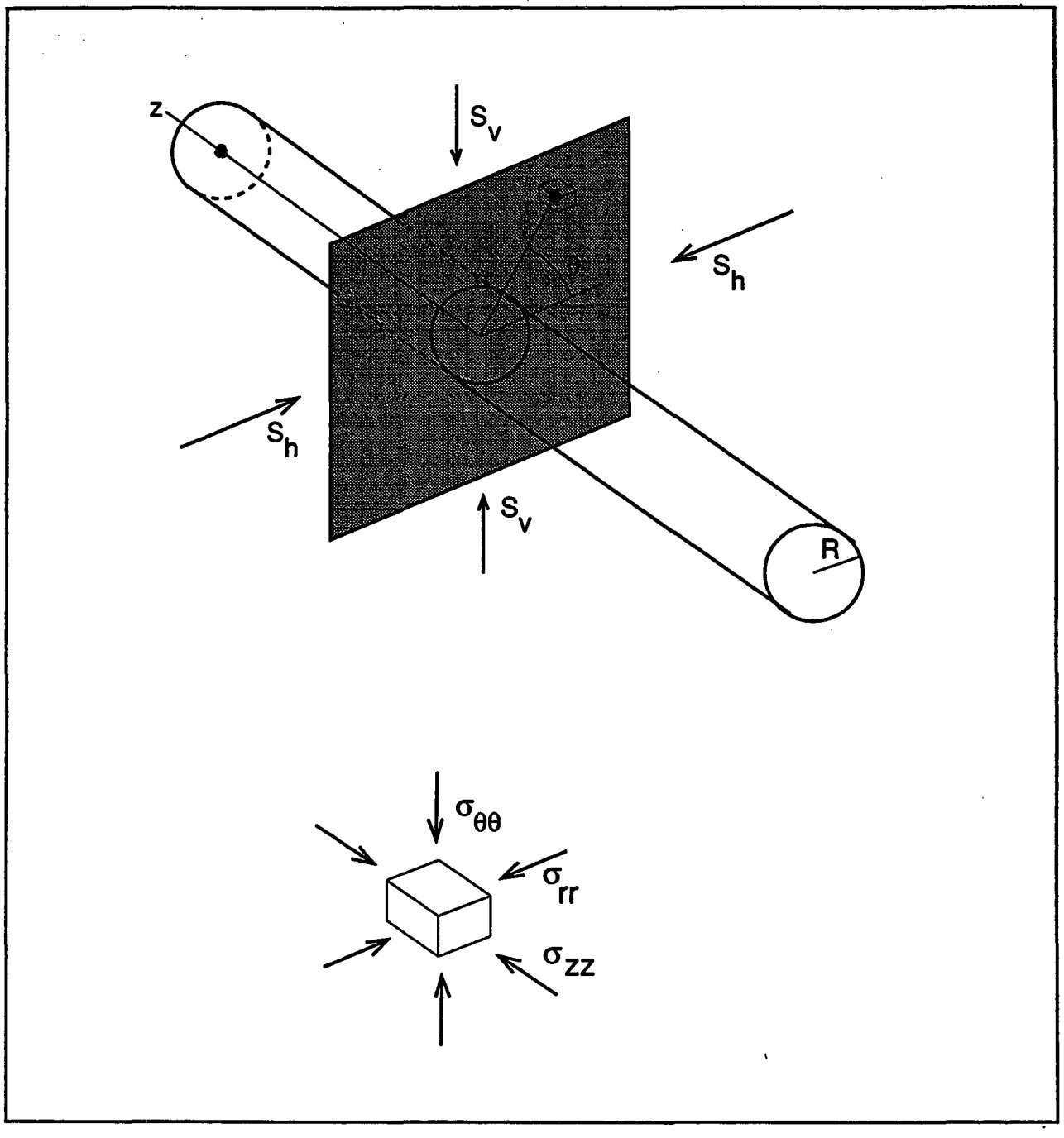

Figure 9.1. Orientation of far-field principal stresses, the Validation drift and the cylindrical coordinate system about the drift.

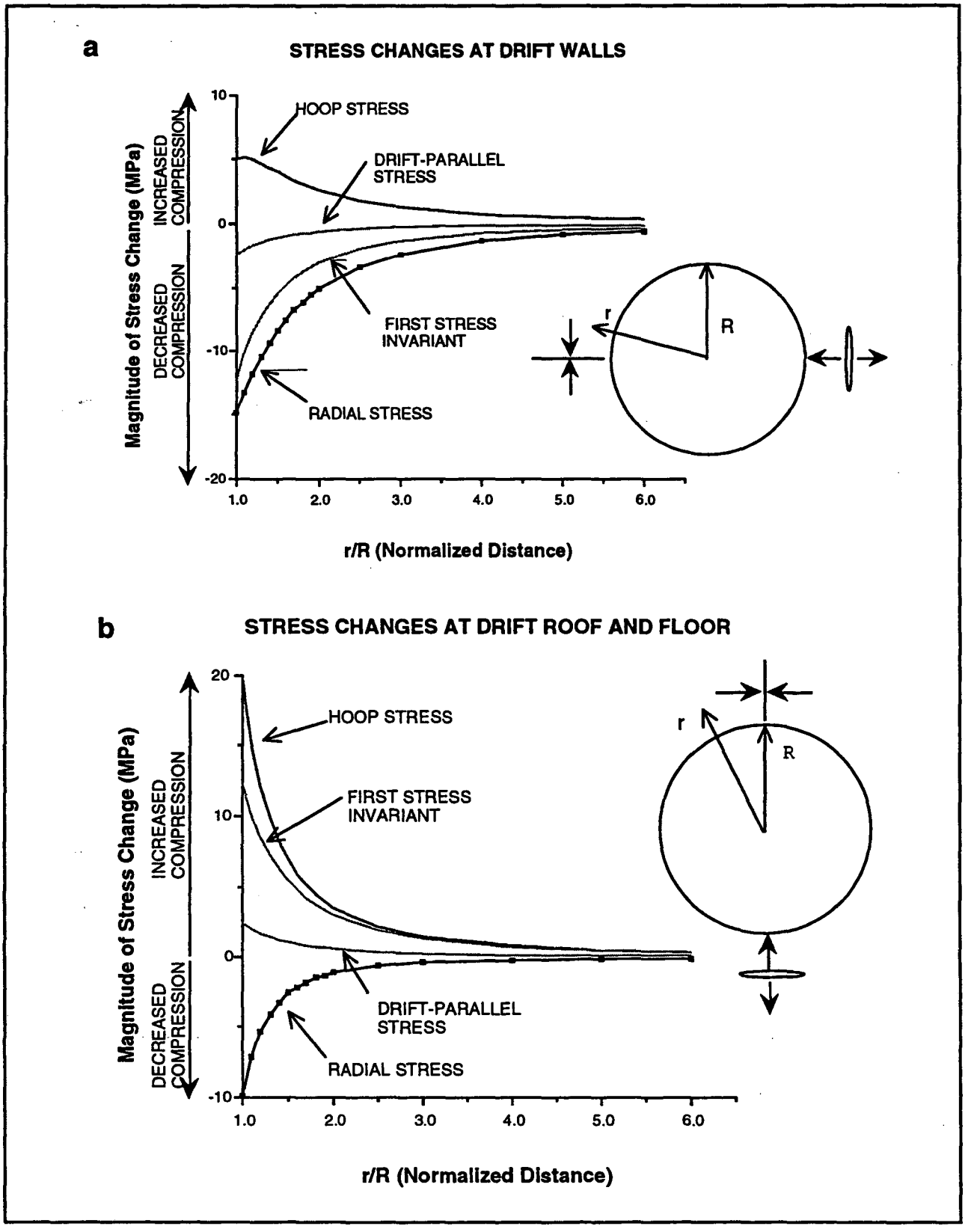

Figure 9.2. Stress changes near a drift plotted as a function of normalized distance from the drift center. a) Stress changes at the drift wall. b) stress changes at the drift floor and roof.

Table 9.1. Predicted post-drift stresses and stress changes along the Validation drift at Stripa (MPa). Positive values are compressive.

Stress	σ_{rr}	$\Delta\sigma_{rr}$	$\sigma_{\theta\theta}$	$\Delta\sigma_{\theta\theta}$	$\tau_{r\theta}$	$\Delta\tau_{r\theta}$	σ_{bar}	$\Delta\sigma_{bar}$	σ_{zz}	$\Delta\sigma_{zz}$	I_1	ΔI_1
Wall, $\theta = 0°$	0	–14.8	14.9	5.00	0	0	7.45	–4.9	20.55	–2.45	35.45	–12.25
Roof, $\theta = 90°$	0	–9.9	34.5	19.70	0	0	17.25	4.9	25.45	2.45	59.95	12.25
Floor, $\theta = 270°$	0	–9.9	34.5	19.70	0	0	17.25	4.9	25.45	2.45	59.95	12.25

Excavation of the drift clearly results in a significant redistribution of stress near the drift. The vertical compressive stress acting before the drift was excavated was 9.9 MPa; after excavation the vertical compressive stress along the wall ($\theta = 0$) would be 14.9 MPa, for an increase of 51%. Horizontal fractures at the drift wall would tend to squeeze shut in response to the elastic effects caused by excavation of the drift. The elastic effects are even more pronounced at the top of the drift and at its floor. The post-drift level of hoop stress at the roof is 34.5 MPa. This represents an increase of 133%. As a result, vertical fractures at the roof that parallel the drift would tend to close down more than horizontal fractures at the drift walls.

Fractures oriented perpendicular to the drift are affected less by the excavation of the drift. At the walls of the drift, the drift-parallel compressive stress would be reduced by 11%; at the roof and floor the compressive stress is increased by this amount. An inspection of Eq. A31 (Appendix 3) reveals that the net effect around the perimeter of the drift is zero.

The normal stress acting on the drift walls is atmospheric pressure, so the excavation of the drift results in a radial compressive stress decrease at the drift walls of essentially 100%. As a result of the decompression, fractures that ring the drift will open; points of contact which locally had propped the fractures open will now cause the fracture walls to separate more. However, because of their orientation, fractures parallel to the drift axis would not conduct water directly into the drift.

According to laboratory work by Gale and co-workers (presented by Black *et al.*, 1990) on the effect of normal stress on fracture conductivity, fracture hydraulic conductivity varies as σ_n^{α}, where σ_n is the applied normal stress and α is an experimentally determined coefficient that appears to range between 0 and –1. Because the absolute magnitude of α is generally less than one, the hydraulic conductivity changes at a lower rate than the applied normal stress; if $\alpha = -0.25$ (a reasonable value based on the laboratory tests), then doubling the compressive stress across a fracture will decrease conductivity by only 16%. Given the results of the stress analysis, fractures oriented radially with respect to the drift would sustain conductivity losses no more than 55% near the drift even if $\alpha = -1.5$. The normal stress changes on fractures oriented approximately perpendicular to the drift (i.e. the longer fractures in zone H) will result in only minor changes to their conductivity.

A more detailed analysis of the conductivity response of the fractured rock to the stress changes bears these conclusions out. The fracture hydraulic conductivity after opening of a drift can be normalized by the ambient (pre-drift) conductivity in the following manner

$$k_r^* = C\,\sigma_{n(\text{post-drift})}^{\alpha} / C\,\sigma_{n(\text{pre-drift})}^{\alpha} \qquad (1)$$

$$k_r^* = \{\sigma_{n(\text{post-drift})} / \sigma_{n(\text{pre-drift})}\}^{\alpha} \qquad (2)$$

By using the equations for post-drift stresses in Appendix 3 (equations A6, A7, and A15) and the pre-drift (ambient) stresses from Table 9.1, one can calculate normalized fracture conductivities as a function of distance from the drift using equation 2. Figure 9.3 shows normalized conductivity values for vertical fractures that radiate from the Validation drift roof. Those fractures would be subject to the greatest changes in normal stress and the greatest attendant decrease in conductivity. Figure 9.3 also lists effective conductivities as averaged over a distance of four drift radii beyond the drift; Appendix 4 gives details for how the effective values are calculated. Beyond four radii the stress redistribution effects should be negligible. Even if α has the unusually large magnitude of -1.50, the effective fracture conductivity on the most significantly affected fractures would decrease by less than 10%. The analysis strongly suggests that the estimated 8-fold reduction to the drift is due largely to factors other than elastic stress redistribution effects.

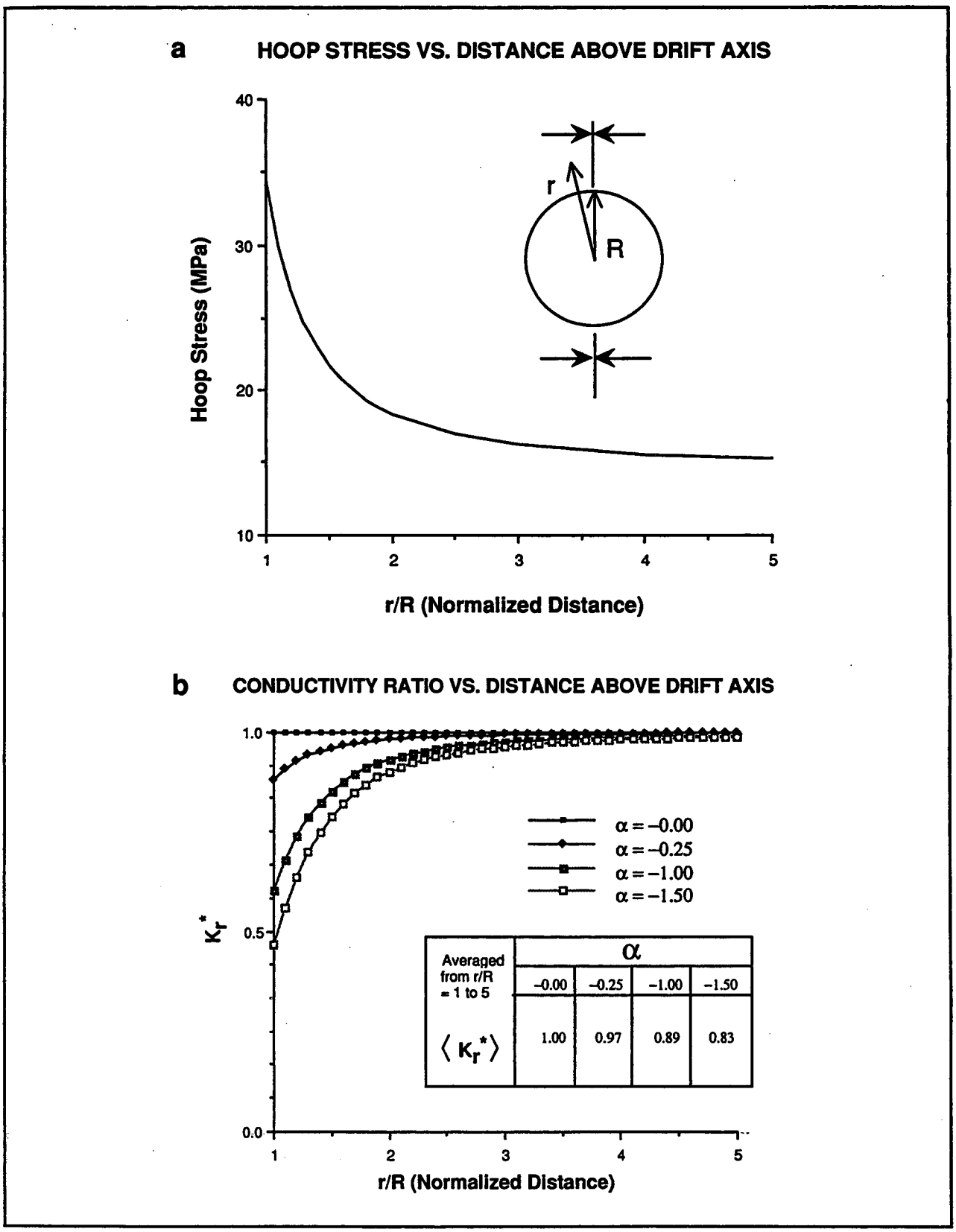

Figure 9.3. a) Hoop stress ($\sigma_{\theta\theta}$) above drift axis. b) Normalized fracture hydraulic conductivities predicted for a vertical, drift-parallel fracture at the roof of the Validation drift.

10 CONCLUSIONS

Of the major fracture zones inferred within the SCV block, zone H (together with HB) has the most prominent radar and seismic fingerprint. It may coincide with a structure several kilometers long identified through a regional aeromagnetic survey. Based largely on geophysical evidence, zone H is inferred to strike 355° and dip 76° to the east, and zone Hb is inferred to strike 353° and dip 60° to the east. Zones H and Hb cannot be distinguished from one another in the drift exposures and are considered to represent a single zone, zone H. Zone H exposures are characterized by a red granite that contrasts sharply with the grey granite typical of the mine. The thickness of the red granite across zone H appears to vary from ~5 m to ~40 m. The color of zone H is its most distinguishing feature; its edges are not sharply defined based on either the intensity or orientation of its fractures. The plane that passes through the center of zone H exposures at the 310-, 360- and 410-m depth levels in the mine strikes N-S and dips ~64° to the east. This orientation has an uncertainty of several degrees in strike and dip and cannot be distinguished from the orientations for the separate zones given above. The zone thickness decreases from the 310 level to the 410 level; this is consistent with geometry inferred from geophysical data for the H-Hb combination.

Sealed fractures of numerous orientations occur at zone H exposures. Most individual fractures are difficult to trace more than a few meters. However, the longest fractures in zone H exposures typically strike to the north and dip steeply to the east, subparallel to the zone as a whole. Many of the fractures in zone H are faults. At the 360 level, the longest fractures west of the zone generally strike 20° or somewhat more to the west and east of the zone they strike 20° or more to the east.

The steeply-dipping faults with a northerly strike apparently have accommodated different styles of slip. Evidence for normal dip slip on these faults is most pronounced and is evidenced by a) fault surfaces with slickenlines that plunge down dip, b) faults being linked by steeply inclined fractures or cavities and c) displaced subhorizontal veins. The strong fingerprint for normal slip along the north-striking faults suggests that the H-zone may have been active when north-striking dikes were being intruded in southern Sweden and/or when normal faulting occurred on the Protogine zone, a large north-striking fault/shear zone belt 80 km west of Stripa. Some faults show evidence for reverse slip. Finally, some faults have accommodated right-lateral strike slip based on steeply-dipping fractures that splay to the northeast. The rather chaotic arrangement of fractures in zone H, the structural evidence for at least three episodes of slip on zone-parallel faults and previously published evidence for at least two episodes of mineralization along fractures at Stripa are consistent with zone H being an old reactivated fault zone.

Although most of the permeability and much of the porosity in the Stripa granite is due to the fractures, some porosity occurs in the form of pitting. Some borehole cores are pitted and in one case a pitted region in the SCV block has been located through geophysical techniques. The pitting has been interpreted to reflect dissolution of quartz from the granite. Pitting also occurs in a drift exposure at the 410 level along an H zone fault. At that spot fluorite was precipitated in pits in the granite and calcite was precipitated in cavities along the fault. These observations suggest that some secondary porosity in the SCV block may be due to the concentrated flow of reactive fluids along fractures.

Direct information on the fractures within the SCV site comes from four sets of boreholes. Although these holes trend in a variety of directions, most are shallowly inclined, so they are best-oriented to detect steeply-dipping fractures. Most of the fractures that are open in recovered drill

cores are along pre-existing mineralized (or otherwise sealed) fractures. Independent of the location and orientation of a borehole, there is a strong tendency for the fractures intersected by a hole to be nearly perpendicular to the borehole. To test the extent to which this reflects borehole sampling bias, the actual fracture orientation distribution encountered in each borehole was compared with a synthetic distribution obtained as if the borehole had sampled a uniform distribution of fracture orientations. The comparison indicates 1) there probably is a strong uniform component to the actual distribution of *in situ* fracture orientations and 2) the observed distribution is strongly affected by the orientation of the borehole. The holes through zone H do show a higher density of steeply-dipping fractures that strike subparallel to the zone than would be expected if the *in situ* distribution of orientations were uniform. Zone-parallel fractures are therefore larger and/or more abundant within zone H than fractures of other orientations. The conclusion that zone H contains fractures of numerous orientations, but with fractures subparallel to the zone being largest or most common, squares with the drift wall observations by the author.

The hydraulic conductivity of a fracture in zone H is expected to reflect the orientation of the fracture and the current stress field. Based solely on the varied orientations of fractures in zone H, one might expect its bulk conductivity to be nearly isotropic. However, because the stress field at the mine appears to be strongly anisotropic, the hydraulic conductivities of the fractures in the zone should vary as a function of their orientation. The most conductive fractures are likely to be perpendicular to the least compressive stress and the least conductive perpendicular to the most compressive stress. The stress measurements in the mine to date indicate that the most compressive horizontal stress is oriented WNW and the least compressive stress is vertical. Steeply-dipping fractures that strike NNE would tend to have the smallest apertures on the average and be least conducive to flow. This is approximately the orientation of the longest fractures in zone H.

The opening of a drift will significantly perturb the stress field in the adjacent rock and hence could potentially change the fracture conductivity within a few diameters of a drift. The elastic effects will be strongest at the drift walls and will die out within a few diameters of a drift. The magnitude of these effects will depend on the orientations of the drift, on the far-field principal stresses, and on the orientation of the fractures near the drift. In most cases, the excavation of a drift at depth will promote the opening of pre-existing fractures that parallel the perimeter of the drift, whereas pre-existing fractures oriented such that they radiate from the drift will tend to close. The effect on fractures that are approximately perpendicular to the drift axis would be minor. Because the radial and drift-perpendicular fractures would carry water into the drift, the stress effects on these fractures are particularly important. The perturbing effects would be greatest for drifts that trend perpendicular to the most compressive far-field principal stress (σ_1) and least for drifts that trend parallel to σ_1; the latter case describes the situation with the Validation drift at Stripa. For a drift oriented obliquely to the principal stress axes, perturbation effects will vary significantly along the drift.

The elastic stress perturbation caused by the excavation of the Validation drift was analyzed to examine the possible effect of inflow to the drift along zone H. The Validation drift at Stripa trends at 287°, and is inclined down to the WNW at 3°, and has a radius of approximately 1.5 m. Zone H intersects the drift approximately 30 m from its east end. The orientations of the drift and the most compressive far-field horizontal stress differ by only 4°, indicating that a 2-D plane strain analysis is useful for analyzing the stress effects on zone H due to excavation. Using the most recent stress measurements for the SCV area, the compressive normal stress tangential to the drift should increase between 50% (at the drift walls) and 133% (at the roof and floor of the drift); these effects

decay to less than 10% within a few meters from the drift. At the levels of normal stress near the Validation drift, the experimental work of Gale (Black *et al.*, 1990) suggests that the ratio of the change in fracture hydraulic conductivity to the change in normal stress is between zero and one; the changes are related by a power law. The hydraulic conductivity along fractures oriented radially to the drift should decrease by less than 10% as averaged over a 6-m distance from the drift. The absolute magnitude of the normal stress changes parallel to the drift are small (<15%) and average to zero around the perimeter of the drift. There should be little direct effect on the inflow along drift-perpendicular fractures (i.e. the longest H zone fractures). The excavation of the drift causes the compressive stress normal to the drift walls to be reduced to atmospheric pressure and pre-existing fractures that ring the drift should open. The hydraulic conductivity of these fractures should increase, but they would not be oriented to conduct water into the tunnel; they might be able to store water or air, however. Elastic stress changes should have little direct effect on fracture conductivity along zone H near the Validation drift and are unlikely to account by themselves for an inferred 8-fold reduction in flow into the drift region.

11 ACKNOWLEDGMENTS

Special thanks to Kai Front, Jane Long, Jahan Noorishad, John Peterson, and especially Steve Flexser for reviewing this report and to Gunnar Rahmqvist at the Stripa mine for his logistical support. John Peterson's help in developing the concepts and computer techniques used to analyze the fracture orientation data is gratefully acknowledged. The fracture orientation data were provided courtesy of John Gale. Judith Peterson was instrumental in the final preparation of the manuscript. This work was supported by the U.S. Department of Energy through the Director, Office of Civilian Radioactive Waste Management, Office of External Relations, under Contract No. DE-AC03-76SF00098.

12 REFERENCES

Abelin, H. and L. Birgersson, 1987. 3-D migration experiment—Report 1: Site Preparation and Documentation, Stripa Project technical report 87–19.

Andersson, P., 1989. Site characterization and validation - geophysical single hole logging, stage 3, Stripa Project technical report 89-07.

Andréasson, P-G and Rodhe, A., 1990. Geology of the Protogine Zone south of Lake Vättern, southern Sweden: a reinterpretation: Geologiska Föreningens I Stockholm Förhanlingar, v. 112. p. 107-125.

Bäckblom, G. and Stanfors, R. (eds.), 1989. Interdisciplinary study of post-glacial faulting in the Lansjarv area northern Sweden: SKB Technical Report 89-31.

Billaux, D., J.P. Chiles, K. Hestir and J.C.S. Long, 1989. Three-dimensional statistical modeling of a fractured rock mass—an example from the Fanay-Augeres mine, International Journal of Rock Mechanics and Mining Sciences and Geomechanics Abstracts, 26, 281–299.

Black, J.H., O. Olsson, J.E. Gale and D.C. Holmes, 1990. Site characterization and validation - stage 4—preliminary assessment and detail predictions, Stripa Project technical report 91-08.

Bylund, G., 1992. Palaeomagnetism, mafic dykes and the Protogine zone, southern Sweden: Tectonophysics, v. 201, p. 49-63.

Carlon, C.J. and Bjurstedt, S., 1990. Stratabound and stratiform sulphide mineralization in the evolution of the Guldsmedshyttan syncline, Bergslagen, south-central Sweden: Geologiska Föreningens I Stockholm Förhanlingar, v. 112. p. 176-177.

Carlsson, L., Egerth, T. and Westlund, B., 1982. Core-logs of the vertical borehole V2: Stripa Project internal report 82-05.

Carlsten, S., 1985. Hydrogeological and hydrogeochemical investigations in boreholes—compilation of geological data, Stripa Project internal report 85-04.

Carslaw, H.S. and Jaeger, J.C., 1984. Conduction of heat in solids: Clarendon Press, Oxford, 510 p.

Dallmeyer, R.D., Gee, D.G. and Beckholmen, M., 1985. 40Ar/39Ar mineral age record of early Caledonian tectonothermal activity in the Baltoscandian miogeocline, central Scandinavia: American Journal of Science, v. 285 , p. 532-568.

Dallmeyer, R.D. and Gee, D.G., 1986. 40Ar/39Ar mineral dates from retrogressed eclogites within the Baltoscandian miogeocline: implications for a polyphase Caledonian orogenic evolution: Geological Society of America Bulletin, v. 97 , p. 26-34.

Dallmeyer, R.D., Peucat, J.J. and Ohta, Y., 1990. Tectonothermal evolution of contrasting metamorphic complexes in northwest Spitsbergen (Biskayerhalvøya): evidence from 40Ar/39Ar and Rb-Sr mineral ages: Geological Society of America Bulletin, v. 102 , p. 653-663.

Daly, J.S., Park, R.G. and Cliff, R.A., 1983. Rb-Sr isotope equilibrium during the Sveconorwegian (=Grenville) deformation and metamorphism of the Orust dykes, S.W. Sweden: Lithos, v. 16, p. 307-318.

Delaney, P.T., Pollard, D.D., Ziony, J.I. and McKee, E.H., 1986. Field relations between dikes and joints: emplacement processes and paleostress analysis: Journal of Geophysical Research, v. 91, p. 4920-4938.

Doe, T.W., K. Ingevald, L. Strindell, B. Leijon, W. Hustrulid, E. Majer and H. Carlsson, 1983. In situ stress measurements at the Stripa mine, Sweden: Lawrence Berkeley Laboratory Report LBL-15009, 251 p.

Erlstrom, M., 1987. Complex fracture-filling material from the Singo fault zone at Forsmark, central Sweden: Geologiska Föreningens I Stockholm Förhanlingar, v. 109, p. 55-58.

Fridh, B., 1987. Site characterization and validation - geophysical single hole logging, Stripa Project technical report 87-17.

Gale, J. and Stråhle, A., 1988. Site characterization and validation - drift and borehole fracture data, stage 1, Stripa Project internal report 88-10.

Gale, J., MacLeod, R., Stråhle, A. and Calrsten, S., 1990. Site characterization and validation-drift and borehole fracture data, stage 3, Stripa Project internal report 90-02.

Gorbatschev, R., 1980. The Precambrian development of southern Sweden: Geologiska Föreningens I Stockholm Förhanlingar, v. 102, p. 129-136.

Hjelmqvist, S., 1975. A Rhenish fault on the southern border of the Baltic shield: Geologiska Föreningens I Stockholm Förhanlingar, v. 97, p. 89-91.

Jaeger, J.C. and Cook, N.G.W., 1979. Fundamentals of rock mechanics: Chapman and Hall, London, 593 p.

Klingspor, I., 1976. Radiometric age-determinations of basalts, dolerites and related syenite in Skåne, southern Sweden: Geologiska Föreningens I Stockholm Förhanlingar, v. 98, p. 195-216.

Kreith, F., 1967. Principles of heat transfer: International Textbook Company, Scranton, Pennsylvania, 620 p.

Lagerbäck, R., 1979. Neotectonic structures in northern Sweden: Geologiska Föreningens I Stockholm Förhanlingar, v. 100, p. 263-269.

Larson, S.Å., Stigh, J. and Tullborg, E-L., 1986. The deformation history of the eastern part of the southeast Swedish gneiss belt: Precambrian Research, v. 31, p. 237-257.

Lindblom, S., 1984. Hydrogeological and hydrogeochemical investigations in boreholes - fluid inclusion studies in the Stripa granite, Stripa Project internal report 89-07.

Long, J.C.S., K. Hestir, K. Karasaki, A. Davey, J. Peterson, J. Kemeny and M. Landsfeld, 1989. Fluid flow in fractured rocks: theory and application, Lawrence Berkeley Laboratory Report LBL-27879, 37 p.

Long, J.C.S., Karasaki, K., Davey, A., Peterson, J., Landsfeld, M., Kemeny, J. and Martel, S., 1990. Preliminary prediction of inflow into the D-holes at the Stripa mine, Lawrence Berkeley Laboratory Report LBL-27182, 100 p.

Long, J.C.S., Karasaki, K., Davey, A., Peterson, J., Landsfeld, M., Kemeny, J. and Martel, S., 1991. An inverse approach to the construction of fracture hydrology models conditioned by geophysical data: International Journal of Rock Mechanics and Mining Sciences & Geomechanics Abstracts, v. 28, p. 121-142.

Lopez-Montano, R., and Nisca, D.H., 1987. Geology of the Eskilstuna SW and SE map-sheets, south central Sweden: interpretation of aeromagnetic maps: Geologiska Föreningens I Stockholm Förhanlingar, v. 109, p. 159-163.

Lundqvist, T., 1979. The Precambrian of Sweden: Sveriges Geologistea Undersökning, series C, no. 768, 87 p.

Magnusson, N.H., 1960. Age determinations of Swedish Precambrian rocks: Geologiska Föreningens I Stockholm Förhanlingar, v. 82, p. 407-432.

Martel, S.J., Pollard, D.D. and Segall, P., 1988. Development of simple fault zones in granitic rock, Mount Abbot quadrangle, Sierra Nevada, California: Geological Society of America Bulletin, v. 100, 1451–1465.

Martel, S.J. and Pollard, D.D., 1989. Mechanics of slip and fracture along fault zones in granitic rock, Mount Abbot quadrangle, Sierra Nevada, California: Journal of Geophysical Research, v. 94, p. 9417-9428.

Martel, S.J., 1990. Development of compound fault zones in granitic rock, Mount Abbot quadrangle, Sierra Nevada, California: Journal of Structural Geology, v. 12, p. 869-882.

Martel, S.J. and J.E. Peterson, Jr., 1990. Use of integrated geologic and geophysical information for characterizing the structure of fracture systems at the US/BK site, Grimsel Laboratory, Switzerland, Lawrence Berkeley Laboratory report LBL-27912, 116 p.

McKinnon, S. and P. Carr, 1990. Site characterization and validation-stress field in the SCV block and around the validation drift, stage 3, Stripa Project technical report 90-09.

Mörner, N-A., 1979. Earth movements in Sweden, 20 000 BP to 20 000 AP: Geologiska Föreningens I Stockholm Förhanlingar, v. 100, p. 279-286.

Mörner, N-A., 1980. The Fennoscandianuplift: geological data and their geodynamical implication, in Mörner, N-A., ed., Earth Rheology, Isostasy and Eustasy, John Wiley and Sons, New York, p. 251-284.

Munier, R., and Tirén, S., 1989. Geometry and kinematics of deformation zones in the Finnsjön area, central eastern Sweden: a deformation system controlled by five sets of shear zones: University of Uppsala Department of Mineralogy and Petrology report 59, 32 p.

Muir Wood, R., 1989. Extraordinary deglaciation reverse faulting in northern Fennoscandia, in Gregersen, S. and Basham, P.W., eds., Earthquakes at North-Atlantic Passive Margins: Neotectonics and Postglacial Rebound, p. 141-173.

Olkiewicz, A., J.E. Gale, R. Thorpe and B. Paulsson, 1979. Geology and fracture system at Stripa, Lawrence Berkeley Laboratory report LBL-8907, 164 p.

Olsson, O., J.H. Black, J.E. Gale and D.C. Holmes, 1989. Site characterization and validation Stage 2—preliminary predictions: Stripa Project technical report 89-03.

Olsson, O., Barton, N., Birgersson, L., Dershowitz, W., Black, J., Cosma, C., Gale, J., Herbert, A., Holmes, D., Laaksuharju, M., Long, J. and Neretniks, I., 1992. Site characterization and validation - final report: Stripa Project technical report (in preparation).

Patchett, P.J. and Bylund, G., 1977. Age of Grenville belt magnetisation: Rb-Sr and palaeomagnetic evidence from Swedish dolerites: Earth and Planetary Science Letters, v. 35, p. 92-104.

Patchett, P.J., 1978. Rb-Sr ages of Precambrian dolerites and syenites in southern and central Sweden: Sveriges Geologiska Undersokning C747, 63 p.

Priem, H.N.A., Mulder, F.G., Boelrjik, N.A.I.M., Hebeda, E.H., Verschure, R.H. and Verdurmen, E.A.,Th., 1968. Geochronological and palaeomagnetic reconnaissance survey in parts of central and southern Sweden: Physics of the Earth and Planetary Interiors, v. 1, p. 373-380.

Röshoff, K.O., 1979 The tectonic-fracture pattern in southern Sweden in Fennoscandia: Geologiska Föreningens I Stockholm Förhanlingar, v. 100, p. 255-261.

Segall, P. and Pollard, 1983. Nucleation and growth of strike-slip faults in granite, Journal of Geophysical Research, 88, 555–568.

Simon, S., 1987. Caledonian deformation of basement in the Lockne area, Jämtland, central Sweden: Geologiska Föreningens I Stockholm Förhanlingar, v. 109, p. 269-273.

Slunga, R., 1989. Earthquake mechanisms in northern Sweden Oct 1987–Apr 1988, SKB Technical Report 89-28, 165 p.

Stephansson, O., 1979. Seismotectonics in Fennoscandia: Geologiska Föreningens I Stockholm Förhanlingar, v. 100, p. 239-245.

Stephansson, O., 1989. Stress measurements and modelling of crustal rock mechanics in Fennoscandia, in Gregersen, S. and Basham, P.W., eds., Earthquakes at North-Atlantic Passive Margins: Neotectonics and Postglacial Rebound, p. 213-229.

Talbot and Heeroma, 1989. Cover/basement relationships in the SW Swedish gneisses near Varberg: Geologiska Föreningens I Stockholm Förhanlingar, v. 111, p. 105-119.

Talbot, C. and Munier, R., 1989. Faults and fracture zones in Aspö: Swedish Nuclear Fuel and Waste management Co, SKB, Swedish Hard Rock Laboratory, Progress Report 25-89-11, 58 p.

Talbot, C.J. and Slunga, R., 1989. Patterns of active shear in Fennoscandia, in Gregersen, S. and Basham, P.W., eds., Earthquakes at North-Atlantic Passive Margins: Neotectonics and Post-glacial Rebound, p. 441-466.

Talbot, C.J., 1990. Problems posed to a bedrock radwaste repository by gently dipping fracture zones: Geologiska Föreningens I Stockholm Förhanlingar, v. 112. p. 355-359.

Talvitie, J., 1979. Seismic-tectonics in Finland: Geologiska Föreningens I Stockholm Förhanlingar, v. 100, p. 247-253.

Terzaghi, R., 1965. Sources of error in joint surveys: Geotechnique, v.15, p. 287-304.

Thorpe, R., 1979. Characterization of discontinuities in the Stripa granite time-scale heater experiment, Lawrence Berkeley Laboratory report LBL-7083, 107 p.

Timoshenko, S.P. and Goodier, J.N., 1970. Theory of elasticity, McGraw-Hill, New York, 567 p.

Tirén, S.A. and Beckenholmen, M., 1989. Block faulting in southeastern Sweden interpreted from digital terrain models: Geologiska Föreningens I Stockholm Förhanlingar, v. 111. p. 171-179.

Tirén, S.A. and Beckenholm, M., 1990. Influence of regional shear zones on the lithological pattern in central Sweden: Geologiska Föreningens I Stockholm Förhanlingar, v. 112. p. 197-199.

Tsang, Y.W. and P.A. Witherspoon, 1981. Hydromechanical behavior of a deformable rock fracture subject to normal stress, Journal of Geophysical Research, 86, 9287–9298.

Welin, E. and Blomqvist, G., 1966. Further measurements on radioactive minerals from Sweden: Geologiska Föreningens I Stockholm Förhanlingar, v. 112. p. 206.

Welin, E., 1990. Geochronological overview of Bergslagen and adjacent areas, central Sweden: Geologiska Föreningens I Stockholm Förhanlingar, v. 88. p. 3-18.

Wikström, A., 1985. The Brevern dolerite dike in south central Sweden and an eastward extension of dolerite-granophyre breccia, Geologiska Föreningens I Stockholm Förhanlingarv. 107, p. 37-40.

Wollenberg, H., S. Flexser and L. Andersson, 1980. Petrology and Radiogeology of the Stripa pluton, Lawrence Berkeley Laboratory report LBL-11654.

Zeck, H.P., and Mallin, S., 1976. A major global suture in the Precambrian basement of SW Sweden?: Tectonophysics, v. 31, p. 35-40.

APPENDIX 1: Coordinates of SCV Block Corners (From Olsson *et al.*, 1989)

	1	2	3	4	5	6	7	8
X	400	400	550	550	400	400	550	550
Y	1000	1150	1150	1000	1100	1150	1150	1000
Z	310	310	310	310	460	460	460	460

Note: Positions are in mine coordinates

APPENDIX 2.1: Information on SCV Boreholes W1, W2, N2, N3, N4

(From Black *et al.*, 1990)

	W1	W2	N2	N3	N4
Collar Position					
X	440.0	510.0	333.3	347.4	321.1
Y	1146.8	1147.4	1139.2	1079.1	1023.1
Z	356.1	355.3	356.7	356.9	345.0
Bottom hole position					
X	441.7	511.4	530.1	527.4	529.0
Y	1000.3	1000.8	1141.0	1082.6	1025.5
Z	368.1	365.9	420.7	414.2	413.7
Length (m)	147	147	207	189	219
Overall hole direction					
Bearing (trend)	270.66	270.55	0.52	1.11	0.66
Plunge	4.68	4.14	18.01	17.65	18.28
Collar direction					
Bearing (trend)	269.94	269.90	359.85	359.97	359.25
Plunge	4.99	5.02	18.59	18.59	18.80
Bottom hole direction					
Bearing (trend)	271.39	271.19	0.87	2.20	2.12
Plunge	4.13	3.32	17.31	17.01	17.47

Note: Positions are in mine coordinates. Bearings are relative to mine north. Overall hole directions are from collar and bottom coordinates.

APPENDIX 2.2: Information on SCV Boreholes C1, C2, C3, C4, C5
(From Black *et al.*, 1990)

	C1	C2	C3	C4	C5
Collar Position					
X	438.5	442.5	432.8	441.1	443.3
Y	1147.0	1147.0	1147.6	1146.6	1147.1
Z	356.2	356.3	355.9	356.2	356.2
Bottom hole position					
X	435.6	509.4	462.8	459.0	519.1
Y	1029.0	1054.4	1056.6	1099.8	1077.9
Z	448.8	453.4	380.9	392.1	451.0
Length (m)	150	150	100	62	140
Overall hole direction					
Bearing (trend)	268.61	305.86	288.22	290.93	317.61
Plunge	38.11	40.38	14.65	35.62	42.72
Collar direction					
Bearing (trend)	267.94	305.35	287.42	290.84	317.61
Plunge	38.95	40.53	14.68	35.51	42.84
Bottom hole direction					
Bearing (trend)	269.35	306.06	288.82	291.09	317.67
Plunge	37.52	39.91	14.36	35.41	42.45

Note: Positions are in mine coordinates. Bearings are relative to mine north. Overall hole directions are from collar and bottom coordinates.

APPENDIX 2.3: Information on SCV Boreholes D1, D2, D3, D4, D5, D6

(From Black *et al.*, 1990)

	D1	D2	D3	D4	D5	D6
Collar Position						
X	439.1	437.9	438.3	439.7	440.1	438.9
Y	1127.9	1127.7	1128.1	1128.3	1128.4	1128.3
Z	383.3	383.6	382.3	382.3	383.6	384.4
Bottom hole position						
X	469.5	468.1	468.3	469.9	470.3	469.4
Y	1033.9	1033.6	1033.8	1034.2	1034.3	1034.3
Z	389.0	389.4	387.6	388.3	389.5	389.9
Length (m)	100	100	100	100	100	100
Overall hole direction						
Bearing (trend)	287.91	287.75	287.63	287.81	287.78	287.96
Plunge	3.32	3.33	3.09	3.47	3.42	3.16
Collar direction						
Bearing (trend)	287.45	287.41	287.35	287.39	287.45	287.47
Plunge	3.32	3.10	3.26	3.41	3.35	3.37
Bottom hole direction						
Bearing (trend)	288.39	287.75	287.95	288.26	288.25	288.50
Plunge	3.24	3.95	2.80	3.43	3.38	3.00

Note: Positions are in mine coordinates. Bearings are relative to mine north. Overall hole directions are from collar and bottom coordinates.

APPENDIX 2.4: Calculated Fracture Zone/Borehole Intersection Depths

(all distances in meters)

Hole	Length of hole	A	B	H	Hb	I	M	K
W1	147	*	141.74	49.11	60.27	110.93	*	*
W2	147	125.52	87.39	56.57	70.71	118.08	*	102.44
N2	207	*	196.31	*	*	*	18.22	149.01
N3	189	179.49	139.12	*	*	*	39.88	182.17
N4	219	168.74	122.81	*	*	*	102.05	*
C1	150	141.14	98.02	53.01	54.73	104.40	*	*
C2	150	112.10	82.55	67.96	67.38	125.86	*	*
C3	100	*	*	52.44	61.11	*	*	*
C4	62	*	*	56.58	59.04	*	*	*
C5	140	110.51	82.20	81.71	77.11	143.76	*	*
D1	100	*	79.71	25.76	29.65	85.88	*	*
D2	100	*	79.96	25.30	29.03	85.29	*	*
D3	100	*	81.87	26.06	30.31	86.50	*	*
D4	100	*	80.45	26.39	30.62	86.63	*	*
D5	100	*	78.95	26.24	30.03	86.13	*	*
D6	100	*	79.07	25.90	29.42	85.83	*	*

*Zone does not intersect borehole.

APPENDIX 3: Equations for Calculating the Redistribution of Stress about a Cylindrical Excavation

The loading boundary conditions can be visualized as follows. Imagine a rock mass (with no drift) which is loaded by compressive stresses S_H, S_h and S_v that act WNW, E-NE and vertically, respectively (Fig. 9.1). The stresses acting in planes perpendicular to the axis of the not-yet-excavated Validation drift are the tangential normal stress ($\sigma_{\theta\theta}$), the radial normal stress (σ_{rr}) and the shear stress ($\tau_{r\theta}$):

$$\sigma_{rr} = 0.5\ (S_h + S_v) + 0.5\ (S_h - S_v) \cos 2\theta \qquad \text{(A1)}$$

$$\sigma_{\theta\theta} = 0.5\ (S_h + S_v) - 0.5\ (S_h - S_v) \cos 2\theta \qquad \text{(A2)}$$

$$\tau_{r\theta} = -\ 0.5\ (S_h - S_v) \sin 2\theta \qquad \text{(A3)}$$

The term θ is the angle between the normal to the plane of interest and the horizontal. The stresses above would act on planes that strike parallel to the drift axis. The mean normal stress (σ_{bar}) equals 0.5 ($\sigma_{rr} + \sigma_{\theta\theta}$):

$$\sigma_{bar} = 0.5\ (S_h + S_v) \qquad \text{(A4)}$$

The stress acting parallel to the not-yet-excavated drift axis is σ_{zz}:

$$\sigma_{zz} = S_H\ . \qquad \text{(A5)}$$

This stresses would act on planes that strike perpendicular to the drift axis.

Now replace S_H by rigid walls (plane strain conditions) and consider that a drift of radius R is excavated. The new stresses acting *in* planes perpendicular to the drift are (Jaeger and Cook, 1979, p. 251):

$$\sigma_{rr} = 0.5\ (S_h + S_v)(1 - R^2/r^2) + 0.5\ (S_h - S_v)(1 - 4\ R^2/r^2 + 3\ R^4/r^4) \cos 2\theta \qquad \text{(A6)}$$

$$\sigma_{\theta\theta} = 0.5\ (S_h + S_v)(1 + R^2/r^2) - 0.5\ (S_h - S_v)(1 + 3\ R^4/r^4) \cos 2\theta \qquad \text{(A7)}$$

$$\tau_{r\theta} = -\ 0.5\ (S_h - S_v)(1 + 2\ R^2/r^2 - 3\ R^4/r^4) \sin 2\theta \qquad \text{(A8)}$$

$$\sigma_{bar} = 0.5\ (S_h + S_v) - (S_h - S_v)(R^2/r^2) \cos 2\theta. \qquad \text{(A9)}$$

where r is the distance from the drift axis. Note that the pre-drift (i.e. far-field) stress conditions are recovered at large distances from the drift (i.e. r >> R). The changes in stress due to the excavation of the drift are obtained by subtracting the pre-drift stresses from the post drift stresses:

$$\Delta\sigma_{rr} = -\ 0.5\ (S_h + S_v)(R^2/r^2) + 0.5\ (S_h - S_v)(-\ 4\ R^2/r^2 + 3\ R^4/r^4) \cos 2\theta \qquad \text{(A10)}$$

$$\Delta\sigma_{\theta\theta} = 0.5\ (S_h + S_v)(R^2/r^2) - 0.5\ (S_h - S_v)(3\ R^4/r^4) \cos 2\theta \tag{A11}$$

$$\Delta\tau_{r\theta} = -\ 0.5\ (S_h - S_v)(2\ R^2/r^2 - 3\ R^4/r^4) \sin 2\theta \tag{A12}$$

$$\Delta\sigma_{bar} = -\ (S_h - S_v)(R^2/r^2) \cos 2\theta. \tag{A13}$$

Under the plane strain assumptions, the change in stress parallel to the drift (σ_{zz}) would be (Timoshenko and Goodier, 1970, p. 30):

$$\Delta\sigma_{zz} = \nu\ (\ \Delta\sigma_{rr} + \Delta\sigma_{\theta\theta}) = 2\nu\ \ \Delta\sigma_{bar} \tag{A14}$$

The post-drift stress acting parallel to the drift axis is then:

$$\sigma_{zz} = S_H + \Delta\sigma_{zz} = S_H - 2\nu\ (S_h - S_v)(R^2/r^2) \cos 2\theta \tag{A15}$$

Another useful quantity is stress invariant I_1, a measure of the mean stress for three dimensions:

$$I_1 = \sigma_{rr} + \sigma_{\theta\theta} + \sigma_{zz} \tag{A16}$$

$$I_1 = (S_h + S_v) - 2(S_h - S_v)(R^2/r^2)\cos 2\theta + S_H - 2\nu\ (S_h - S_v)(R^2/r^2)\cos 2\theta. \tag{A17}$$

Note that at large distances from the drift, $I_1 = S_h + S_v + S_H$.
The change in I_1 due to the drift is:

$$\Delta I_1 = \Delta\sigma_{rr} + \Delta\sigma_{\theta\theta} + \Delta\sigma_{zz}. \tag{A18}$$

Substituting for $\Delta\sigma_{zz}$

$$\Delta I_1 = \Delta\sigma_{rr} + \Delta\sigma_{\theta\theta} + \nu\ (\Delta\sigma_{rr} + \Delta\sigma_{\theta\theta}) \tag{A19}$$

$$\Delta I_1 = -\ 2(1 + \nu)(S_h - S_v)(R^2/r^2) \cos 2\theta. \tag{A20}$$

The stress effects of the drift are most pronounced at the drift wall (R = r). The post-drift stresses are:

$$\sigma_{rr} = 0 \tag{A21}$$

$$\sigma_{\theta\theta} = (S_h + S_v\ ) - 2(S_h - S_v) \cos 2\theta \tag{A22}$$

$$\tau_{r\theta} = \tau_{\theta r} = 0 \tag{A23}$$

$$\sigma_{bar} = 0.5\ (S_h + S_v) - (S_h - S_v) \cos 2\theta \tag{A24}$$

$$\sigma_{zz} = S_H - 2\nu\ (S_h - S_v) \cos 2\theta \tag{A25}$$

$$I_1 = (S_h + S_v) - 2(S_h - S_v)(R^2/r^2)\cos 2\theta + S_H - 2\nu\,(S_h - S_v)(R^2/r^2)\cos 2\theta. \quad \text{(A26)}$$

The *changes* in stress at the drift wall are:

$$\Delta\sigma_{rr} = -0.5\,(S_h + S_v) - 0.5\,(S_h - S_v)\cos 2\theta \quad \text{(A27)}$$

$$\Delta\sigma_{\theta\theta} = 0.5\,(S_h + S_v) - 1.5\,(S_h - S_v)\cos 2\theta \quad \text{(A28)}$$

$$\Delta\tau_{r\theta} = 0.5\,(S_h - S_v)\sin 2\theta \quad \text{(A29)}$$

$$\Delta\sigma_{bar} = -(S_h - S_v)\cos 2\theta \quad \text{(A30)}$$

$$\Delta\sigma_{zz} = -2\nu\,(S_h - S_v)\cos 2\theta \quad \text{(A31)}$$

$$\Delta I_1 = -2\,(1 + \nu)(S_h - S_v)\cos 2\theta. \quad \text{(A32)}$$

APPENDIX 4: Equations for Calculating the Effective Hydraulic Conductivity for Radial Flow into a Cylindrical Excavation

Flow into a drift can be likened to the steady state radial flow of heat into a cylinder. The rate of heat (fluid) flow q through the walls of a hollow cylinder can be written as (Kreith, 1967, p. 38; Carslaw and Jaeger, 1984, p. 189):

$$q = (T_{outer}-T_{inner})\,(2\pi kl)/\{\ln(r_{outer}/r_{inner})\} \qquad \text{(A33)}$$

where T_{outer} and T_{inner} are the respective temperatures (heads) at the outside and inside walls of the cylinder, k is the thermal (hydraulic) conductivity of the cylinder, l is the cylinder length, r_{outer} is the outer radius of the cylinder, and r_{inner} is the inner radius.

Now consider the case of a composite cylinder of n layers bounded by inner and outer radii (r_1, r_2), ..., (r_i, r_{i+1}), ..., (r_n, r_{n+1}) with conductivities of k_1, ..., k_i, ..., k_n. For constant heads inside ($r=r_1$) and outside ($r=r_{n+1}$) the cylinder, the steady state flow through each layer i will be the same.

$$(q/l)\,\{\ln(r_2/r_1)\}/2\pi k_1 = (T_2-T_1);\ldots \qquad \text{(A34a)}$$

$$(q/l)\,\{\ln(r_{i+1}/r_i)\}/2\pi k_i = (T_{i+1}-T_i);\ldots \qquad \text{(A34b)}$$

$$(q/l)\,\{\ln(r_{n+1}/r_n)\}/2\pi k_n = (T_{n+1}-T_n) \qquad \text{(A34c)}$$

Summing over all n layers

$$(q/l)\,\sum^{n}\{\ln(r_{i+1}/r_i)/2\pi k_i\} = (T_{n+1}-T_1) = (T_{outer}-T_{inner}). \qquad \text{(A35)}$$

For a single-layer cylinder with the same dimensions as the composite cylinder and the same boundary head conditions, a single effective conductivity k_{eff} can be obtained

$$(q/l)\,\{\ln(r_{outer}/r_{inner})\}/2\pi k_{eff} = (T_{outer}-T_{inner}) \qquad \text{(A36)}$$

Equating equations A35 and A36

$$(q/l)\,\sum^{n}\{\ln(r_{i+1}/r_i)/2\pi k_i\} = (q/l)\,\{\ln(r_{outer}/r_{inner})\}/2\pi k_{eff} \qquad \text{(A37)}$$

Solving for the effective conductivity k_{eff}

$$k_{eff} = \{\ln(r_{outer}/r_{inner})\}/\sum^{n}\{\ln(r_{i+1}/r_i)/k_i\}. \qquad \text{(A38)}$$

LAWRENCE BERKELEY LABORATORY
UNIVERSITY OF CALIFORNIA
INFORMATION RESOURCES DEPARTMENT
BERKELEY, CALIFORNIA 94720

AAH194
LBL Libraries